NORTHWESTERN UNIVERSITY

Influence of Multiscale Constraint on Inelastic Deformation Behavior of Austenite and Martensite Phases in Shape Memory Alloys

A DISSERTATION

SUBMITTED TO THE GRADUATE SCHOOL
IN PARTIAL FULFILLMENT OF THE REQUIREMENTS

for the degree

DOCTOR OF PHILOSOPHY

Field of Mechanical Engineering

By

Partha P. Paul

EVANSTON, ILLINOIS

December 2018

ABSTRACT

Influence of Multiscale Constraint on Inelastic Deformation Behavior of Austenite and Martensite Phases in Shape Memory Alloys

Partha P. Paul

Deformation in materials with a hierarchical microstructure is expected to be complex because of the interaction between the units that form such a microstructure [**84**]. One can contemplate that the complexity of deformation would be even higher when additional inelastic deformation modes are active in such materials, apart from traditional elastic and plastic deformation modes. Shape memory alloys (SMAs) are a class of metallic materials that exhibit a nano- to macro-scale hierarchy in the microstructure. NiTi is the most common SMA, used in a variety of applications, from the biomedical industry as implants [**5**] and stents[**139**], to the aerospace industry as actuators [**132, 48**]. NiTi shows remarkable properties such as 'superelasticity', due to which the deformation is reversible, even up to $\approx$ 10% strain. This is possible due to a reversible phase transformation between a high and a low crystal symmetry phase.

When this hierarchy in microstructure is combined with structural features, such as pores, cracks and notches the deformation picture becomes even more heterogeneous, rendering its characterization even more challenging. Each of these structural and microstructural

features acts as a source of constraint, inducing heterogeneity in deformation in its vicinity. Various works in the past have addressed the effect of one or two dominant features, in inducing deformation heterogeneity. This includes structural features such as notches [**137**], pores [**148**], cracks [**33**] as well as microstructural elements such as precipitates [**79**], phase boundaries [**94**], granular constraints from neighbors [**97**] and brittle impurities embedded in a metallic matrix [**96**]. *This work investigates the interactions between various structural features(in the form of pores, notches and cracks), with the microstructure (in the form of grain, phase and twin boundaries), when multiple sources of constraint act simultaneously, across multiple length scales.*

Broadly, this interaction between structure and microstructure is divided into two halves. The first half studies such interactions primarily in the high symmetry austenite phase in NiTi while in the second half, such interactions are studied in the low symmetry martensite phase. In terms of characterization of the material in it's high crystal symmetry phase, the response of the material is studied in the presence of microholes. The size of these pores with respect to the average microstructural length of the material is systematically varied to study the interactions between structure and microstructure. This is expanded to studying the growth of cracks in the vicinity of these holes, with the crystallographic constraints from the grains in the high symmetry phase, and it's effect on the growth rate of cracks and propagation of failure. Finally, this competition between structure and microstructure is studied in micropillars, where the grain size is varied with respect to the pillar size. The suppression of deformation with a systematic change in the size of the grain with respect to the specimen size is examined in detail.

In the second half of this work, the characterization is mainly done on the low crystal symmetry phase, martensite. The spatially heterogeneous evolution of a martensitic

microstructure is examined in a notched specimen. This reveals a variety of inelastic mechanisms that act simultaneously, to result in a microstructure that continues evolving with increasing load in a heterogeneous manner till fracture. Finally, the heterogeneity in deformation around ternary phases and notches are examined in more detail, in terms of the inelastic mechanisms involved in the deformation and the extent of deformation on different domains lying in the vicinity of different sources of structural and microstructral constraint.

A common theme running throughout this work is 'multiscale'. From the range of nanometers up to centimeters, various characterization techniques are used to probe the complex structure-microstructure interactions in materials with a hierarchical structure and microstructure. These include surface (2D) and volumetric (3D) based methods, in situ and ex situ methods and experimental and simulation based methods.

Acknowledgments

First, I would like to thank my advisors. From Germany to Northwestern to Duke, Prof. Brinson has been an advisor, mentor and guide. Between juggling her personal and professional life, she has always ensured she was available for me, as an advisor. Prof. Aaron Stebner has at times been an advisor, friend and sounding board for ideas. From initial times at beamlines to various conferences, he has always struck me with his confident approach to tackling hard research questions. Prof. David Dunand has provided expert advice which was instrumental in getting my thesis off the ground. At various times, various combination of these three professors have helped me navigate my thesis and develop my research outlook.

I would like to thank Dr. Harshad Paranjape. From a post doctorate who started with mentoring me, we have been through a lot together. He has mentored me in research and is an important reason for my growth academically during my PhD. Discussions with him have always been engaging and lively, writing papers and proposals been great learning experiences. I will forever be indebted to his mentorship for shaping my academic outlook. Through numerous days and nights at the beamtimes and shared rooms at conferences, we have discussed research and food and drink and much more. These have played no small part in shaping my approach to research.

I would also like to thank my colleagues, Dr. Ashley Bucsek and Dr. Behnam Amin-Ahmadi in particular, for help with experiments, analyses and for many discussions, both academic and personal. In the Brinson group, I would like to thank Dr. Catherine Tupper

and Dr. Pingping Zhu, for guiding me through my initial year at NU, and easing me into research life. At the national laboratories, beamline scientists have helped me navigate through very challenging beamtimes, including Dr. Jun San-Park , Dr. Hemant Sharma and Dr. Peter Kenesei at Argonne, Dr. Darren Dale and Dr. Darren Pagan at Cornell and Dr. Nobumichi Tamura and Dr. Camelia Stan at Lawrence Berkeley.

At NU, the incredible staff at various facilities have helped me do a variety of experiments. Mark Sinew was incredibly patient while I tried over a year to run mechanical testing on my challenging samples and materials. Karl, Tirzah and Ben have always been available at NUANCE, during my many sessions (both fruitful and fruitless there). Karl in particular, has never been short on help, advice or entertaining stories and observations. In the MatCi facility, Dr. Carla Shute has helped immensely. In the Dunand group, Dr. Dinc Erdeniz helped with various experiments over the years.

Dr. Gang Chen, during his brief time at NU also helped with setting up the research during my initial year at NU. Prof. Pete Anderson from OSU and Prof. Qingping Sun and Dr. Parham Kabirifar from HKUST, through collaborations on projects have been exciting opportunities for me. Other members of the Brinson group have always provided invaluable advice and ear, even though our fields were not the same, including Dr. Marc Palmeri, Dr. Pavan Kolluru, Dr. Min Zhang, Anqi Hu, Dr. Xiaolin Li, Dr. He Zhao, Dr. Xu Cheng, Dr. Yang Li, Dr. Krishanu Nandy, Yixing Wang, Min Zhang, Ridvan, David and Matthew. In the department, Pat and Sinta have been incredibly patient and kind with me. In particular, with so much official travel and so many expenses to be handled, Sinta has been very generous with her time and patience.

Monetary support for my research has come from the office of Basic Energy Sciences, Department of Energy (DE-SC0010594).

My parents have been a constant source of emotional support throughout my life, in particular during my graduate school. My brother has always been a sea of calm, always ready to listen and provide advice while my sister is simply the best doctor I know. Navigating my personal life at NU and in the US has been very rewarding, largely due to Sarah Wolff, who has been a constant source of support as well as a brilliant sounding board for bouncing ideas. Having a fellow PhD to always talk to, about research and life has been a joy. From undergraduate in India through Graduate school in the US, Abhishek and Sanjay have been the two people closest to me, through good times and bad.

Cooking has been a major source of comfort and excitement outside my lab. With Satya, Sarah, Kat, Ishan, Pooja, Max, Armaan and so many others, I had the joy of exploring and experimenting with diverse and innumerable culinary delights. Traveling has been the other big source of joy for me. From the mountains in Montana to the beaches and vineyards in California, these trips have formed a tapestry of delicate and beautiful memories. I will forver treasure these trips with Anant, Saboo, Mahim, Nikhil, Riju, Madhu, Ashwin, Imran. Yet others like Saurabh, Kritish, Pratyush, Vinay, Priyank and a lot of others have been awesome friends.

At NU, being part of the *Indian Graduate Students and Scholars Association* has helped me remain connected to the Indian in me. From Abha to Amit to numerous others, organizing events and dinners for the student community has been incredibly fun and fruitful. The privilege of having the lake in the backyard of my office was immense. Plenty of writing sessions took place, staring into the lake with the sound of water crashing the rocks in my ears. Through the ups and downs and curves of my graduate school, all these have contributed to making me a better researcher and a better person and shaping who I am.

Table of Contents

List of Tables

List of Figures

CHAPTER 1

Introduction

1.1. Motivation

Hierarchical materials are comprised of elements that span across length scales. This hierarchy of constituent elements can come from structural as well as microstructural components that constitute the material [**66**]. Examples of such hierarchical materials abound, from polymers[**4**] to human bones[**13**] and metallic materials, like with the Eiffel Tower. In all these materials, the hierarchy of constituent elements imparts specific properties to the material, such as toughness or strength or ductility. Shape Memory Alloys are a special kind of metallic hierarchical materials, which have a hierarchical microstructure. These materials have crystallites that span length scales from the range of millimeters to nanometers. NiTi is the most common Shape Memory Alloy, having found a variety of uses, ranging from stents and implants in the biomedical field to actuators in the aerospace field [**5, 139, 132, 48**]. The characterization of these materials is also therefore reflective of these length scales, which renders it challenging.

As is common with characterization techniques for multiscale materials, there are two broad categories of characterization. Some studies employ a high resolution study, compromising on the amount of material characterized. For example, TEM studies done on NiTi reveal various inelastic mechanisms at the nanoscale [**134, 136**]. While these provide a rich picture of nanoscale deformation, these techniques are surface based and often ex situ. This raises the question of whether the deformation seen is representative of the entire material

or a snapshot of a particular portion of the material. On the other hand, bulk methods at the macroscale are used to track the specimen scale behavior of the material, such as the elastic constants of constituent phases, the transformation strains and crystallographic texture with respect to an external, changing thermomechanical field [**120, 130**]. While these techniques correctly reflect the overall behavior of the material, the compromise is in terms of the spatial resolution, where the material is assumed to contain millions of grains.

Therefore, a combination of methods is increasingly being used, to obtain a picture of deformation which is both representative of the entire material as well as containing good spatial resolution. Works combining Digital Image Correlation (DIC), X-ray diffraction and modeling [**96, 97, 85**] have been used to explain the effect of constraints arising from grain and phase boundaries on stress induced transformation and the nucleation of fatigue cracks. This thesis aims to explore the hierarchical microstructure and structure of NiTi specimens in a similar way, employing a mixture of techniques to understand the deformation behavior, in particular the interactions between structure and microstructure across length scales.

1.2. Background

The widespread use of NiTi arises from the remarkable properties exhibited by this material, where it can be deformed to large strains (up to $\approx 10\%$) without permanent deformation. Such large strains are recovered through thermomechanical loading, giving rise to the properties of *superelasticity* and the *shape memory effect*. These are possible due to a solid-state diffusionless phase transformation between a high crystal symmetry (cubic) *austenite* phase and a low crystal symmetry (monoclinic) *martensite* phase, which is reversible. The austenite phase is stable at high temperatures and low loads, while the martensite is stable at low temperatures and high loads.

Figure 1.1(a) elucidates the mechanism of *superelasticty*. Beginning with the austenite phase at zero load, increasing the load isothermally induces a stress induced phase transformation into the martensite phase. At the peak load illustrated, the material exists in a mixed austenite and martensite phase. Further loading results in the complete transformation into the martensite phase. On unloading, the material is transformed back to the parent austenite phase. Figure 1.1(b) illustrates the *shape memory effect*, which involves manipulating both the mechanical load and the temperature. The material starts as pure martensite, which exists in a twinned microstructure, called a *self accommodated microstructure*. On loading, the martensite deforms via inelastic mechanisms such as detwinning, producing a large strain, which is not recovered upon mechanical unloading. This detwinned martensite is then heated, transforming it into the austenite phase. When the heated austenite phase is cooled back to the starting temperature at zero load, the material again transforms to the martensite phase, in it's *self accommodated* state.

Therefore, in contrast to traditional elastic-plastic metallic materials, SMAs deform via the mechanisms of elasticity and (stress induced) phase transformation 1.1(a). In addition to these, the *austenite* phase also deforms via plastic slip at high loads [**108, 23**]. The low symmetry martensite phase deforms via detwinning, as shown in Figure 1.1(b). In addition to this, it also exhibits twin nucleation, amorphization and slip [**84, 53, 63, 126**]. Therefore, characterizing the heterogeneous and multiscale deformation in SMAs primarily involves deconvoluting the effects of these various mechanisms that are often acting simultaneously.

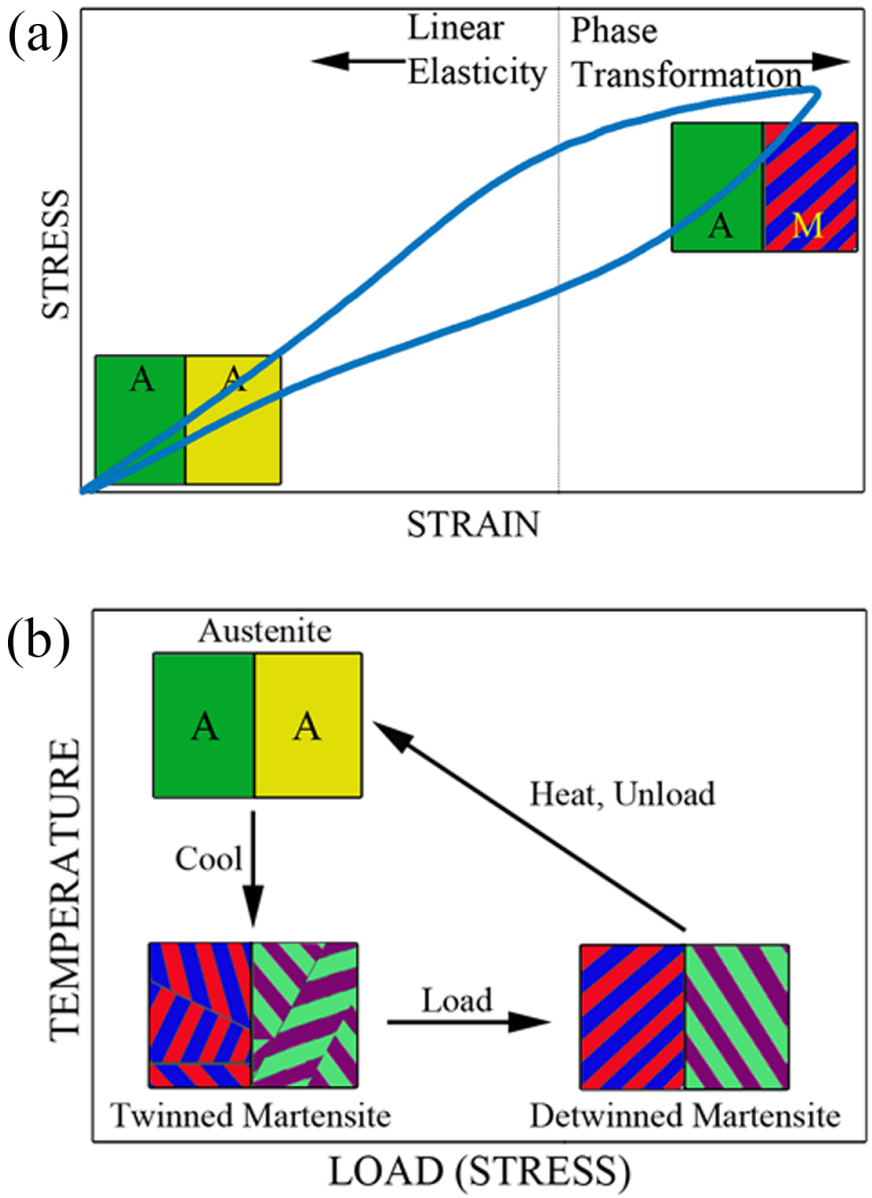

Figure 1.1. Thermomechanical deformation of SMAs. (a) shows the property of superelasticity, where an isothermal loading results in a reversible phase transformation. (b) shows the shape memory in SMAs. Through a combination of thermal and mechanical loading, SMAs undergo reversible phase transformations which is reversible by mechanical load as well as inelastic deformations, which are recoverable by thermal deformation.

1.2.1. SMAs: Hierarchical Materials

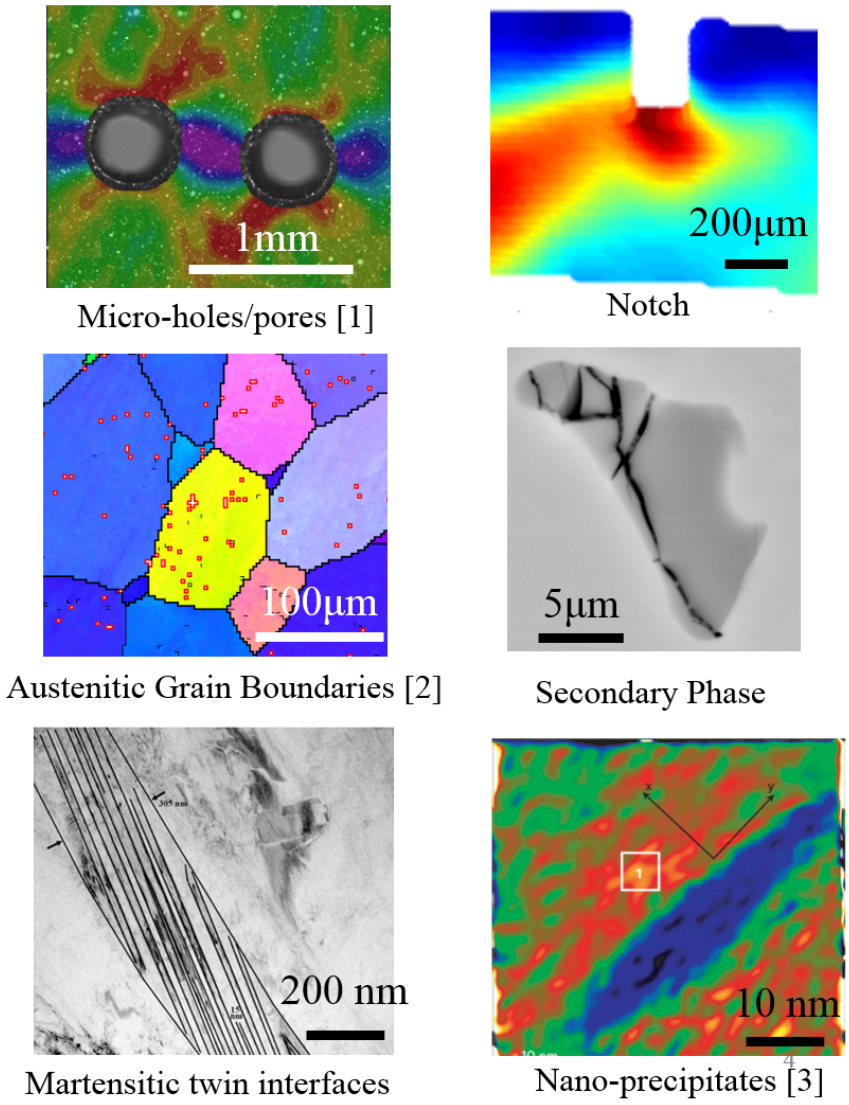

Figure 1.2. Hierarchy of SMA microstructure and structure. (a-f) reveals the hierarchy of various elements comprising the structure and microstructure of SMAs. (a, b) show structural constraints in the form of holes and notches respectively, acting at the mm - cm range. (c, d) show microstructural constraints in the order of mm - µm scale, in the form of austenitic grain boundaries (adapted from [**101**]) and brittle Ti inclusions. (e, f) show microstructural constraints in the µm - nm range, in the form of twin interfaces of martensite and nanoprecipitates of Ni and Ti [**127**].

Therefore, through a manipulation of the thermal and mechanical deformation field, SMAs can be taken through high deformation, which is reversible in nature. However, the characterization of this deformation becomes challenging when the length scales of the crystallites that make up this hierarchical microstructure are considered. In addition to the microstructural hierarchy, a variety of structural features and their influence on deformation and competition with microstructure is also studied in detail. Structural features are those arising from the geometry of the specimen. This includes pores, holes, notches and cracks. Microstructural features are those arising from the material itself. These include grains and grain boundaries in the austenite phase, ternary phases (usually oxides and carbides of Ti, in the form of brittle inclusions), twin interfaces in the martensite phase, phase boundaries (between the austenite and martensite phase or between either phase and inclusions) and precipitates (Ni_4Ti_3). The length scale of these range from the order of millimeters to nanometers, as shown in Figure 1.2.

1.2.2. Multiscale Characterization

The characterization techniques employed in this work can be broadly split into two categories: experimental and simulation based techniques, shown in Figure 1.3. Each row in the figure is arranged in increasing spatial resolution from top to bottom, ranging from the macroscale to the nanoscale. These methods encompass surface and volumetric as well as in situ and ex situ capabilities. The salient features of each technique, in terms of capabilities and utility is summarized in Table 1.1.

Experimental techniques are usually of two kinds, based on the way the characterization is done: in situ and ex situ. In addition, the techniques can be surface based or volumetric. On the other hand, modeling techniques are classified according to the phenomena and

mechanisms they are used to examine, complimenting the experimental findings at that length scale. At the macroscale, the nominal stress-strain-temperature curves are plotted, using load cells, extensometers and thermocouples. At this scale, the behavior of the entire specimen at the specimen scale is examined. Techniques such as neutron diffraction are then used for in situ measurement of specimen scale variables and their evolution with the load state. This is used to explain the phenomena of *superlelasticity* during isothermal loading and *shape memory effect* during thermomechanical loading [**82, 15**], the effect of crystallographic texture on mechanical properties [**43, 72**]. To compliment experimental endeavors at the macroscale, phenomenological models are used to model the specimen scale deformation [**26**]. These are self consistent models that have been used to elucidate the role of structural constraints such as arrays of holes/pores [**147**], isolate the effect of structure from microstructure [**101**], isolate elastic and inelastic mechanisms [**16, 24, 92, 64**] and study the thermomechanical response during deformation [**18, 83**].

At the millimeter to micrometer range, the techniques involve a higher spatial resolution than that afforded by the macroscale techniques. Digital Image Correlation (DIC) is an in situ method of calculating surface strains by tracking the movement of points of interest by taking a series of images of the specimen surface during deformation. DIC is often combined with coarser techniques such as macroscale thermomechanical loading, to tie local strain variations with the global stress-strain evolution and deformation mechanisms [**67, 60**]. On the other hand, DIC is also combined with higher resolution surface based microscopy techniques such as Scanning Electron Microscopy (SEM) and Electron BackScatter Diffraction (EBSD) to tie the microstructural elements to local heterogeneities in the surface strains caused by them [**59, 32, 55**]. Finally, DIC is also combined with 3D, volumetric methods at the micro to mesoscale to connect the surface deformation to bulk deformation[**97, 96**].

X-ray diffraction, fluorescence and tomography techniques are used for in situ and non-destructive deformation characterization at the micro to mesoscale. The diffraction techniques are used to calculate the orientations and strain tensors during in situ loading, with a spatial resolution of ≈1 µm - 20 µm. X-ray High Energy Diffraction Microscopy (HEDM) is a 3D, in situ technique used to obtain grain scale deformation, orientation and position [**9, 98**]. This technique is typically employed along with X-ray microtomography, for accurate tracking of the specimen boundaries[**45**]. Apart from obtaining the full (3D) strain tensor at the grain scale, the strain can also be partitioned into elastic and inelastic components [**96**]. X-ray micro diffraction, also known as microLaue diffraction is an X-ray diffraction based technique, that can provide sub-micron spatial resolution. It is a 2D, surface based technique to calculate local orientations and strains, during in situ loading , [**49, 25, 109**]. The diffraction is usually complimented by imaging of the surface using X-ray fluorescence. Therefore, this class of X-ray techniques vary in resolution as well as surface versus volumetric capabilities, but have unique properties of in situ and non desctructive capabilities and act as a bridge between the macroscale and nanoscale techniques.

Using electrons instead of X-rays for diffraction and imaging results in an increase in spatial resolution but a decrease in the volume of material that can be observed, due to poor penetration of electrons as compared to X-rays. SEM and EBSD are the two most commonly used characterization tools that bridge the mesocale and the nanoscale. Both of these are destructive characterization techniques. They are most commonly used ex situ, to image the material surface before and after the deformation, though many in situ applications have been developed in recent years [**39, 77, 87, 65**]. These techniques are used to map grain orientations in the high symmetry (austenite) phase, heterogenous phases in materials [**35**] and map remnant deformation post loading[**106**].

Simulations at the micro to mesoscale are usually micromechanics based[**110, 80, 6, 103, 108**]. Crystal plasticity based models are used to model the deformation [**76**], accounting for the phase transformation crystallography and plasticity at the grain scale. The inputs obtained from the imaging and diffraction techniques listed above are often used as inputs to such models, to validate and build on the experimental results [**97, 100**]. These combined X-ray, electron and modeling based techniques form a majority of experimental techniques spanning between the macroscale and the nanoscale.

Finally, at the nanoscale, Transmission Electron Microscopy (TEM) is used to study individual crystallites in the low symmetry phase and the deformation mechanisms associated with it. TEM is a destructive characterization technique, used to observe small areas of the specimen. In SMAs, TEM has been used to study the effect of nano precipitates on the deformation response [**57**], size effects [**135**], amorphization of the martensite phase at room temperature [**136, 90**] as well as crystallography of twin structures [**73**] under loading. TEM involves an intricate procedure for sample preparation, along with the smallest volumes under investigation, while providing the highest spatial resolution.

In summary, a variety of techniques are available and necessary, to allow for the full scale characterization of hierarchical materials such as SMAs. Using various appropriate combinations of these, the mechanisms that cause the deformation in such materials is examined in detail, based on the length scale of investigation. The combined picture formed from all these will help provide a picture of deformation that is representative of the material and the specimen as a whole, whilst also having adequate spatial resolution to account for the spatial heterogeneities in the deformation.

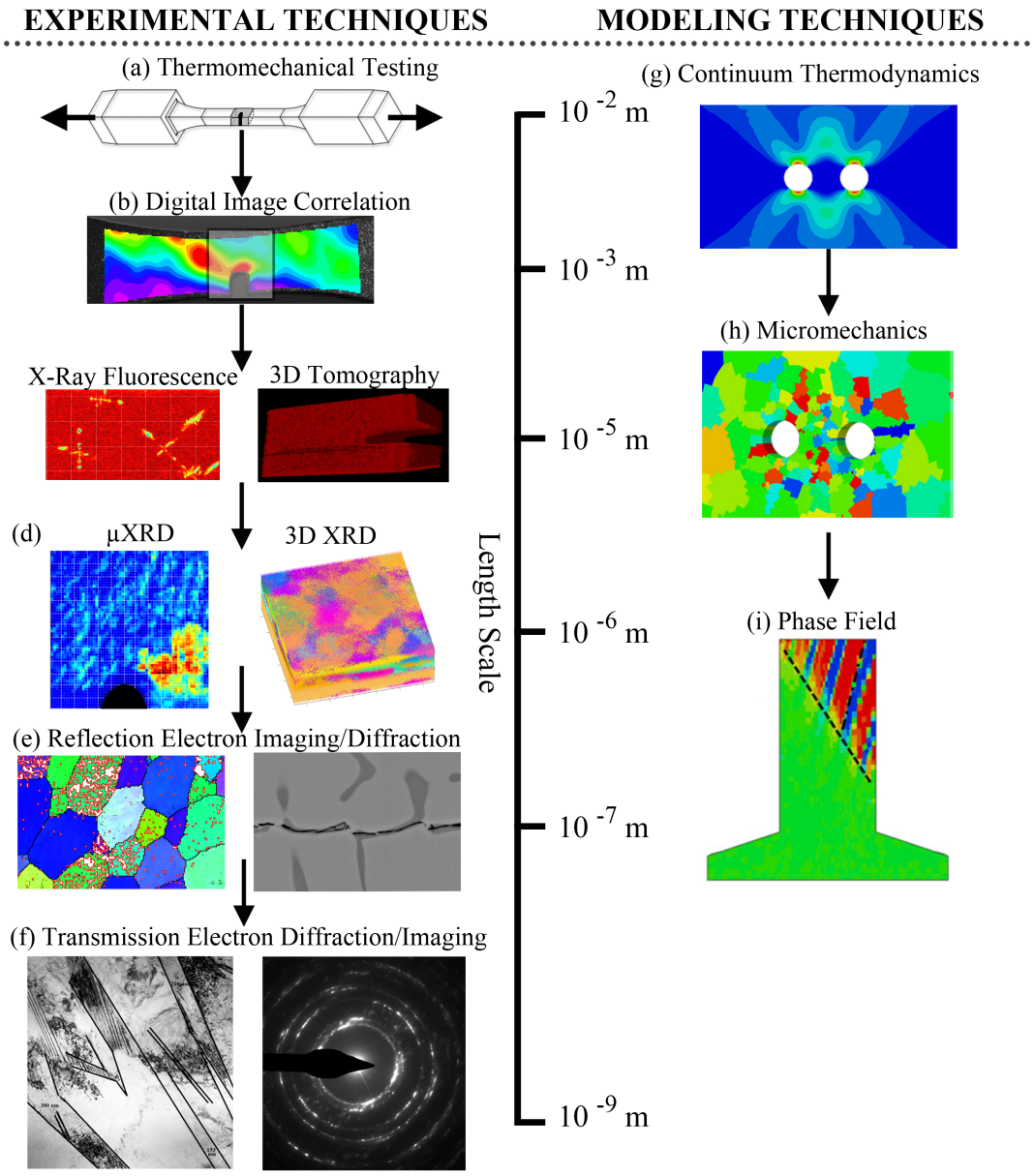

Figure 1.3. Multiscale characterization scheme. (a-i) reveal a combination of experimental and simulation based techniques and the associated length scales used for characterizing deformation phenomena in NiTi. (a-f) encompass experimental techniques in increasing spatial resolution from cm down to nm, combining surface (2D) and volumetric (3D) methods, along with in situ and ex situ methods. (g-i) encompass simulation based techniques with increased spatial resolution, ranging from cm - µm.

Table 1.1. Capabilities of techniques used and phenomena studied

Technique	**Type**	**Purpose**	**Spatial Resolution**	**2D/ 3D**
Mechanical loading	Experimental	In situ, isothermal macro load state	≈10cm	3D
Extensometer	Experimental	In situ macro strain state	≈10mm	2D
DIC	Experimental	In situ mapping of surface strains	≈50 µm	2D
X-ray Tomography	Experimental	In situ mapping of exact specimen boundaries	≈20 µm	3D
X-ray HEDM	Experimental	In situ mapping of orientations and strains	≈20 µm	3D
X-ray Fluorescence	Experimental	In situ mapping of exact specimen boundaries	≈2 µm	2D
X-ray Microdifraction	Experimental	In situ mapping of orientations and strains	≈2 µm	2D
SEM	Experimental	Ex situ locations of heterogeneous phase	≈100nm	2D
EBSD	Experimental	Ex situ crystallography and phase mapping	≈100nm	2D
TEM	Experimental	Ex situ interfaces, crystallites and phases	≈1nm	2D
Phenomenological modeling	Simulation	Deformation heterogeneity from structural features	-	3D
Crystal Plasticity	Simulation	Heterogeneity from crystallography of microstructure	-	3D
Phase Field modeling	Simulation	Inelastic deformation mechanisms	-	3D

1.3. Research Objectives and Outline

Section 1.2 introduces various phases in NiTi SMAs and the various inelastic mechanisms associated with them, that act, often simultaneously, during deformation. Section 1.2.1 then outlines various constituents of the hierarchical microstructure of NiTi, along with hierarchical structure of NiTi specimens. Finally, Section 1.2.2 outlines a plethora of characterization techniques across multiple length scales, along with the phenomena they are used to study deformation behavior in SMAs. Through the thesis, these mechanisms will be studied using combinations of the techniques presented, in the hierarchy of structure and microstructure with an aim of answering the following questions:

(1) What is an effective methodology for characterizing materials where the deformation mechanisms and the deformation heterogeneities induced thereof are at different length scales.
(2) If multiple sources of constraint act simultaneously, how can the effect of each be individually understood in the overall deformation picture.
(3) If different deformation mechanisms act at different length scales, how can they be effectively deconvoluted and understood.

This work can be broadly divided into two parts, which each attempt to answer the research objectives listed above. The first part consists of studying deformation phenomena in a material which is primarily in the high symmetry *austenite* phase. Chapter 2 addresses the first question, through a study of the competition between structure (micro holes) and microstructure (nano precipitates) in determining the deformation response at low loads. Chapter 3 builds on the results from Chapter 2 and studies this competition, at a higher level of deformation. Here, the effect of grains and micro holes are examined on the rate of

growth of cracks and propagation of failure in the material. Chapter 4 rounds out the first part, examining the role of grain size relative to specimen size in determining the extent of suppression of phase transformation in micropillars.

The second half of the thesis deals with characterization of deformation and the associated deformation mechanisms in a material which primarily exists in the low symmetry *martensite* phase. Chapter 5 studies the spatial heterogeneity of the martensitic microstructure and it's evolution with load under the influence of structural (notch) and microstructural (heterogeneous phase) constraints, revealing a microstructure that continues to evolve with the load state up to fracture. Chapter 6 studies the spatial heterogeneity in extent and mechanisms of inelastic deformation in the low symmetry phase, based on location with respect to structural (notch) and microstructural (heterogeneous phase) sources of constraint. Chapter 7 summarizes the work and lays out some recommendations for future directions of this work.

CHAPTER 2

Interactions between Structure and Microstructure Influence Stress Induced Phase Transformation

Adapted with permission from: Partha P Paul, Harshad M Paranjape, Behnam Amin-Ahmadi, Aaron P Stebner, David C Dunand, L Catherine Brinson (2017). Effect of machined feature size relative to the microstructural size on the superelastic performance in polycrystalline NiTi shape memory alloys. Materials Science and Engineering: A, 706, 227-235.

Characterization efforts on SMAs can be divided into two broad categories, based on the relative length-scale of the extrinsic structural features (such as pores, cavities and cracks) and the microstructural features (such as grain morphology and orientations) in the specimens studied. Mechanics of SMAs at length scales where the size of the specimen or any machined features is sufficiently larger than the grain size allows for the assumption of spatially homogeneous and occasionally isotropic material properties. This length-scale has historically received extensive attention in terms of both modeling and characterization. However, at a length-scale of the structural features approaching the intrinsic microstructural length, material properties are heterogeneous (e.g., the crystal orientation abruptly changes from one grain to another) and consequently interpretation of the local phase transformation response must take into account these heterogeneities.

Experimentally, phenomena such as the dependence of transformation stress and recoverable strain on texture and crystal orientations [**15, 14, 22**], anisotropy in the elastic

modulii of austenite and martensite [**107, 105, 118**], relative stresses for the onset of phase transformation, reorientation, plasticity and their relative strain contribution [**120**] have been studied extensively using various diffraction techniques and *in-situ* testing. Common to these studies is the assumption that the volume interrogated contains a large number of grains and the observed response is not dependent on individual grain responses or on microstructural heterogeneities, but rather on volume-averaged, representative material parameters. Similarly, the observed response is insensitive to the specimen size. However, size effects become observable as the specimen size is decreased. Particularly as the specimen size approaches the microstructural length scales, the size effects become prominent. When the microstructural length scale is measured in terms of the average grain size, this spans from the nanometer to micrometer range in most metals and alloys.

Experimental studies conducted on SMA wires with various diameters, micrometer and nano-sized pillars, and polycrystals with nanometer to micrometer-sized grains have revealed a change in the transformation mechanics as the intrinsic size is reduced. For example, experiments on Cu-based SMA show that thermal effects related to heat transfer from the wire to the surroundings play a role in determining critical transformation stress and hysteresis when the wire diameter is large (hundreds of microns). However, in thinner wires (1 µm to 100 µm), the heat transfer is near-instantaneous and the transformation kinetics is dominated by granular constraints and pinning at free surfaces. The result is a higher hysteresis width in thinner wires due to a larger relative free surface area to provide pinning sites. Another manifestation of this size effect is a transition from many martensite domains to a single domain microstructure with decreasing intrinsic size [**129**]. At even smaller length scales, in micro and nano-pillars, the onset of transformation is sudden [**89**] and its progression seen to occur in a non-smooth manner and the hysteresis shows a non-intuitive relation

with the thermal cycling rate – it decreases with higher thermal cycling rates [**142, 112**]. S tructure-property relationships are seen to be very different in nanocrystalline NiTi wires, as compared to conventional wires, with an increased fatigue damage resistance and recoverable strain in wires with nano-sized grains [**113**]. An extreme manifestation of the size effects occurs at the length scales smaller than 200 nm in NiTi SMAs, where the phase transformation is completely suppressed in very small grains [**38, 135**].

A distinction between length scales is essential to reliably predict the thermo-mechanical response of SMAs depending on the specimen size. This distinction is reflected in the numerical models for SMAs. At the macro-scale, phenomenological or self-consistent models are suitable to predict the thermo-mechanical response on cycling, multi-axial loading behavior, and contributions from multiple inelastic mechanisms – phase transformation, reorientation, detwinning and plasticity [**18, 16, 8, 92, 83, 24, 56**]. These models, while being computationally efficient, do not account for microstructural heterogeneity. Micromechanics based approaches, in contrast, are able to capture the effect of microstructure and simulate the local SMA response [**99, 37, 124, 76, 108, 95**]. These approaches are suitable to predict the performance and microstructural evolution at the micro to nano length scales. While it is appealing to use these micro-mechanical approaches to model SMA behavior of aggregates with millions of grains, it is not practical due to prohibitive computational expense. Hence it is necessary to make a choice between the two approaches depending on the required level of detail in the predicted response.

To make such a choice between phenomenological and micromechanical models, an understanding of the role played by the size of structural features (e.g., machined holes, pores, notches) and individual grains in polycrystal deformation is necessary. Previous endeavors on studying the effect of structural features include:

(1) A numerical exercise to understand the coupling of elastic and inelastic strain fields locally around a single machined hole and hole assemblies using a phenomenological model [**148**]

(2) A comparison to experimental strain fields around a single hole using digital image correlation, when the hole is much bigger than the mean grain size [**10**].

While empirical studies on wires with micron-scale diameter and *bamboo* grain morphology address some of the issues related to the size effects when the grain and structural sizes are similar, there are several open questions. The influence of grain interaction on SMA deformation has been explored numerically [**93**] and empirically [**60, 97**], however the nature of granular interaction is not clear when the specimen or the features in it are of comparable size to the grains themselves. The role played by microstructure vs. the stress concentration in a small specimen or around small structural features in determining the local superelastic response is unclear. With the increasing interest in miniature SMA components, including micro electro-mechanical systems and porous SMA assemblies where the pore size can be comparable to the grain size, a quantitative understanding of the deformation phenomena at the intermediate length scales is essential.

This chapter explores the SMA mechanics at the length scale where the structural feature size approaches the microstructural length scale. Using three specific cases, we vary the size of machined features (micro-holes) in SMA specimens until the micro-hole diameter is comparable to the average grain size. We track the local and global strain fields during superelastic loading using digital image correlation (DIC), a technique that has been extensively used to characterize the SMA deformation at the micro and macro length scales [**10, 30, 58**]. By comparing the measured surface deformation with the prediction of a

macro-scale, phenomenological model, we are able to identify a length scale at which the phenomenological prediction significantly deviates from the measured strain. This is the length scale at which the microstructure starts to play a significant role in determining the local deformation, rather than the homogeneous material properties or the boundary conditions. Hence the key outcome of this work is a criterion in terms of relative length scales of specimen, structural features, and microstructure, to determine the propriety of phenomenological vs. microstructural modeling approaches for predicting SMA deformation.

2.1. Materials, Experiments and Simulations

2.1.1. Material and Sample Description

A polycrystalline NiTi plate (Ti-50.53at.%Ni) supplied by Confluent Medical Technologies (formerly Nitinol Devices and Components) was used to prepare three planar dogbone specimens with 25 mm × 3 mm gage dimensions according to the ASTM E8 standard [**3**]. The transformation temperatures were determined by differential scanning calorimetry (DSC), using a Mettler Toledo DSC822^e calorimeter to be $A_s = 293\,\mathrm{K}$, $A_f = 303\,\mathrm{K}$ from the heating curve and $M_f = 255\,\mathrm{K}$, $M_s = 278\,\mathrm{K}$, $R_s = 283\,\mathrm{K}$ and $R_f = 293\,\mathrm{K}$ from the cooling curve. The dogbone specimens were cut using electrical discharge machining and subjected to a high temperature anneal at 1200 K for 900 s in vacuum and oven cooling to room temperature. Then a second anneal at 773 K in air for 1800 s with the specimens sandwiched between heavy steel plates to ensure that the specimens did not warp during annealing, followed by a low temperature anneal at 473 K for 86.4 ks. The surface was then ground and polished up to 1 µm using a diamond-based solution, followed by vibratory polishing with 0.06 µm colloidal silica.

Tensile testing was performed on each of the following three dogbone specimens.

Table 2.1. Dimensions of the planar dogbone specimens used to perform tension tests. D, t, d, and L are schematically shown in Figure 2.1(b).

Name	Width (D, mm)	Thickness (t, mm)	Hole Diameter (d, µm)	Hole Spacing (L, µm)
MONOLITH	3.02	0.70	-	-
S550	2.99	0.44	564	970
S150	3.02	0.59	156	266

MONOLITH: This sample has a monolithic gage section without any machined holes.

S550: This sample has two 564 µm diameter holes machined in the center of the gage with 970 µm center-to-center spacing.

S150: This sample has two 156 µm diameter holes with a 266 µm center-to-center spacing in the center of the gage.

The dimensions of these specimens are summarized in Table 2.1, and the specimen geometries are schematically shown in Figure 2.1(a).

To ensure repeatability of the results, additional samples with similar hole diameters to S550 specimen were tested and demonstrated similar results in terms of the macro stress-strain response to the key findings in Section 3 and Section 4. However, the results for those additional specimens are not shown.

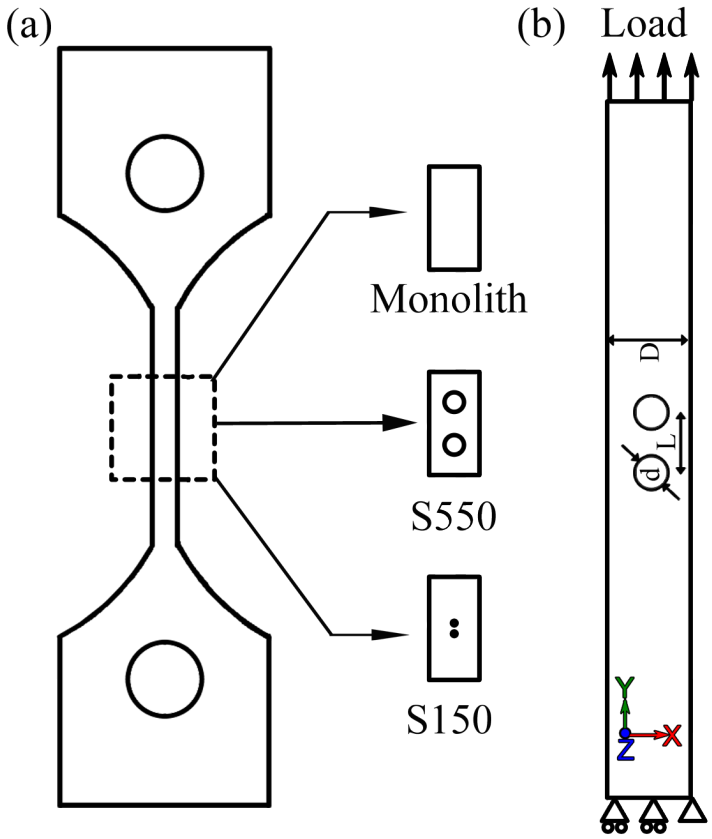

Figure 2.1. (a) Schematic of the tensile dogbone specimens with the details of the machined hole geometry. (b) Boundary conditions employed in the finite element analysis (FEA). The same boundary conditions are employed in all the simulations.

2.1.2. Tension Experiment Setup

The specimens were loaded in tension at room temperature to 0.75% global axial strain under displacement control at an engineering strain rate of $2 \times 10^{-4}\,\mathrm{s}^{-1}$ and then unloaded to zero load. The loading was done using a Sintech 20G load frame and the global strain was measured using a 1 mm knife-edge extensometer.

Local strains around the holes were measured using a digital image correlation (DIC) setup consisting of a Point Grey Grasshopper (9.1 MP) camera with a K2 Distamax Long

Distance Microscopic lens. DIC is a non-contact method for the measurement of surface strains by tracking the movement of patterns on the specimen surface and has been used extensively to measure strain distributions in SMA specimens [**31, 78**]. A grey layer of paint primer was used as the background layer and 5 µm alumina particles were then sprayed on the wet primer to obtain a speckle pattern. A sequence of images of the gage section captured at 1 frame per second during loading and unloading for each specimen was then analyzed through VIC2D software from Correlated Solutions to obtain the local axial strains.

2.1.3. Microstructural Analysis

Grain orientation distribution and mean grain size in the representative regions in each specimen were obtained by electron backscatter diffraction microscopy (EBSD) using a FEI Quanta 600F electron microscope. These measurements were performed prior to tension testing. Post-mortem transmission electron microscopy (TEM) analysis of the S150 sample was performed using FEI Talos (FEG, 200 kV) to characterize the phases and precipitates present. The location for TEM analysis was chosen based on the EBSD data such that a $\langle 1\,1\,1\rangle_{B2}$ zone axis was aligned in the TEM. A cross-sectional TEM thin foil was prepared using the Focused Ion Beam (FIB) lit-off technique and bright field and selected area diffraction pattern (SADP) of the sample were obtained.

2.1.4. Simulations Using a Phenomenological Model for Phase Transformation

The superelastic response during the tension experiments for each specimen was simulated using a macro-scale, phenomenological model consisting of elastic and phase transformation constitutive laws. This model uses a constant Lagrange multiplier based explicit integration

scheme for reduced computational expenses. The model and its Abaqus user material (VUMAT) implementation are described in detail elsewhere [**117**], however the key features of the formulation are:

(1) The representative volume element (material point) is assumed to be a polycrystal with isotropic elastic properties and a uniform maximum transformation strain ($\varepsilon_{\mathrm{tr}}^{\mathrm{max}}$).

(2) The total strain ε at a material point is additively decomposed into an elastic (ε_{e}) and a transformation component ($\varepsilon_{\mathrm{tr}}$) as: $\varepsilon = \varepsilon_{\mathrm{e}} + \varepsilon_{\mathrm{tr}}$.

(3) The volume change on transformation from austenite to martensite phase is assumed to be negligible as is the standard assumption of the Crystallographic Theory of Martensite [**11**].

(4) Martensitic transformation is tracked through two internal variables: self accommodated martensite volume fraction (ξ_{SA}) and oriented martensite volume fraction (ξ_{σ}). The total martensite volume (ξ) fraction is the sum of these two components: $\xi = \xi_{\mathrm{SA}} + \xi_{\sigma}$.

(5) Only the oriented volume fraction of martensite contributes to the transformation strain.

(6) A phenomenological expression for the driving force for phase transformation is constructed as a function of the deviatoric stress, temperature, and the oriented martensite volume fraction.

The finite element mesh in each case was constructed using 4-node bilinear *plane stress* quadrilateral reduced integration elements (CPS4R in Abaqus notation). The MONOLITH specimen had the same element size throughout the sample (100 elements along the 25mm

gage length). In the case of specimens with holes, a finer finite element mesh was constructed near the holes with a gradual transition to a coarser mesh near the sample edges. For the S150 and S550 samples, at the gage center, the mesh was seeded such that the density of the nodes along the holes remained the same (52 elements along the circumference of the holes). A convergence study was conducted on all the samples to ensure that the mesh was sufficiently resolved, especially near the holes. Since this model does not take any micromechanical inputs, the size of the elements with respect to the average grain size of every specimen is not considered. The boundary conditions imposed in the simulations are shown in Figure 2.1(b). They include a rolling boundary conditions on one edge perpendicular to the loading direction to constrain that edge in the direction of loading, a pinned corner of the sample to prevent rigid body modes and a uniform displacement applied to all nodes on the other edge, to mimic the experimental loading.

The elastic stiffness, onset stress for forward and reverse transformation, and the hardening parameters for the forward and reverse transformation were calibrated using the global stress-strain curve obtained for the MONOLITH specimen. Strain along the loading direction and martensite volume fraction were recorded from each of the simulations. The simulated global stress-strain curves are obtained from the displacements at points corresponding to the location of the edges of the extensometer and the reaction forces obtained from the loading edge of the finite element analysis (FEA) model geometry considered. Table 2.2 summarizes the calibrated model properties and material parameters used in the simulations. The parameters include kinetic parameters (A_r), internal parameters (C^r, C^f) and hardening co-efficients (H_σ, K).

Table 2.2. Calibrated material properties and model parameters for the phenomenological simulations.

Property	Symbol	Value	Parameter	Value
Young's modulus	E	32 GPa	Y_{re}	40 MPa
Poisson's ratio	ν	0.4	H_σ	4000 J kg^{-1}
Density	ρ	6.45 gm cm^{-3}	C^f	105 MPa
Martensite start	M_s	278 K	C^r	2 MPa
Martensite finish	M_f	255 K	A^r	2 MPa
Austenite start	A_s	293 K	K	1 MPa
Austenite finish	A_f	300 K		
Patel-Cohen coeff.	$C_{A,M}$	4.5 MPa K^{-1}		
Max. trans. strain	ε_{max}	0.04		
Yield stress	σ_0	1000 MPa		
Initial martensite fraction	ξ_0	0		

2.2. Results

2.2.1. MONOLITH Sample

Figure 2.2 shows the experimental (solid curve) and simulated (dotted curve) global stress-strain response for the MONOLITH sample during a uniaxial tension test. In the experimental curve, during loading, a non-linearity appears at a global strain between 0.45 and 0.5%. The transition in the slope of the experimental curve is gradual vs. an abrupt transition in the simulated response. Martensite phase fraction values from the simulation show that

this transition represents the onset of phase transformation. The stress-strain curves are hysteritic, and on unloading, the strain completely recovers. At four representative points marked 1 to 4 on the curve in Figure 2.2, the experimentally observed local axial strain distribution in the dogbone gage center is shown in the top row. The local strain gradually increases to a maximum of approximately 0.85% at the peak imposed global strain. At peak global strain, the variation in the local strain is ≈0.4%. For the unloading part, DIC strain measurement shows a gradual reduction in strain to approximately 0% (not shown in the figure). The middle row shows the axial strain distribution from the FEA simulation. The phenomenological model naturally shows a more homogeneous strain distribution as compared to the experiment. The average simulated axial strain at the peak is 0.75%.

2.2.2. S550 Sample

Figure 2.3 shows the global axial stress-strain response for the S550 sample, as obtained from the experiment (solid curve) and from the simulation (dotted curve). The experimental stress-strain curve transitions to a non-linear response between 0.35 and 0.4% axial strain, which is smaller than 0.5% for the similar transition for the MONOLITH specimen. The peak global stress for this case is 250 MPa, which is higher than the peak stress of approximately 220 MPa for the MONOLITH specimen. The global strain shows near complete recovery on unloading with less than 0.01% residual strain at 0 load. The local axial strain distribution measured using DIC at four representative points (1 to 4) is shown in the top row. At point 2, shortly after the onset of non-linearity in the global stress-strain curve, two bands of larger local axial strain emanate from the holes and travel to top-right and bottom-left corners of the gage. With increasing global strain, the local axial strain in these two bands grows until

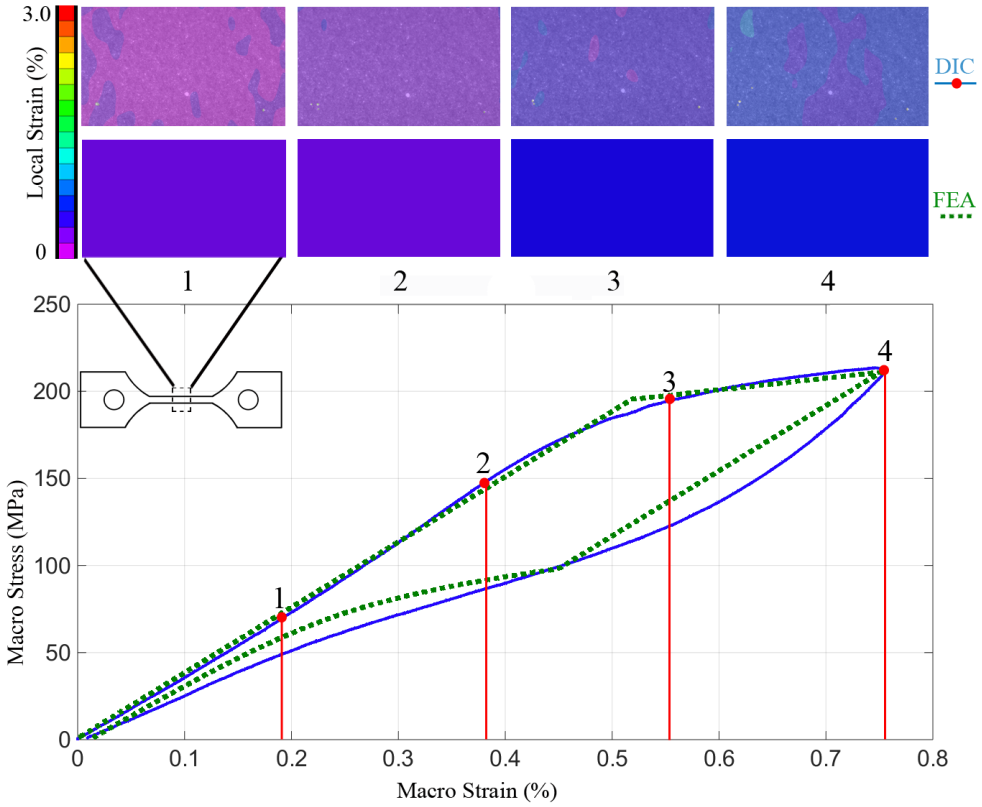

Figure 2.2. MONOLITH specimen. Global stress-strain curves and local strain maps obtained from the experiments (solid curve and top row), and macro-scale simulations (dotted curve and bottom row). At peak load, the specimen shows a maximum DIC strain of ≈0.85%

it reaches ≈3% at peak global strain. The axial strain away from the holes, in the left and the right regions of the DIC area is near 0%.

The peak stress is underestimated by the phenomenological model (200 MPa), as compared to the experimentally obtained stress value (250 MPa). Plausible reasons for this difference include local plasticity around the holes leading to toughening of the sample and a lack of microstructural input to the FE model. However, it is to be noted that this difference in the macro stress-strain response is not expected to have any influence on the local

stress-strain measurement or behavior around the holes, which is the focus of the following sections.

Local FEA axial strain results for the S550 specimen are shown in the middle row over the global curves. The model predicts the formation of "V" shaped bands emanating from each hole. The strain bands have two axes of symmetry: a horizontal axis passing through the center of both holes and a vertical axis passing through the mid-point between two holes. The axial strain in the bands varies between approximately 1% and 2%. There is a strain maximum predicted just above and below each hole and a broad region of strain minimum is predicted between the two holes. Though the local FEA results for the unloading part are not shown, they show a gradual reduction in the axial strain with full strain recovery on unload.

2.2.3. S150 Sample

Figure 2.4 shows the macro stress-strain response for the S150 specimen, as measured experimentally (solid curve), and obtained through the simulation (dotted curve). The global experimental response is similar to the MONOLITH specimen. However, a small residual strain ($\approx 0.02\%$) at the end of unloading is observed. The axial strain distribution in the center of the gage, measured using DIC, is shown in the top row. The axial strain is uniform. The average axial strain around the holes at the peak global strain is in fact comparable to the imposed global strain. No strain localization around the holes is observed.

Simulated macro stress-strain response for S150 is shown by the dotted curve, and the local strain map around the holes in the gage is shown in the middle row of Figure 2.4. Similar to S550 simulation, a pronounced strain minimum between the holes and the formation of

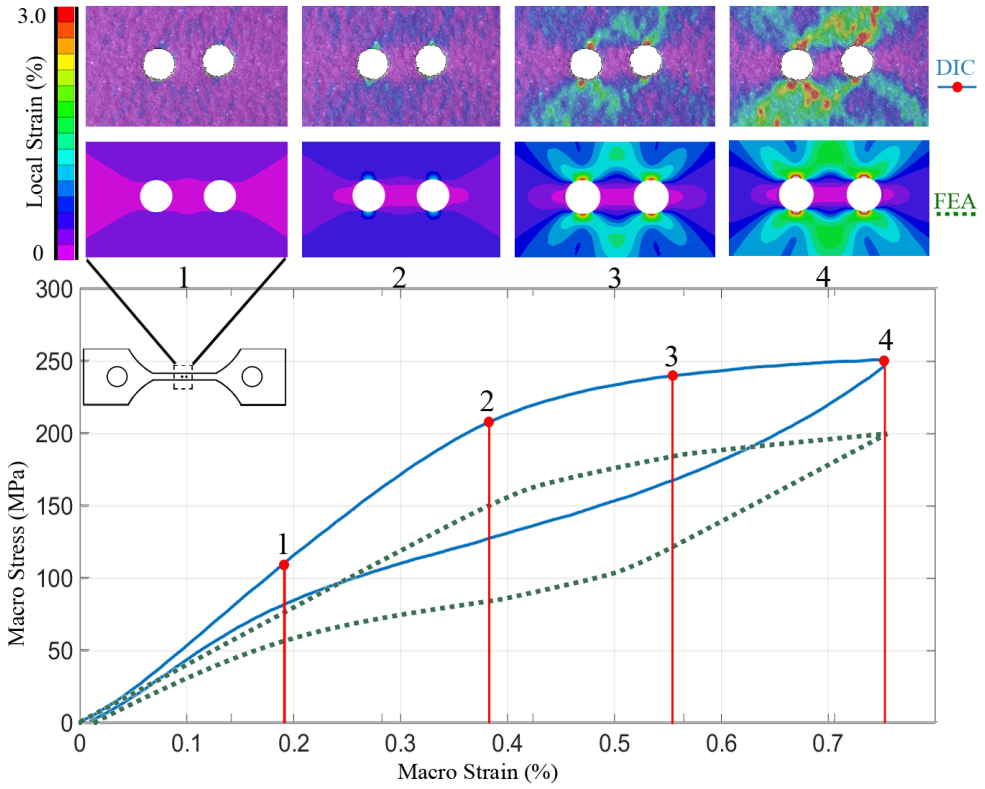

Figure 2.3. S550 specimen. Global stress-strain curves and local strain maps obtained from the experimental results (solid curve and top row) and simulated response (dotted curve and bottom row). At peak load, the specimen shows a maximum DIC strain of ≈3%. Both experiment and simulation show the formation of strain bands around the holes.

symmetric "V" shaped bands of relatively larger strain around the holes, is predicted for S150. The bands grow perpendicular to the loading direction with increasing global strain.

2.2.4. Microstructural Characterization

Figure 2.5 (a-c) show the gage-section microstructures for the MONOLITH, S550, S150 specimens respectively. The grain orientation distributions in terms of inverse pole figure maps are shown in the inset for each subfigure. The grain orientations show a random texture. The

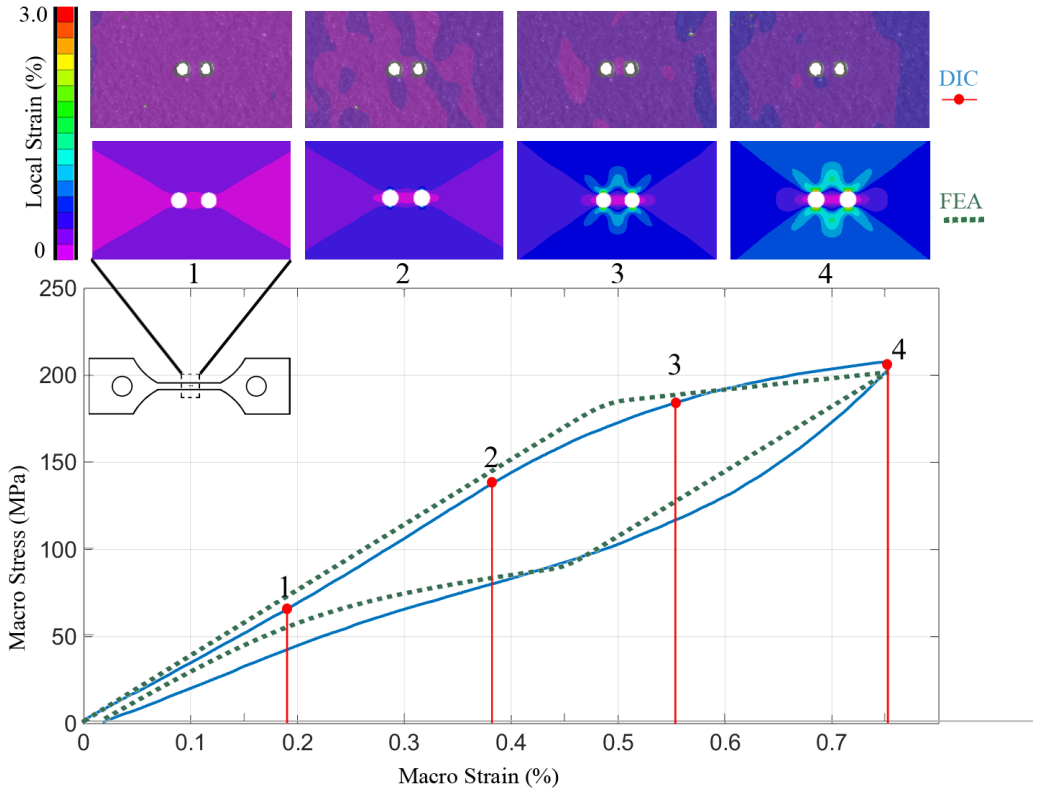

Figure 2.4. S150 specimen. Stress-strain curves and local strain maps obtained from the experiment (solid curve and top row) and simulation (dotted curve and middle row). At peak load, the specimen shows a maximum DIC strain of ≈0.8%. The experimental response does not show any strain localization around the holes, while the simulated response shows the formation of "V" shaped strain bands.

mean grain size, calculated using the linear intercept method, in the MONOLITH, S550 and S150 specimens is approximately 50 µm, 87 µm, and 50 µm respectively. The grain structure around the holes is similar compared to that away from the holes. In the S550 specimen, there is some grain refinement between the holes to a mean grain size of approximately 50 µm. However, we do not expect this to affect the response of the material, as this size is well below the grain size where the Hall-Petch effect begins to be observed. In SMAs, size of grains is expected to play a role in the deformation behavior in the *nanometer regime*, by

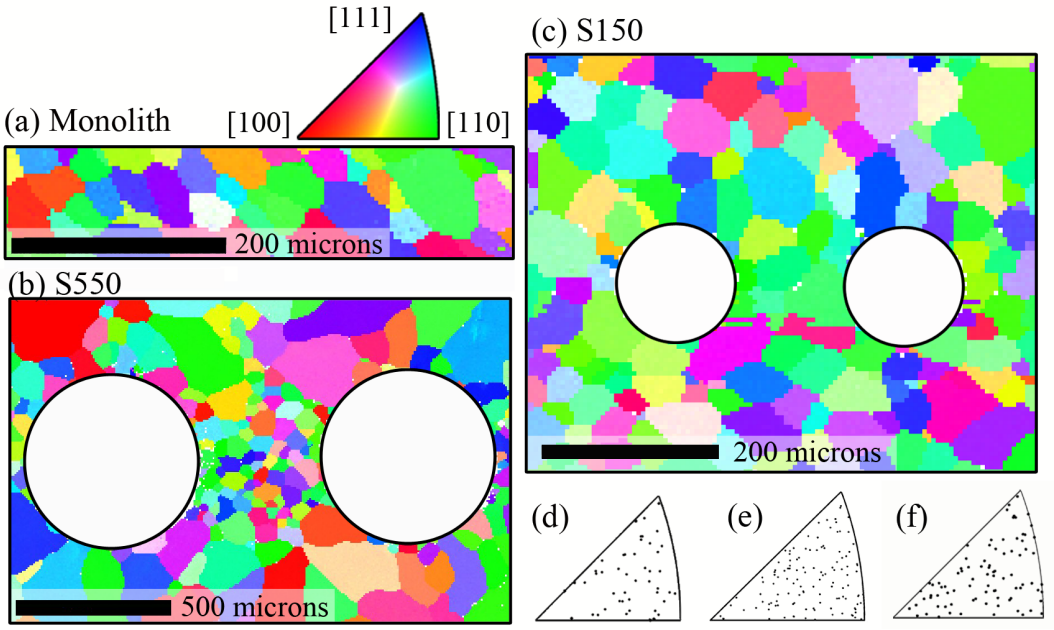

Figure 2.5. Grain maps and orientation data (a-c) and mean grain orientation distributions with respect to the loading axis (d-f) for MONOLITH, S550 and S150 specimens respectively, obtained using EBSD. The grain size distribution is similar across the specimens and the texture is random.

affecting the transformation onset stress and transformation strain produced [**143**] or causing the suppression of phase transformation altogether [**129**]. The grain sizes considered in this work are well above the nanometer scale and we do not expect to see noticeable effects from the grain size.

2.3. Discussion

A comparison between the spatial distribution of the experimentally measured axial strain and the simulated axial strain in all specimens indicates a trend. The agreement between the model and the experiments decreases as the size of the machined features is reduced from MONOLITH to S150. This suggests that the influence of the microstructural features relative to the effect of the structural features increases as the size of the holes is reduced to

approach the average grain size in the specimens. In this section, we discuss the role of the most important structural factor – the presence of holes, relative to the role of microstructural factors, in determining the local strain distribution in each specimen. The microstructural factors considered include the grain structure and any presence of precipitates and secondary phases.

2.3.1. Effect of Relative Microstructural Size and Hole Size on Strain Distribution

2.3.1.1. Structural Factors Determine the Strain Distribution in MONOLITH

. For the MONOLITH specimen, the local axial strain distribution at the peak macro strain in the experiments (Figure 2.2) shows a relatively small variation (mean 0.8%, standard deviation 0.2%) compared to other specimens. The area in Figure 2.2 where the axial strain distribution is reported, is approximately 3×2 mm. The mean grain size (diameter) in that specimen is approximately 50 μm. Thus the imaged area consists of approximately 3000 grains. Presence of such large number of grains in the imaged region is expected to smear out the heterogeneous transformation strains in the individual grains.

The experimental MONOLITH stress-strain response shows a gradual change in slope at approx. 0.5% strain. Such transition is typically associated with the onset of phase transformation. This is consistent with the experimental results obtained by Brinson et al. [**19**] and the simulations of Manchiraju and Anderson [**76**], where the global stress strain curve shows a gradual transition into the transformation regime. Since grains with varying orientations are present in the specimen, phase transformation initiates in favorably oriented grains. With the increasing imposed strain, phase transformation progressively begins to occur in less favorably oriented grains. Thus the experimental slope gradually decreases as

more and more grains start transforming. This phenomenon is not captured in the macro-scale simulation results as the model is agnostic of the microstructure-level progression of phase transformation. Thus in the MONOLITH specimen:

: **Presence of holes**: Not applicable. But the imposed boundary conditions (i.e., the imposed macro strain) determined the observed response.

: **Microstructure** did not have specific effect on the local strain response. However, the interaction between grains introduced a gradual change in slope in the macro stress-strain response.

2.3.1.2. Structural Factors Determine the Strain Distribution in S550 and an Influence of the Microstructure is Apparent

. Addition of the structural features in the S550 specimen introduces heterogeneity in the observed strain response. The main source of heterogeneity is the stress concentration around holes. This results in the axial strain concentration of approximately 3% around the holes. This structural effect is captured by the phenomenological model as shown in the simulated local strain plots in Figure 2.3 (middle row). While the formation of strain bands is anticipated due to the stress concentration around holes, the experimentally observed bands are asymmetric. A similar observation of asymmetric strain bands around machined holes was made by Bewerse et al. using optical microscopy [**10**]. This departure from symmetry can be attributed to the influence of the microstructure.

A strain band emanating from the left hole in the S550 specimen is interrupted by a group of grains unfavorably oriented for transformation. Figure 2.6(a) shows the DIC strain map for S550 at the peak load. The V-shaped strain band starting from the left hole is interrupted in the top-left corner of the figure. This region is marked by slant lines. The

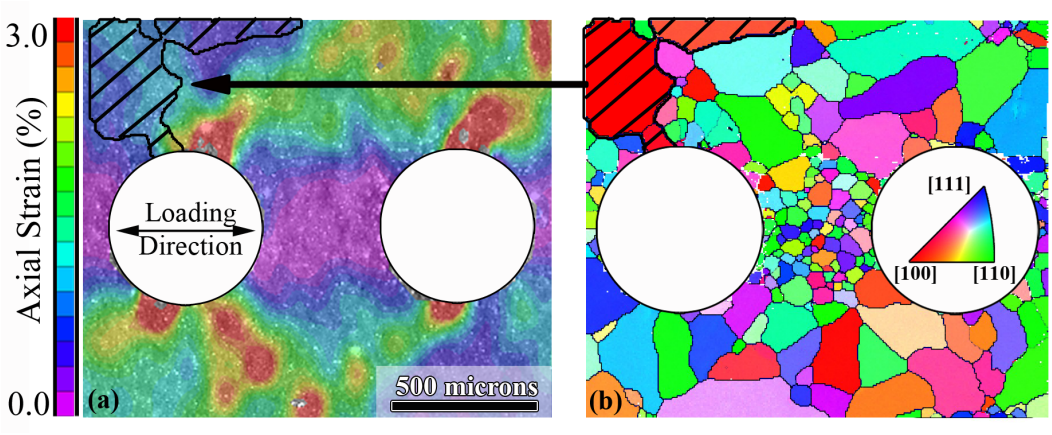

Figure 2.6. S550 specimen. (a) Experimental axial strain at peak load with the overlaid boundary of a group of [0 0 1] oriented grains. (b) EBSD grain map showing the [0 0 1] grains in the top-left corner. The grains are marked with slant lines. According to the Crystallographic Theory of Martensite [**11**], these grains are oriented to produce relatively small axial transformation strain in tension in NiTi compared to e.g., [1 1 1] and [1 1 0] oriented grains.

EBSD grain map for the specimen is shown in Figure 2.6(b). Several grains with a [1 0 0] orientation are situated in the same region where the strain band is interrupted. According to the Crystallographic Theory of Martensite (CTM) [**11**], [1 0 0] orientation in NiTi produces a smaller axial transformation strain compared to e.g., [1 1 0] or [1 1 1] orientations. Thus the interrupted strain band is likely the result of the [1 0 0] oriented grains present in that region. Since the phenomenological model does not incorporate any microstructural inputs, the strain concentration in Figure 2.3 is symmetric. Based on this information, grain orientation is identified as the key microstructural factor in influencing the local strain response in the case of S550. Thus in the S550 specimen:

: **Presence of holes** lead to stress concentrations, which then caused strain localization of up to 3% in V-shaped bands.

: **Microstructure** affected the local strain distribution. Specifically, grains that are unfavorably oriented for phase transformation, lead to smaller strains even in the

regions where a stress concentration is present due to the holes. Additionally, similar to MONOLITH, the interaction between the grains introduced a gradual onset of phase transformation.

2.3.1.3. Strain Distribution in S150 is Determined by the Microstructural Factors

. The strain measurements for S150 specimen show a strong departure from the observation for S550. Despite the availability of sites for stress concentration, S150 does not show distinct strain bands (Figure 2.4) and the simulated strain bands in S150 are lower in strain magnitude compared to S550 simulation results.

To compare the structural effect of the holes in S550 and S150, analytical calculations based on the tabulated stress concentration formulae [**104**] are performed on the samples. The peak stress for a sample with thickness t is calculated as a product of the theoretical stress concentration factor (k_t) and the nominal stress (σ_{nom}), based on the reduced cross sectional area due to the holes, in two separate cases:

(i): a single hole of diameter d in an infinitely long specimen with a fixed width D

$$k_t = 3.000 - 3.140(d/D) + 3.667(d/D)^2 - 1.527(d/D)^3 \tag{2.1}$$

(ii): a pair of holes of diameter d separated by L in an infinite solid

$$k_t = 3.000 - 0.712(d/L) + 0.271(d/L)^2 \tag{2.2}$$

The nominal stress, normalized to the uniaxial tensile load P, in both the cases is

$$\sigma_{nom}/P = 1/(t(D-d)) \tag{2.3}$$

The normalized peak stresses for S150 based on cases **(i)** and **(ii)** are **1.68** and **1.58** respectively. For the S550 specimen, the normalized peak stresses based on cases **(i)** and **(ii)** are **2.37** and **2.51** respectively. This shows that the structural stress concentrations are more prominent in the S550 sample as compared to the S150 sample. The presence of more prominent strain bands in S550 can be rationalized based on the higher stress concentration around the holes in the S550 sample. Just the lower stress concentration in the S150 sample however, cannot be used to completely rationalize the absence of strain bands. This suggests that causes of microstructural origin dominate over the structural stress concentration in determining the local strain distribution.

In S150, the grains have a uniform size distribution and the texture is random, as shown by the EBSD grain maps in Figure 2.5(b). Thus, grain structure alone is not the cause behind the absence of strain concentration bands. Further microstructural analysis reveals that precipitates may have played a role in determining the local deformation patterns in S150. Based on the heat treatment employed on the samples (as described in Section 2.1), specifically the 773 K, 1800 s annealing between heavy steel plates, Ni_4Ti_3 precipitates are expected to form in the S150 specimen. Khalil-Allafi et al. [**57**] observed such precipitation in Ti-50.7at.%Ni annealed at 773 K for 3600 s under stresses up to 20 MPa. TEM analysis from a FIB lift-out from a region between the holes as shown in Figure 2.7(a, b) shows the presence of precipitates and R-phase. Figure 2.7(c, d) show the corresponding bright-field TEM micrograph and selected area diffraction patterns (SADP). The presence of Ni_4Ti_3 precipitates and R-phase is confirmed based on the 1/7 $\langle 3\,2\,1 \rangle$ and 1/3 $\langle 1\,1\,0 \rangle$ super-reflections, respectively. These observations are consistent with the work of Michutta et al. [**79**], who observed the precipitation of Ni_4Ti_3 in Ni-rich NiTi during aging under compressive loads up to 50 MPa and the preferential nucleation of R-phase at the precipitate-matrix boundary

while cooling. Similarly, Xie et al. [**141**], empirically observed that the precipitate-matrix boundaries acted as preferred nucleation sites for the martensite phase. The cause for this selective nucleation of the R-phase was investigated by Zhou et. al. [**146**], who established that Ni_4Ti_3 precipitates act as stress concentrators causing preferential nucleation at the interface of the precipitate with the austenite matrix by numerically estimating the magnitude of stress variation along the interface.

Thus, precipitate-assisted nucleation of martensite and R-phase at various locations in the specimen gage, coupled with a lower stress concentration near the holes compared to S550 and stress concentration around the precipitates, is likely to have resulted in a more uniform strain distribution at peak load in S150. While S550 specimen is also expected to have precipitates, since it underwent an identical heat treatment, the effect of precipitate-assisted nucleation in that case is expected to be secondary to the larger stress concentrations around the holes. In the MONOLITH specimen on the other hand, due to the absence of stress concentration sites (i.e., holes) the effect of precipitates, if any, is indistinguishable from the homogenized response over many thousands of grains. Thus in the S150 specimen:

: **Presence of holes** did not appear to play a role in determining the local strain distribution.

: **Microstructure** determined the local strain distribution. Specifically, the presence of uniformly distributed Ni_4Ti_3 precipitates assisted the nucleation of martensite and the secondary phase, leading to a more uniform strain distribution around the holes on loading at room temperature.

This analysis shows that the microstructure played a progressively more important role in determining the strain response from MONOLITH to S150. Since the same heat treatment

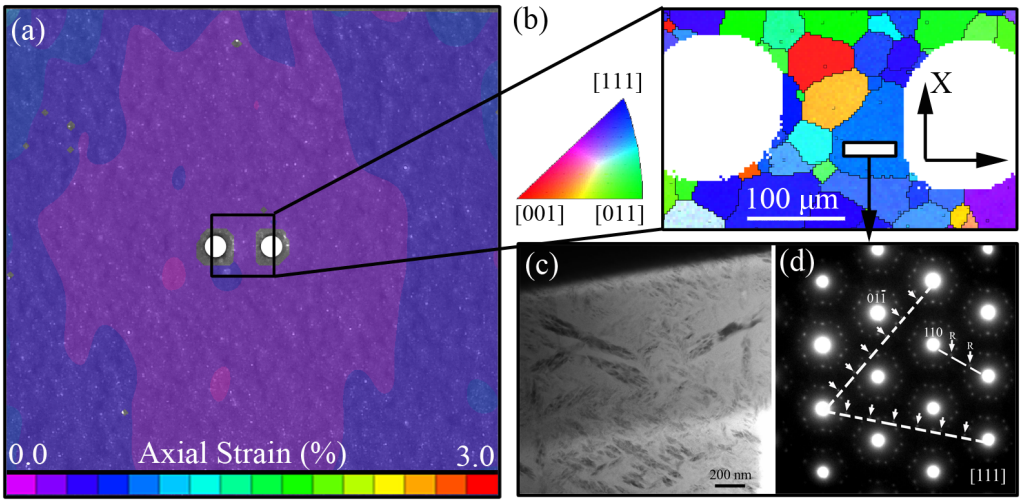

Figure 2.7. S150 specimen. (a) Experimental axial strain at peak load, as obtained from DIC. (b) EBSD map of region highlighted in (a), colored according to orientations with respect to the X axis. The FIB cross-sectional cut is indicated by solid black lines. (c) Bright field TEM micrograph of the specimen and (d) the corresponding SAD pattern showing the $\langle 1\,1\,1\rangle_{B2}$ zone axis containing R-phase reflections of type $1/3\langle 1\,1\,0\rangle$, along with $1/7\langle 3\,2\,1\rangle$ reflections of Ni_4Ti_3 precipitate.

is employed in all three samples, the precipitate distribution is expected to be similar. The relative size of the structural features however, decreased from MONOLITH to S150. In the gage section of MONOLITH there are thousands of grains present. In S550, there are approximately 60 grains between the holes. In S150, there are less than 10 grains between the holes. The precipitate size and separation is of the nanometer-scale, as shown in Figure 2.7(c), yet it dominated the strain response in S150. Thus, we propose a criterion for selecting phenomenological vs. microstructural models for capturing local strain response around structural features in SMAs based on two factors – the structural feature size relative to the average grain size and the presence of other microstructural features such as precipitates.

2.3.2. Suitability of Micromechanical vs. Macro-scale Models for SMAs

The discussion in the previous subsection points to the increased influence of microstructural effects as the machined feature size is systematically reduced. For example, in MONOLITH, the local deformation is completely determined by the imposed boundary conditions. In S550, where the feature size is approximately 6 times the average grain size, the deformation is partially influenced by the microstructure. However, when the region of interest contains a few grains as in S150, and when other microstructural features such as precipitates that can affect the nucleation and growth of martensite are present, the local strain response is dominated by the microstructure. Thus we propose that –

- Macro-scale, phenomenological models can adequately capture the local deformation response when the region of interest is larger than 10 times the mean grain size.
- Micromechanical models are necessary to capture the local deformation response in SMAs, when the region of interest is comparable to the mean grain size and when features such as precipitates are present that can modify the spatial distribution of martensite.

This conclusion however has certain exceptions. For example, the regions that are *far enough* from the structural features or stress concentration sites may not experience the effect of local heterogeneities. This is similar to the Saint-Venant's principle, where the local distribution of the loads does not significantly influence the deformation in the regions sufficiently away from where the loads are applied. This points towards the presence of a critical neighborhood around the structural inhomogeneities where microstructural information is essential to reasonably predict the local deformation response. However, in regions

away from the holes for example, phenomenological models that do not account for the microstructural heterogeneities continue to be adequate, as long as the the regions interrogated contain a large number of grains. Also, when the region of interest is large, the local influence of precipitates or inclusions is small.

This discussion is relevant to predicting the response in small SMA assemblies like micron sized actuators and sensors, and porous structures, where the relative sizes of structural features (like pores) are comparable to the length scale of the intrinsic microstructure of the material. In such cases the above criterion can be useful in selecting an appropriate macro scale model or a microstructural model.

2.4. Conclusions

In this work we examined a structural feature size effect on the local deformation in a NiTi SMA by studying three contrasting cases with varying sizes of machined holes with respect to the average grain size in planar specimens. This study details the deformation behavior using extensive characterization on three specific specimen cases which reflect the extremes of hole (feature) size with respect to the grain (microstructure) size. Even though NiTi is used as a model system, these results are expected to apply to other SMAs as well.

(1) In the absence of structural features or stress concentration sites, the deformation is homogeneous to a global strain of 0.75%, as seen in the MONOLITH specimen. The axial strain distribution, simulated using a macro-scale, phenomenological model for phase transformation is adequate to capture the uniform strains seen in the experiment.

(2) In a specimen where the grain size is relatively small compared to the hole size, structural effects dominate over microstructural effects, as seen in the S550 specimen. Individual grains influence the local strain distributions, e.g., grains unfavorably oriented for transformation interrupting a strain band in the region of stress concentration.

(3) In the specimens such as S150 where stress concentration around the holes is diminished, the holes are comparable in size to the grains, and feature such as precipitates are present that can modify the martensite nucleation and growth mechanics, the microstructural effects dominate over structural effects. In these cases, the local strain distribution significantly deviates from the prediction of the macro-scale model, where the predicted stress concentration around the holes does not reflect in the actual axial strain observations.

(4) Microstructural models are more appropriate to predict local phase transformation response when the region of interest or a structural feature in the specimen is less than ten times in size compared to the average grain size, or when precipitates can influence local martensite nucleation and growth. When a multitude of grains are present in the region of interest, a macro-scale model is adequate for predicting the local phase transformation response.

In the future, this work will be well complimented by an approach that characterizes a larger number of samples to provide statistical insights into the interaction between machined features and local phase transformation response. An efficient way to do this is using micromechanical modeling, which takes experimental microstructural characterization as an input to predict grain and sub-grain scale deformation in virtual samples.

CHAPTER 3

Interactions between Structure and Microstructure Determine Micromechanics of Crack Growth

Adapted from: Partha P Paul, Margaret Fortman, Harshad M Paranjape, Peter M Anderson, Aaron P Stebner, L Catherine Brinson (2018), Influence of Structure and Microstructure on Deformation Localization and Crack Growth in NiTi Shape Memory Alloys, Shape Memory and Superelasticity 4(2), 285-293.

3.1. Introduction

In the implant industry, porous NiTi SMAs in particular are a candidate material for bone implants [**17**]. Porosity can promote tissue growth, and by varying the pore volume fraction, the stiffness of the implant can be matched with the stiffness of the bone. The emerging techniques of metal additive manufacturing (AM) are particularly suitable for making such components due to the ability of these methods to produce near-net-shape products with complicated geometries [**29, 36**].

There is another, less obvious advantage of using metal AM to make porous SMA products or SMA assemblies with micro-scale features such as holes, channels, or notches. The stress and strain distribution in such assemblies with structural features can be highly heterogeneous owing to the stress concentrations near the pores [**101**]. Additionally, the deformation in SMAs is highly orientation dependent. Since implants typically undergo cyclic

loading, deformation can accumulate over time in these stress concentration zones and eventually lead to failure. Hence tailoring local grain orientations around pores or other features may provide a method to relieve stresses, reducing the likelihood of crack nucleation around pores. To this end, AM has the unique flexibility to allow such microstructural tailoring. The control of grain size in AM components of Ti-6Al-4V is possible to some extent by controlling the laser parameters such as scan speed and power in laser-based AM builds [**61**]. More recent efforts have also demonstrated that metal AM can be used to tailor site-specific properties including grain orientation and morphology [**27**]. DeHoff et al. showed the possibility of such site-specific orientation control in Inconel 718 by varying electron beam scan parameters in specific patterns [**34**]. When selective laser melting (SLM) of random textured raw material is used to build NiTi SMA parts, [1 0 0] is observed to orient along the build direction under the laser spot [**111**]. Ma et al. showed that by the controlling the SLM processing parameters, a spatial variation in the transformation temperatures can be obtained in a NiTi SMA build [**34**]. Wang et. al. recently studied the relationship between laser parameters in SLM and the local composition and transformation temperatures, tuning them to produce parts with alternating layers of austenite and martensite phase [**138**]. Thus, strategically designed laser scan patterns can be used to develop specific microstructures by controlling grain orientations and composition in SMAs. With this control of orientations, AM promises to be a useful technique to produce both tailored geometries as well as site-specific property variations.

In anticipation of the advancement of these AM techniques that enable tailorability of the microstructure, we focus on a related mechanistic issue: the influence of the grain structure, grain orientations, and micro-hole geometry on the deformation localization and crack growth in NiTi SMA. We collectively explore deformation localization and crack growth since most

often micro-cracks nucleate in the regions of accumulated inelastic deformation. Micro-holes provide a simple model for the complex stress-state that is likely to develop in porous SMA assemblies as well as AM-produced SMA products with small-scale features. These mechanistic aspects have been extensively studied individually. For example, micro-holes and notches are known to induce multi-axial stress-states and multiple martensite variants in their vicinity [**87**] and also act as the nucleation sites for cracks [**62**], while grain boundaries are known to constrain deformation due to phase transformation [**23**]. Crack growth in SMAs has been extensively studied both at the individual crystal scale as well as in a statistical sense, using empirical [**28, 140, 33, 109**] as well as modelling based techniques [**51, 7**]. However, the influence of structural features along with the accompanying microstructure on deformation localization and crack growth has not been studied together.

This work employs a coupled experimental and modeling approach to provide a new understanding of the effects of microstructure and defects on localization and crack growth. We use microstructural modeling to systematically vary the grain orientation in two virtual SMA specimens with micro-holes to explore the trends in strain localization around holes. We then use an empirical approach to qualitatively characterize the paths followed by cracks growing from micro-holes and traversing multiple grains in a superelastic NiTi SMA planar specimen loaded in tension. In Section 2, we introduce the modeling and experimental methods used. The first half of Section 3 contains results from the simulations while the latter half consists of results and discussions from the experimental investigations.

3.2. Materials, Experiments, and Simulations

In this work we use two methods: cyclic tension experiments with *ex-situ* electron microscopy and micromechanical modeling. The experimental approach is used to monitor

crack growth around a pair of micro-holes in a NiTi plate during cyclic tensile loading. The micromechanical modeling is used to simulate the strain evolution and strain-band formation in virtual samples. The microstructures in these simulations are based on the experimental sample. The details of these methods are described below.

3.2.1. Description of materials, specimen, and experiments

The superelastic NiTi SMA material containing 55.6wt.%-Ni and the experimental specimen used here are similar to the ones extensively described in [**101**]. The relevant details are summarized below.

(1) The material is superelastic, polycrystalline Ni55.6wt%-Ti with an average grain size of $\approx$ 87 µm. The map of austenite (cubic) grains and the grain orientation along the loading axis are shown in Figure 3.1(a).

(2) A schematic of the sample geometry is shown in Figure 3.1(d). The sample gauge section is 25mm x 3mm and the gauge is $\approx$ 0.5mm thick.

(3) In the center of the gauge, two holes are drilled into the sample as schematically shown in Figure 3.1(e, left). The hole diameter is 564 µm with the center-to-center spacing of 970 µm. The hole size and the spacing are chosen to be within one order of magnitude of the mean grain size.

Mechanical testing is done at an engineering strain rate of $\approx 10^{-3}$ /s using a Sintech 20G load frame. The sample is loaded in uniaxial tension for 100 load cycles to a nominal axial strain of 1%, as measured by a 10mm extensometer with knife around the center of the sample gauge section. The sample is removed from the load frame after 10, 20, 50 and

100 cycles for imaging of any cracks. The imaging is performed using a FEI Quanta 600F scanning electron microscope (SEM).

3.2.2. Simulations Using a Micromechanics based Model

A microstructural finite element (FE) model for phase transformation by Manchiraju and Anderson is used to perform the simulations [**76**]. Key features of the model are summarized below.

(1) Each element is modeled as an austenite single crystal with three deformation mechanisms:
   (a) Anisotropic linear elasticity in the austenite and martensite phases
   (b) Martensitic phase transformation between austenite (cubic, B2) and martensite (monoclinic, B19') phases at the habit plane variant (plate) scale.
   (c) Plasticity in austenite in the framework of crystal plasticity. Six $\langle 1\,0\,0\rangle/\{1\,1\,0\}$ and six $\langle 1\,0\,0\rangle/\{0\,1\,0\}$ B2 slip systems are considered.

(2) The inputs to the model, reflecting the deformation mechanisms described above, are:
   (a) **Elasticity**: Elastic constants and thermal expansion co-efficients for the martensite and austenite phases.
   (b) **Phase Transformation**: Equilibrium transformation temperature, latent heat of transformation per unit volume, coefficients of a phenomenological hardening matrix accounting for plate-plate interaction, and the critical energy barrier for austenite to martensite phase transformation (which is assumed to be equal in magnitude but of opposite sign for martensite to austenite reverse transformation).

(c) The input also includes the crystallographic orientation at every material point.

(3) Based on a prescribed deformation, final outputs of the model are the stress tensor and the martensite plate volume fractions at each integration point in the FE model.

The goal of this work is to model the transformation characteristics around structural features at relatively low loads. Therefore, we suppress plasticity by setting the critical resolved shear stress to a very high value (1000MPa). The equilibrium transformation temperature is set from differential scanning calorimetry (DSC) testing done on the experimental sample, as described in [**101**]. Representative values for other material parameters in the simulations are listed in Table 1 in [**76**].

Since the majority of deformation of similar samples in [**101**] is observed to be concentrated around the holes, a rectangular region localized around holes was modeled using Abaqus FE software. First, the average grain size from Figure 3.1(a) was used to tessellate the model with grains. The grains in the model were assumed to be columnar through the thickness. Second, a mesh comprising tetrahedral elements (C3D10M in Abaqus notation, 10 integration points, bilinear interpolation) was created. Finally, every grain was assigned a particular orientation and all elements located within a tessellated grain were identified and assigned that same crystallographic orientation, to simulate a polycrystal specimen. The mesh was created such that it is fine ($\approx$ 225 elements per grain) near the holes where most of the deformation is concentrated and coarser (up to 5 elements per grain) away from the holes as shown in Figure 3.1(e, center schematic). One end of the rectangular model was held stationary while a constant displacement (at a similar rate to the experimental loading) was applied on the other edge, to simulate uniaxial tensile loading.

Using this model setup, two simulations with the same model geometry described above, but different hole geometry, as shown in Figure 3.1(e) were considered to model the interactions between structure and microstructure.

(1) **Simulation 1**: A 25 mm x 3 mm x 0.25mm gage section with a random grain orientation distribution was used in this simulation. This resembles actual porous materials in polycrystals, by including 8 holes of varying sizes (100 µm, 200 µm and 400 µm) and separations arranged in a staggered manner through the central part of the specimen, as shown in Figure 3.1(e, right schematic). A tessellation is performed on the surface of the specimen, using the average grain size obtained from EBSD and extrapolated through the thickness of the sample assuming through-thickness grains.

(2) **Simulation 2**: This simulation consists of only two holes in the model as a highly idealized representation of a porous SMA specimen. The model in this case represents the same 25 mm x 3 mm x 0.25mm gage section as in the above case. The diameter of each hole is 150 µm and the center-to-center hole separation is 300 µm(Figure 3.1e, left schematic). Two separate instances of this case are considered. In the first instance, a specimen with a random orientation distribution is used, to mimic a polycrystal with random texture. In the second instance, the orientation of selected grains above one of the holes is changed so that the resultant grain orientations highly favors phase transformation in the loading direction. These two instances are described further in Section 3.3.2 (Figure 3.3).

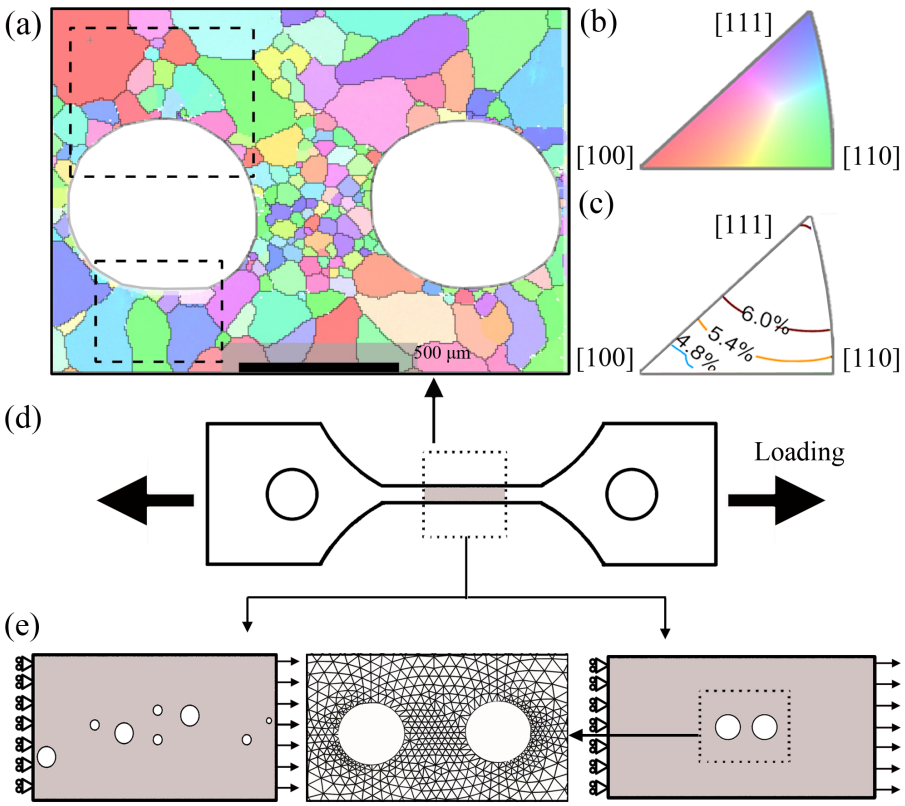

Figure 3.1. Schematic of experimental and virtual specimens. (a) Orientation map of the experimental sample with holes with (b) the color key for orientations with respect to the loading axis. (c) The dependence of theoretical axial transformation strain on orientation, based on calculations from the Crystallographic Theory of Martensite [**11**]. (d) Schematic of the experimental specimen with arrows showing the loading direction. (e) Sample geometry and boundary conditions used in the simulations. The left and right panels show the hole structure in Simulation 1 and 2 respectively, while the central panel shows the mesh density used in Simulation 2.

3.3. Results and Discussion

3.3.1. Simulation: Structural Features Determine the Initiation Sites and Grain Orientations Determine the Continuity of High-strain Bands

Figure 3.2 shows the simulated axial strain around holes at four different nominal strain states in Simulation 1 described in the previous section. While the nucleation of large-strain bands begins directly at the sites of stress concentration viz. above and below the holes, the geometry of these strain bands itself is more complex. Figure 3.2(a) shows the initial load-free state and (b-d) show the propagation of the high strain bands in the regions around the holes. The sequence of strain states in Figure 3.2(b-d) shows tortuous, asymmetric, and occasionally discontinuous growth of strain bands with increasing loads. The grayscale contour indicates the simulated axial strain while the colored insets show the theoretical axial transformation strain inside the box in the gray contours. The theoretical strain depends on the grain orientation as indicated in Figure 3.1 (c).

The location of strain bands in "V" shape above and below the holes in the simulation is expected based on the theory of elasticity. Those sites are the locations of stress maxima. The observed complex geometry in the growth of strain bands can be rationalized based on the favorability for transformation of the grains that these bands encounter. The insets in Figure 3.2(b-d) show the theoretical axial transformation strain that individual grains can produce, using the Crystallographic Theory of Martensite [**11**]. Dependence of theoretical axial transformation strain on the orientation is shown in Figure 3.1(c) and, in general, in NiTi, grains with [1 1 1] and [1 1 0] directions oriented with the loading direction produce a larger transformation strain and are therefore easier to transform compared to [1 0 0] oriented grains. The black arrows in the insets in Figure 3.2(b-c) indicate the direction of propagation

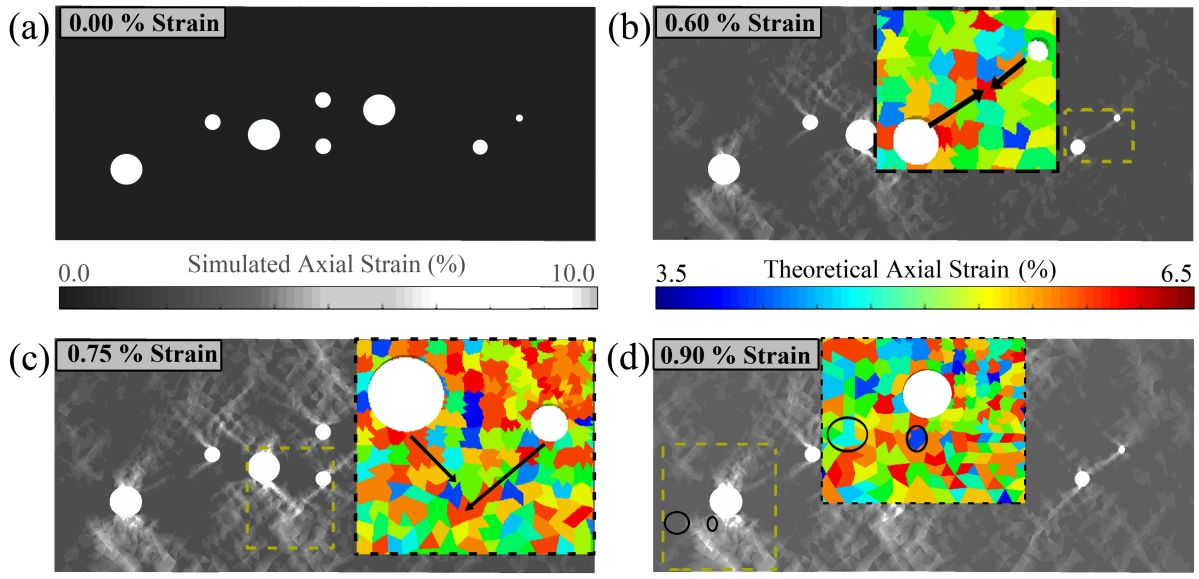

Figure 3.2. Simulated estimates (grayscale contours) of axial strain from Simulation 1, with the theoretical axial transformation strain for the boxed region indicated by the colored plots. (a) shows the entire specimen in the initial load-free state. Grayscale contours in (b-d) show different snapshots of (a) at increasing nominal macro strains: (b) at 0.6%, (c) at 0.75%, and (d) at 0.9%. The colored insets in each sub-figure (b-d) show the theoretical axial transformation strain for the boxed region similar to that shown in (a). The dependence of theoretical transformation strain on orientation is shown earlier in Figure 3.1(d). The loading in all sub-figures is along the horizontal direction. The black arrows in the insets show the direction of propagation of strain bands from nucleation spots. The ellipses in (d) indicate where high strain bands either completely stopped or grew around unfavorably oriented grains.

of the bands. When a propagating band encounters a highly unfavorable grain, there are two possible outcomes. As seen in Figure 3.2(d), if the grain is small enough, the band can grow around the grain and continue propagating, as indicated by the ellipse just below the hole. However, if the grain is large enough, it completely stops the growth of the band in that direction, as shown by the ellipse near the bottom left of the hole. In this latter case, we have observed that typically a different strain band nucleates and grows from nearby,

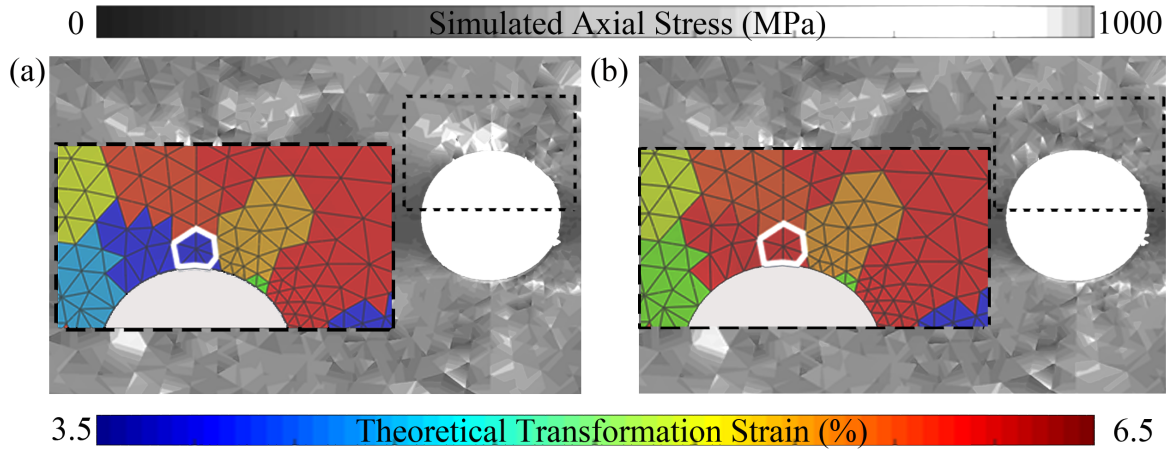

Figure 3.3. Results from Simulation 2 showing stress relief near holes when grain orientations are changed. The grayscale contour shows the axial stress from simulations while the colored contour is the theoretical transformation strain, which depends on the orientation according to Figure 3.1(c). In (a), the stress maximum in the sample corresponds to a grain producing relatively small theoretical axial transformation strain is situated above the hole (inset, blue color with white border), due to inefficient transformation. In (b), when the orientation of that grain is changed to favor transformation(inset, red color with white border), the stress is relieved as shown above the hole by the dotted box.

in a different direction, based on an efficient pathway in its neighborhood. Thus branching strain bands can be seen in the lower-right portion of Figure 3.2(d). A similar observation was made by Richards et al. [**108**]. They observed phase transformation spreading between favorably oriented grains with slip acting as a bridge in unfavorably oriented grains for phase transformation.

3.3.2. Simulation: Local Orientations can be Tailored to Relieve Stress Concentrations

The results in the previous section demonstrate that in SMA specimens where the pore size is comparable to the grain size, the stress-concentration and the growth of strain bands can be

heterogeneous. Thus, site-specific control of microstructural features such as crystallographic orientation can be used to alter stress states in specific regions of the sample. This section shows a specific example of this idea.

Figure 3.3(a) shows the simulated axial stress at 1% macro strain in Simulation 2, when the grain orientations are assigned randomly and the average grain size is obtained from the experimental sample. There is a stress concentration above the hole in a region where an unfavorably oriented grain is located, demarcated by a white outline and also observed in the grayscale axial stress map. The inset shows theoretical axial transformation strain for the grains. The stress concentration site coincides with the location of the grain that produces 3.5% axial transformation strain. In the second instance of the simulation, the results of which are shown in Figure 3.3(b), the crystallographic orientation of this grain is changed so that it is now favored for transformation, producing 6.5% axial transformation strain. Therefore, in case (b), after switching the orientation, the grain transforms easily and the stress concentrations above the hole in (b) are relieved. Tailored material design to proactively target grain orientations in regions of anticipated local stress concentrations might have favorable influence on the cyclic loading performance of porous SMA components. This is a concept that merits further study to advance a further understanding of the effect of such tailored microstructures. In steels – materials that deform by plasticity – change in pore shape from a circle to an 'S' shape increased the fatigue life due to reduction of local stresses [**52**]. In SMAs however, the promotion of local transformation to relieve stresses as demonstrated in this section may also lead to local transformation-induced slip, leading to an accumulation of defect content over many cycles, which can lead to functional fatigue.

3.3.3. Experimental: Stress Concentration Determines Crack Nucleation and Grain Structure Influences Crack Growth

The previous subsections used a simulation-based approach to explore the influence of grain orientation on strain localization and a way to reduce local stress by orientation engineering. In this section, we use an experimental approach to show how orientations also influence crack growth. These results are from the investigation of crack growth over 100 cycles up to a nominal axial strain of 1%, as described in Section 3.2.1.

Figure 3.4(a) shows the EBSD grain maps with SEM images of crack growth superimposed on them (b-d) for the experimental sample after 20, 50, and 100 cycles. The region shown in this figure is coincident with the bottom-left quadrant of Figure 3.1(a), shown by the dotted box. In this region, two cracks are visible: one in the cyan colored grain (numbered 1) and another in the green colored grain just to the right (numbered 2). The crack through Grain 1 does not show significant growth during cycling. With an orientation between [1 1 0] and [1 1 1], Grain 1 is oriented favorably for phase transformation and slip in austenite phase under uniaxial stress along horizontal direction. Thus it is plausible that the stress state is more relaxed under peak load due to profuse phase transformation, thus stopping crack growth. On the other hand, the crack through Grain 2 grows continuously during cycling, interrupted by small, black inclusion particles and following a tortuous path. In both cases, a band-shaped deformation structure is visible around the cracks.

Figure 3.5 shows the crack growth observed in the dotted box in the top-left quadrant of Figure 3.1(a), at the end of 20, 50 and 100 cycles. In this case, one major crack in the center region grew through the aquamarine-colored grain (numbered 1) into the green grain (numbered 2). The crack followed an approximately straight path through the Grain 1 at

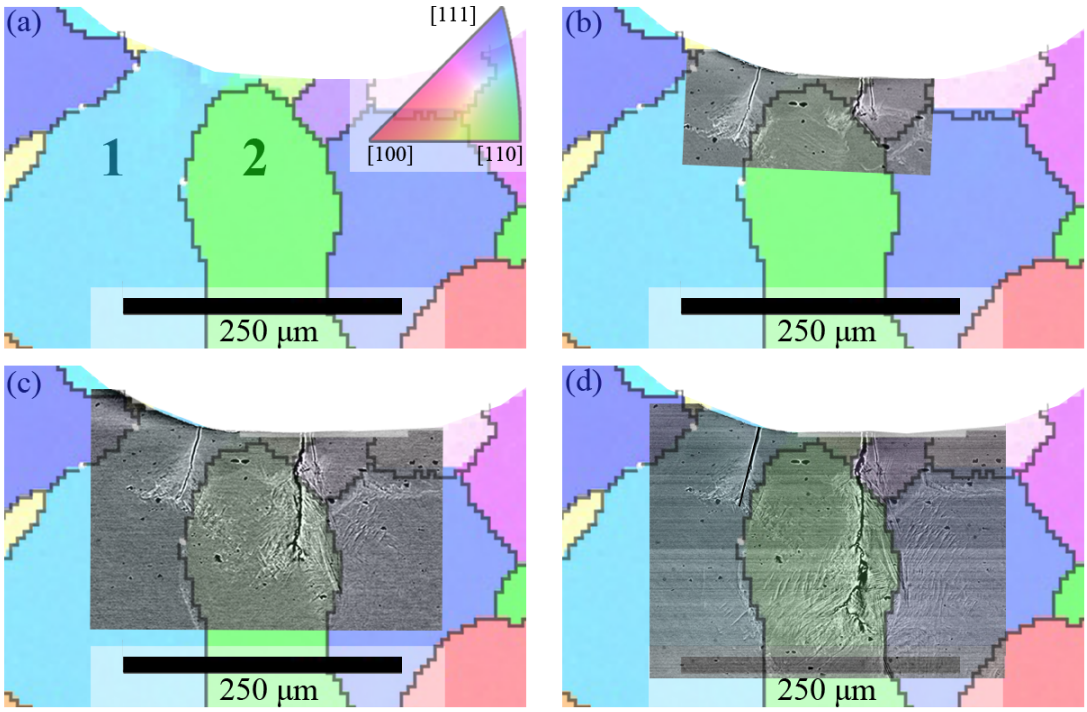

Figure 3.4. Crack growth in the bottom left quadrant indicated by the dotted box in Figure 3.1(a). (a) Grain orientation with respect to the leading axis. The standard coloring scheme, as shown in the key in Figure 3.1(b) is used. Crack geometry, as seen using *ex-situ* SEM, is superimposed on the grain orientation map after (b) 20 cycles, (c) 50 cycles and (d) 100 cycles. The crack in cyan grain, numbered 1, does not grow. The crack in green grain (numbered 2) grows, however it encounters inclusions (dark spots).

an angle of $\approx 75^0$ to the loading axis and then through Grain 2, at an angle of $\approx 60^0$ to the loading axis. These angles correspond to $\{1\,1\,0\}$ type planes in the respective grains. Gall et. al. [**41**] showed that fracture in NiTi takes place through cleavage along $\{1\,0\,0\}$ and $\{1\,1\,0\}$ planes. The straight nature of the crack growth suggests crystallographic fracture along a $\{1\,1\,0\}$ type plane. This observation is in contrast with the previous result, where the crack follows a tortuous path which we postulate is due to the presence of inclusions in its path in that case, as seen by Vaidyanathan et al. [**131**].

To the left of the hole in Figure 3.5 are red grains, which, according to Figure 3.1(b) are close to a [1 0 0] orientation from the loading axis. According to Figure 3.1(c), such grains are characterized by a high transformation stress and low transformation strain (inefficient for transformation). Since this loading was conducted at relatively low loads (up to a peak nominal strain of 1%), it is not expected to show significant deformation due to the high activation threshold for transformation. This is confirmed by the SEM images, by a marked absence of a remnant deformation field around that region seen around cracks in Figures 3.4 and 3.5.

We also monitored the crack growth around the right hole in the experimental sample. Three cracks were observed close to grain boundaries and did not show significant growth over cycling while one large crack primarily grew through a large [1 1 0] type grain. These observations are largely consistent with the results presented for the left hole. However, a statistical correlation between grain orientation and propensity for crack growth cannot be made from these observations that considered a limited number of grains and two holes of fixed size. A more comprehensive program relating crack growth to grain orientations may follow the approach recently used to relate grain size and fracture resistance [**1, 69**]. This would involve tracking a larger number of cracks around a broader distribution of pore sizes, grains, and locations, for example in a sample similar to the virtual specimen in Simulation 1.

3.4. Conclusions

The goal of this work was to explore two mechanistic phenomena in a representation of porous NiTi shape memory alloys. The first phenomenon – strain localization around holes,

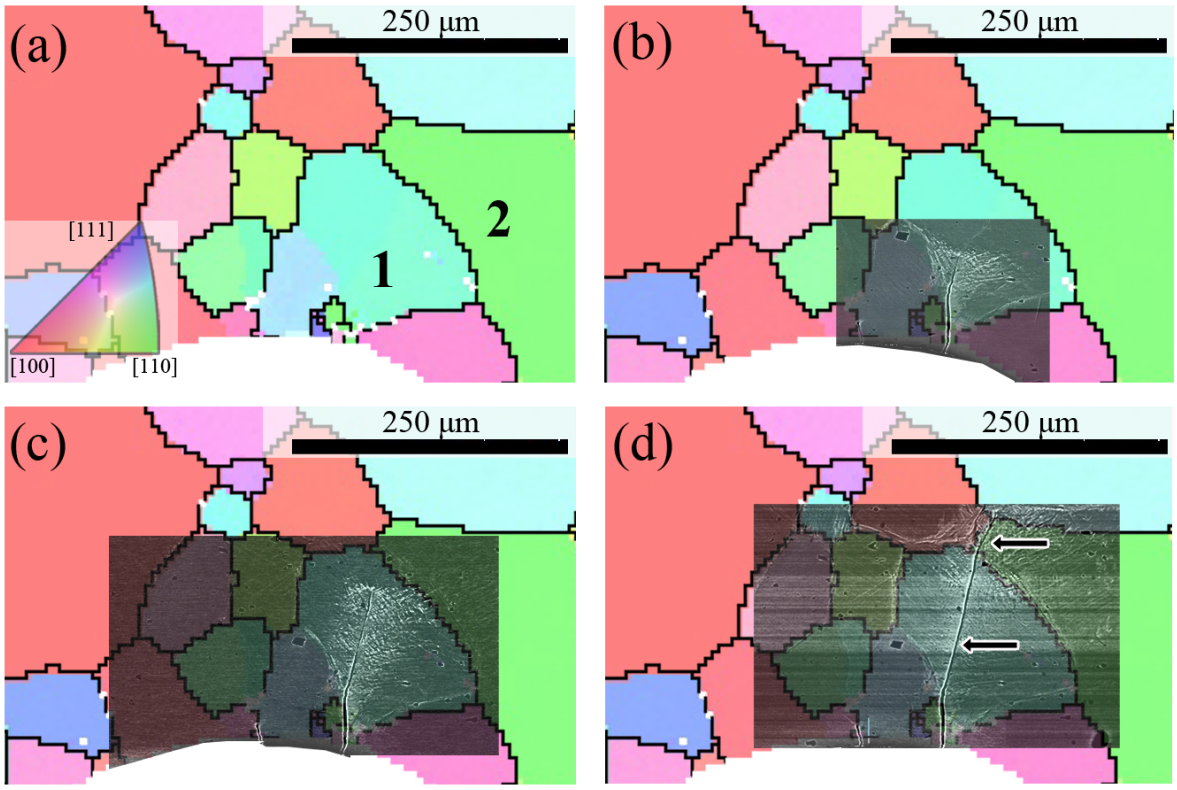

Figure 3.5. Crack growth in the top left quadrant shown by the dotted box in Figure 3.1(a). (a) Grain orientation with respect to the leading axis. The standard coloring scheme, as shown in the key in Figure 3.1(b) is used. Crack geometry, as seen using *ex-situ* SEM after (b) 20 cycles, (c) 50 cycles and (d) 100 cycles. The crack in the aquamarine grain (numbered 1) grows through a straight path through the entire grain, till it reaches a grain boundary and then continues to grow into the green grain (numbered 2). The arrows in (d) indicate the change in angle of the crack as it grows from Grain 1 to Grain 2. Residual deformation is seen around the crack.

was studied using a microstructural modeling approach. Relation between crack growth and grain orientation around holes was explored experimentally. The major conclusions are:

(1) The relation between hole location, grain orientation, and strain band formation is intuitive. Strain bands form at stress concentration sites around holes. However

their growth is enhanced by grains optimally oriented for transformation and impeded by unfavorably oriented grains. Thus the strain bands can fluctuate in strain and follow tortuous path.

(2) This strain band geometry dependence on the orientations can be used to relieve stress concentrations by introducing easy-to-transform grain in the path of the bands. Recent AM techniques may be able to achieve such orientation tailoring.

(3) The presence of large [1 1 0] type grains with respect to the loading axis is seen to provide the least resistance to crack growth in areas of stress concentration around the holes.

This work opens an avenue for engineering local crystal orientations to improve fatigue life of components made of materials that are highly anisotropic and heterogeneous in deformation. In the future, it will be interesting to experimentally explore a larger crack population to statistically uncover significant trends between the nature of crack growth and grain orientation, and a more comprehensive picture of polycrystalline fracture in porous shape memory materials. For reducing stress concentration around pores, a future additive manufacturing effort may develop a laser scan strategy that actually realizes the orientation changes discussed in Section 3.3.2.

CHAPTER 4

Interaction between Structure and Microstructure Determine Extent of Deformation in Nanoscale Phase Transformation

4.1. Introduction

An interesting manifestation of the interactions between structure (specimen size) and microstructure (grain size) was observed during compression loading of tapered cylinders of superelastic NiTi, where the average grain size was systematically varied with respect to the specimen size [**54**]. In this work, nanosized pillars are fabricated as tapered cylinders in the SEM, with a length of 1.5 µm, a top diameter of 688 nm and a taper of 5^0 with respect to the axis of the pillar. Multiple specimens were prepared in which the average grain size of cubic NiTi was systematically varied from 10 nm to 421 nm and taken through quasistatic uniaxial compression, to the same peak axial stress, followed by unloading. The range of grain sizes is chosen such that at its maximum size, the grain size approaches the specimen size. The major discovery of this work was the suppression of phase transformation in the specimens with large and small grains, with a grain size of 86 nm exhibiting the largest extent of deformation. When the same range of grain sizes was tested on larger sized pillars (top diameter of 1mm), there was a monotonic increase in the extent of transformation with the grain size, before saturating at large grain sizes (>150 nm).

The specimen with the smallest grain size, viz. 10 nm, shows a heavy suppression of phase transformation. This phenomenon of suppression of phase transformation with decreasing grain size at the nanoscale has been well investigated and attributed to various factors such

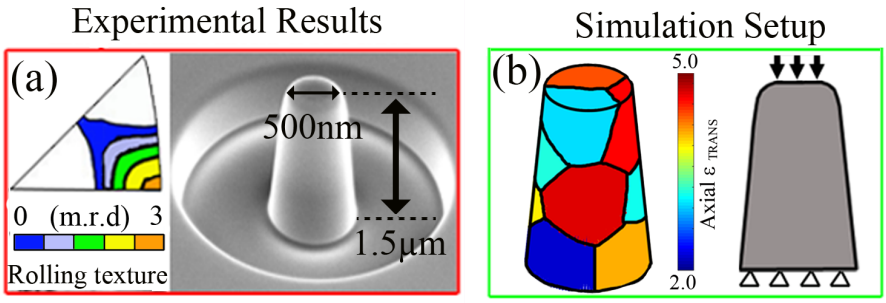

Figure 4.1. Set up of micromechanical simulations. (a) shows the experimental specimen used [**54**], along with the specimen crystallographic texture [**133**]. (b) shows the set-up of the micromechanical model, informed from the experiments. The left shows the specimen with 421 nm grains, with different colors indicating the transformation strain produced by the grain, according to the Crystallographic Theory of Martensite [**11**] while the right shows the loading boundary conditions.

as deformation by amorphization and an unfavorable energy landscape at the nanoscale [**2, 135, 38**]. Therefore, increasing the grain size also results in an increase in the extent of transformation, up to 86 nm. However, when the grain size is further increased beyond 86 nm, the extent of transformation decreases, right up to the maximum grain size of 421 nm. This non-monotonic trend of deformation with increasing grain size was attributed to the plausible interactions between the structure and microstructure across the specimens. This facet is explored in greater detail, through micromechanical simulations. In particular, the larger deformation exhibited by the 86 nm specimen compared to the 421 nm specimen, and the possible structural and microstructural reasons contributing to the suppression of deformation in the latter are explored.

4.2. Set up of simulations

To elucidate the mechanisms of the interactions between structure and microstructure in the compression micropillar, micromechanical simulations [**76**] were used to mimic the

deformation in the tapered pillars. As stated earlier, two specimens are modelled, with average grain sizes of 86 nm and 421 nm. Based on the average grain size, the total number of grains in the specimen was calculated and grains centers populated uniformly throughout the specimen. Using Voronoi tessellation on Matlab, grains were grown out from the grain centers. Since the experimental material was prepared by rolling, each grain was assigned an orientation from a list of orientations which gave an overall crystallographic texture that mimics the one obtained from rolling, as shown in Figure 4.1(a), as per [**133**]. Figure 4.1(b) shows a schematic of the setup of the simulations from the experiments, loaded under uniaxial compression. The bottom surface was kept stationary while the top surface was provided an axial compressive displacement, to mimic the experimental loading. To reduce the computational cost, the specimens were just taken through loading. The extent of deformation was then quantified through the total martensite fraction, which directly corresponds to the strain, which was used to quantify deformation in the experiments.

The modeling was done on ABAQUS, using an implicit analysis scheme. A mesh was constructed, using 82423 eight node brick elements (C3D8 in ABAQUS notation), which was used for both specimens. The material model was written as an implicit UMAT subroutine. Along with the material properties and parameters, this is described in detail in [**76, 93, 100**]. The deformation mechanisms considered are linear elasticity in the austenite and martensite phases and stress induced phase transformation from the austenite to the martensite phase. For simplicity, and to study the interactions between phase transformation and the specimen geometry and size, plasticity is switched off in the simulations.

4.3. Results and Discussion

Using the setup for simulations described above, the reasons for of the maximum deformation in the 86 nm specimen, as compared to the 421 nm specimen is explored in detail. A variety of factors are found to influence the deformation picture in these specimens, some of which are of microstructural origin and others of a structural origin. These factors are elucidated individually in detail in the following sections (4.3.1 - 4.3.4).

4.3.1. Effect of microstructural intra-grain variation of stress on deformation behavior

In polycrystals, the effect of grain boundaries as the initiators of deformation has been well documented. Using the micromechanical model employed in this work, the nucleation of phase transformation at grain boundaries and propagation into the grain interiors was shown in idealized grains [**95**]. The effects of constraints arising from grain boundaries and triple junctions on the deformation behavior of SMAs and the stress concentrations thereof has also been studied in detail [**128**]. Using a phase field model, the propagation of phase transformation into grain interiors from the boundary is simulated in [**75**]. In each of these cases, the stress concentration at a grain boundary causes the nucleation of deformation (phase transformation) which subsequently propagates into the interior of the grain.

Figure 4.2 demonstrates this progression of deformation on the (top) loading surface in the two specimens. The panel on the top left for each specimen indicates the theoretical axial transformation strain for each grain, based on its orientation with respect to the loading axis, as calculated by the Crystallographic Theory of Martensite (CTM) [**11**]. In the 421 nm specimen, the deformation is concentrated close to grain boundaries while the grain interiors

are comparatively undeformed. In the 86 nm specimen, the deformation to grain interiors is seen to have progressed to a larger extent, where certain grains are already transformed significantly (red) while certain grains show almost zero transformation (blue). This is consistent with observations on nucleation and progression of deformation in polycrystals [**2**]. In general, regions towards the interior of grains experience fewer constraints (leading to stress concentrations and increased deformation) from their neighboring elements as compared to regions of the grain close to boundaries. This is confirmed in Figure 4.3, where in general, elements in a grain closer to the grain center experience less deformation as compared to elements further from it (closer to boundaries), for a similar value of distance from the loading axis. With an increase in grain size, a larger number of elements lie in the grain interior and further away from grain boundaries, thus resulting in a decreased level of stress concentration (and deformation) for the grain as a whole. Larger grains also have regions in the grain interior, which are furthest away from any grain boundaries and are therefore at their most stress relaxed state, due to which propagation of phase transformation is harder.

Therefore, with an increase in the grain size, a larger portion of the grain lies in the grain interior and farther away from any stress concentrator such as a grain boundary, which contributes to a decreasing extent of deformation.

4.3.2. Effect of structural intra-grain variation of stress on deformation behavior

As specified in Section 4.2, the specimens are machined in the SEM as tapered cylinders. The $\approx 5^0$ taper is to minimize damage from the electron beam on the specimen during fabrication. The taper results in a cylindrical specimen with a continuously varying cross sectional area along the axial direction, as shown in Figure 4.1(b), resulting in a continuously decreasing stress field along the axial direction. Therefore, the loading surface on the top has a cross

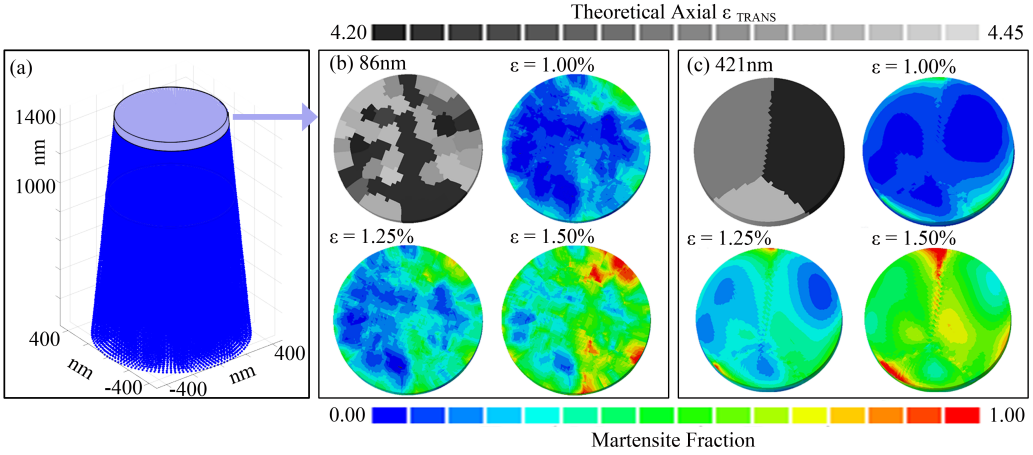

Figure 4.2. Intra grain variation of deformation. The progression of deformation is shown for the top section of the specimen, as highlighted in (a) with increasing loading for the two specimens (b) 86 nm and (c) 421 nm. The 86 nm specimen shows grains that are completely transformed into martensite, as compared to the 421 nm specimen where the deformation is largely limited to grain boundaries, without having propagated into the grain interiors.

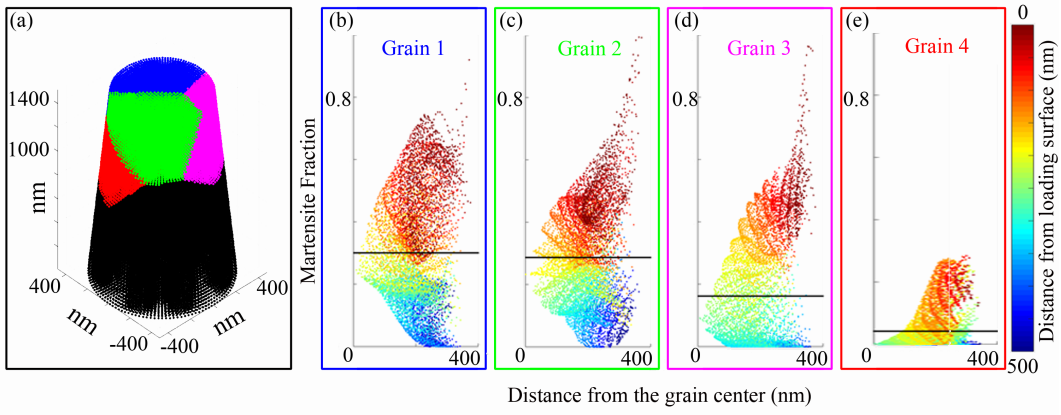

Figure 4.3. Effect of specimen geometry on deformation. The figure shows the variation of deformation, represented by the martensite fraction, in the four grains that show the largest extent of transformation in the specimen with 421 nm, highlighted in (a). The data points are colored according to distance from the loading surface. The solid black line indicates the mean martensite fraction in the entire grain. In general, regions far away from the grain center and closest to the loading axis show the maximum extent of deformation.

sectional area that is about a quarter of the cross-sectional area of the fixed surface at the bottom. This implies a stress distribution such that the stress on the top loading surface is four times that on the bottom, fixed surface, with a monotonic distribution of stress in between, based on the distance from the top surface. Figure 4.3 elucidates the strong relationship between the local deformation level inside a grain, quantified by the martensite fraction, as a function of its distance from the top loading surface, as well as distance from the grain center. Four representative grains from the 421 nm specimen are shown, which show the maximum deformation, that lie in the top half of the specimen. In each of these grains, more deformation within a grain is shown by regions that are:

(1) Closer to the loading se for a similar distance from the grain center.

(2) Farther away from the grain center for a similar distance from the loading surface.

The first point follows from the discussion in Section 4.3.1,which is of microstructural origin. The closer a region in a grain is to the grain center, the farther away it is from any grain boundaries or potential sources of elevated stress to nucleate and propagate deformation. The second point, which shows the dependence of deformation on distance from the loading surface points towards a structural influence on deformation.

Table 4.1. Dependence of intra grain variation of axial stress on grain size

Grain Size (nm)	Cross Section Diameter Grain Top (nm)	Stress Grain Top MPa	Cross Section Diameter Grain Bottom (nm)	Stress Grain Bottom MPa
421	688	σ	768	0.90σ
086	688	σ	704	0.98σ

For simplicity, in each of the two specimens, a representative grain is considered which starts at the top surface and has the same crystallographic orientation with respect to the loading axis. The top surface is assumed to be at a mean stress value of for both specimens. Based on the average grain size, the grain extends down to a distance of 421 nm and 86 nm from the top loading surface. Thus, the bottom of each grain lies in a cross-sectional area which is at a different lower stress level than the top. Table 1 quantifies this intra grain variation in stress with respect to the grain size. In the 421 nm and 86 nm specimens, the intra grain reduction in the stress along the axial direction is calculated to be 10% and 2% respectively. Hence, the larger the grain size, the more the intra grain stress reduction, resulting in a lesser average stress felt by a grain, for the same stress level on the loading surface. This difference in the axial stress variation is significant because the grain size approaches the specimen size. When the size of pillars in the original experiments in [**54**] is significantly larger (macropillars), an increase in grain size yields a monotonic increase in extent of deformation to saturation unlike micropillars, since the effect of the geometry

(taper) with respect to the grain size is not as significant when the specimen is much larger than the grain.

Therefore, the specimen taper with respect to the grain diameter contributes towards a general decrease in the mean stress experienced by a grain with an increased grain size when the grain size approaches the specimen size, thus contributing towards lesser extent of deformation.

4.3.3. Effect of number of neighbors on deformation behavior

After the structural and microstructural analysis of deformation within a grain, the effect of another microstructural constraint, in the form of effect of neighboring grains is examined in the two specimens. An earlier work on the effect of granular constraints from neighboring grains in superelastic NiTi under uniaxial tension revealed two key results [**97**]:

(1) The axial (elastic) strain increases with an increase in the number of neighboring grains.

(2) Over the specimen, surface grains are shown to show lower (elastic) strains in the axial direction as compared to interior grains, as shown in Figure 4.4(a). Surface grains have a smaller number of neighbors as compared to interior grains and therefore exhibit in a more relaxed state on average.

Figures 4.4(b, c) show histograms of the distribution of grains according to the number of nearest neighbors for each grain. The mean number of neighbors is higher in the 86 nm specimen, which also shows the largest extent of deformation. A larger percent (and number) of grains in the 86 nm specimen also have a greater number of nearest neighbor grains, as compared to the 421 nm specimen. In addition, in the 421 nm specimen, none of the grains

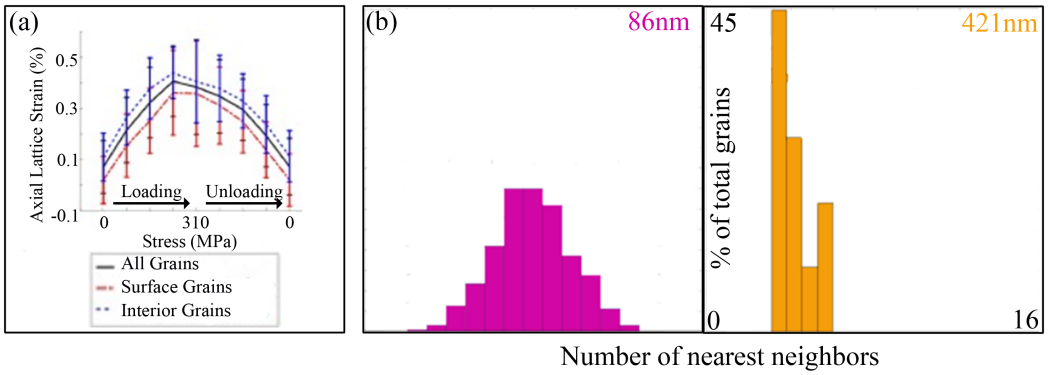

Figure 4.4. Effect of number of neighbors on deformation behavior. The number of nearest neighbors for every grain is calculated and plotted as a histogram, with respect to the percentage of total grains. (a) is adapted from [**97**], which shows the average axial elastic strains is higher for interior grains with respect to surface grains during phase transformation. On average, an interior grain has more number of nearest neighbors than a surface grain. (b) shows the distribution of nearest neighbors for the 86 nm and 421 nm specimens respectively. The 86 nm specimen shows the maximum deformation in both simulations as well as experiments and also corresponds to the highest average of nearest neighbors.

are interior grains. For simplicity, any grain that touches any of the lateral or top and bottom surfaces of the specimen is classified as a surface grain while all the other grains, that do not touch any external surface is an interior grain. On the other hand, the 86 nm specimen has 758 out of 1300 grains (58%) are interior grains while only 42% are surface grains.

Therefore, the percent of interior grains, along with the mean number of nearest neighbor grains is higher in the 86 nm *specimen, contributing towards a higher level of deformation.*

4.3.4. Effect of crystallographic texture on deformation behavior

The specimens have a strong rolling texture from the material processing, as shown in Figure 4.1(a). The effect of this texture on the deformation response is examined by comparing the behavior of the textured specimen (Figure 4.5(b)) versus the behavior of two other

specimens with the same average grain size, but with a random polycrystal texture (Figure 4.5(c, d)). The effect of crystallographic texture on superelastic behavior of SMAs has been explored in detail through experimental and simulation-based efforts [**12, 144, 121, 80**]. The crystallographic texture in polycrystalline NiTi used to explain the difference between tensile and compressive behavior [**40**]. The role of rolling texture on the recovery strain and hysteresis during superelastic loading of NiTi is examined in detail by contrasting the deformation behavior along and transverse to the rolling direction [**72**]. Figure 4.5 elucidates the effect of the crystallographic texture on the compression response in NiTi micropillars, in the specimen with the largest grain size, viz. 421 nm. In general, the specimen with the rolling texture shows the maximum amount of deformation, compared to both specimens with the polycrystal texture. This also follows from the crystallographic theory of martensite [**11**], which predicts the transformation strain produced by a grain during phase transformation to the monoclinic phase, based on its orientation with respect to its loading direction. In general, the minimization of energy principle dictates that the ease of transformation directly depends on the amount of transformation strain produced, which is shown to depend on orientation with the loading axis as shown in Figure 4.5(a).

Figures (b-d) show the extent of deformation, in terms of the martensite fraction for three cases: (b): rolling texture, (c, d): random polycrystal texture. The colored contour on the right in each sub-figure shows the grains and the theoretical axial transformation strain shown by each grain. The specimen with the rolling texture, (b), has grains that all have orientations that produce large transformation strains (orange-red contours) whereas the random polycrystal samples have grains in cyan-blue, which produce a much lower transformation strain. The rolling textured specimen, also shows the largest amount of deformation, compared to the other two specimens. In between specimens (c) and (d), the top loading

surface in (d) contains grains that produce a relatively higher transformation strain, as compared to (c), and also shows a more progressed stage of deformation. Thus, the texture is seen to have an effect on the deformation response, in particular the extent of deformation. However, the texture increases the deformation level across all grain sizes and therefore is not an important contributing factor to the decreased deformation at larger grain sizes.

Therefore, the crystallographic texture in the specimen is seen to affect the deformation response in the material, across all specimens. However, it cannot explain the variation in deformation response across specimens with the same texture and different grain sizes.

4.4. Conclusions

The interaction between structure and microstructure, in the form of specimen size and average grain size was studied in compression micropillars of superelastic NiTi. In particular, the deformation in two specimens, one with a large grain size and another with a small grain size are analyzed, using a micromechanics-based simulation. The following reasons are found to influence deformation, when specimen and grain size are comparable, in similarly sized specimens:

(1) The microstructural intra grain variation of deformation leads to a higher deformation with a lower grain size. In particular, with an increasing grain size, a larger percent of the grain lies in its interior and away from any grain boundaries, contributing towards a lesser deformation.

(2) The structural intra grain variation of deformation leads to a higher deformation with a lower grain size. The geometry of the specimens is a tapered cylinder, leading to different cross-sectional areas and stresses along the loading axis. With

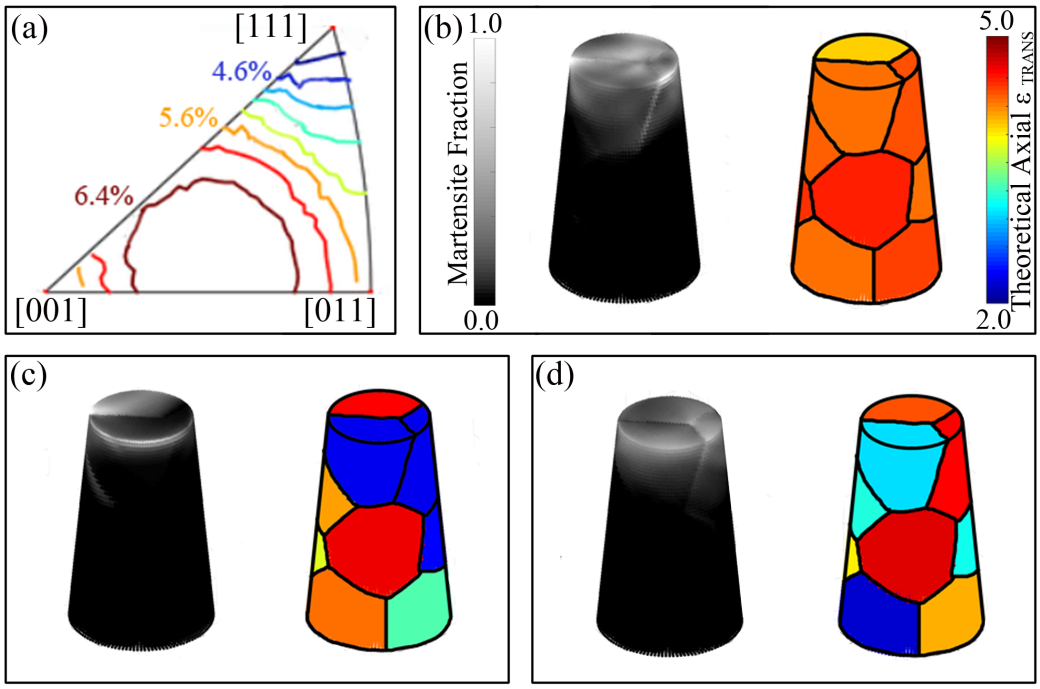

Figure 4.5. Effect of specimen crystallographic texture on deformation. (a) shows the contour of axial transformation strain produced on transformation from cubic to martensitic NiTi, as predicted by the Crystallographic Theory of Martensite [**11**]. (b) shows the deformation in the specimen with rolling texture while (c) and (d) show the deformation response in specimens with a random texture. In (b-d), the grayscale contour on the left shows the overall martensite fraction in the specimens at peak load, while the colored contour on the right indicates the theoretical transformation strain produced in the axial direction, calculated from (a).

larger grains, this variation is larger. This results in a lowering of the mean stress experienced by a grain with an increase in the grain size.

(3) The effect of neighboring grains and granular constraints thereof contribute to a higher level of deformation in a specimen with smaller grains. This is due to the combined effect of a larger number of grains having a larger number of neighboring grains, as well as less surface grains, which exist in a relaxed state due to fewer constraints, compared to interior grains.

(4) Finally, the crystallographic texture due to rolling on the experimental specimens is seen to increase the extent of deformation, compared to random polycrystals. However, this does not account for difference in behavior of specimens with the same texture but different grain sizes.

4.5. Acknowledgements

Prof. Qingping Sun and Dr. Parham Kabirifar are acknowledged for providing the experimental data, along with valubale discussions and inputs. Dr. Sivom Manchiraju and Prof. Pete Anderson are acknowledged for providing the UMAT subroutine used in the simulations. Dr. Harshad Paranjape provided valuable guidance on using the micromechanical model. The computational work used the Extreme Science and Engineering Discovery Environment (XSEDE), supported by National Science Foundation (ACI-1053575).

CHAPTER 5

Interactions between Structure and Microstructure Determine Heterogeneous Evolution of Deformation in Low Symmetry Phases

5.1. Introduction

Deformation in materials with a hierarchical microstructure is expected to be complex because of the interaction between the units that form such a microstructure [**84**]. One can contemplate that the complexity of deformation would be even higher when additional inelastic deformation modes are active in such materials, apart from traditional elastic and plastic deformation modes. Shape memory alloys (SMAs) are a class of metallic materials that exhibit a nano- to macro-scale hierarchy in the microstructure. The low crystallographic symmetry martensite phases in SMAs exhibit both – a hierarchical microstructure and multiple inelastic deformation modes such as twinning, detwinning, nanocrystallization and amorphization. The monoclinic (B19′) martensite phase in Nickel-Titanium (NiTi) SMAs is one specific example of such low symmetry phase. A typical martensitic NiTi microstructure consists of micro-scale crystallites. The crystallites themselves consist of nano-laminates with internal twin structure consisting of crystallographic variants.

The deformation mechanics of monoclinic martensite in NiTi has received attention at primarily two individual length scales. On one hand, at the macro scale, experimental efforts based on X-ray diffraction and neutron diffraction have attempted to quantify the evolution

in texture and strains due to specific twinning modes during thermomechanical deformation of martensitic NiTi. Using X-ray diffraction, the dynamic evolution of martensitic texture under load biased thermal cycling is quantified [**53**]. Using neutron diffraction, the contribution of twinning modes and plastic slip to the overall deformation strain in monoclinic NiTi was quantified. Whereas a self accommodated martensitic microstructure is seen to develop strengthening textures with increased tensile loading [**120**], the texture of stress induced martesnite is seen to exhibit decreasing texture with increased loading, due to constraints arising from crystallographic compatibility [**130**]. On the other hand, at the nano scale, scanning and transmission electron microscopy (SEM/TEM/STEM) based efforts have attempted to capture the evolution of nano-scale twin structure at the individual crystallite level [**134**]. Using a combination of Digital Image Correlation (DIC) and optical microscopy, localized strain concentrations were linked to deformation of martensitic NiTi through reorientation by observing the movement of junction planes, lying at the intersection of twin plates of martensite [**67**]. Similar to a similar works at the macroscale, the crystallite nanoscale picture of change in inelastic and plastic deformation modes with increased loading [**42**] and directionality of loading [**74**] was studied in twinned SMA microstructures.

In addition to such a hierarchical microstructure in SMAs, another source of interest in studying the deformation response is the presence of stress-concentrating features such as notches, cracks, or holes. The deformation picture around these stress concentrators arise from their complex interactions with the microstructure [**86, 100, 101**]. Specifically, in martensitic NiTi, while the path and the growth rate of a crack front would depend on the deformation mechanics of the twinned microstructure, there is evidence that a growing crack in superelastic NiTi may in fact be growing in single phase martensite. Few efforts in the literature have attempted to quantify the martensite microstructure evolution in the presence

of stress concentrating structural features. Using synchrotron powder X-ray diffraction, it has been shown that the crack in martensitic NiTi grows through a microstructure that is primarily detwinned martensite phase [**44**]. Using a similar characterization technique, an increase in loading is seen to induce an increasingly textured martensite in the vicinity of a crack in martensitic NiTi [**33**]. Intuition suggests that the stress concentration near crack-tips, notches etc., would cause a collapse of the hierarchy in the martensite microstructure and lead to the formation of a single crystallographic variant. This is because the twin-forming crystallographic variants in NiTi martensite can reorient at relatively low stresses to the crystallographic variant favored by the external stress.

In this work, we seek to characterize the evolution in the martensite microstructure hierarchy in the presence of a stress concentrating feature in the form of a notch. Specifically, we seek to answer the question if the twinned microstructure of martensite coarsens in length scale such that large individual crystallographic variants are present in front of the notch under load. This aspect of martensite deformation has implications to the modeling of crack growth in martensite. Since the monoclinic martensite in NiTi has anisotropic elastic properties, a coarse variant structure in front of cracks or notches would require that the crack growth be simulated using microstructural modeling frameworks that operate at the individual martensite variant scale and account for the anisotropy [**95, 70, 145**]. However, if the microstructure maintains the nano-scale twinned hierarchy, then perhaps coarse-grained models that blur out the individual variant structure can be adequate to model the crack-tip deformation phenomena [**125**].

To characterize the martensite microstructure evolution across the complete hierarchy, we used digital image correlation at the macro-scale, high-energy X-ray diffraction at the micro-scale, and TEM at the nano-scale. We also used simple elastic simulations to capture

the stress concentration around the notch. These methods are described in Section 5.2. The key results are presented in 5.3. Finally, we discuss the observed evolution in martensite microstructure and its implication to the modeling of crack-tip mechanics in NiTi SMAs in 5.4.

5.2. Materials and Methods

5.2.1. Material and Specimen Preparation

The material used is an equiatomic NiTi SMA (Ni-49.8 at.%Ti, determined using energy dispersive spectroscopy). The transformation temperatures of the material, calculated using Differential Scanning Calorimetry(DSC) were found to be $M_f = \approx$ -3^{0}C, $A_s = \approx 31^0$C and $A_f = \approx 45^0$C, meaning the material is completely martensitic below $\approx$ -3^{0}C and completely austenitic above $\approx 45^0$C. The material is grown as a single crystal in the cubic austenitic phase at $\approx 400^0$C using the modified Brigdman method and cooled down to room temperature, as described in [**20**]. While cooling to room temperature, brittle carbides and oxides (henceforth referred to as inclusions) of Ti, primarily TiC and TiO_2 formed throughout the material. These have been observed in NiTi SMAs, usually present in networks that span lengths from 1 µm - 100 µm [**96**].

A dogbone specimen was machined from from this material, with the dimensions indicated in Figure 5.1(a). The gauge section of the specimen is 1mm $\times$ 1mm $\times$ 1mm. The specimen is initially detwinned under uniaxial tensile loading, to a load of $\approx$ 350N, peaking at an axial strain of $\approx$3.8%. A single edge notch was machined at the center of the gauge section of the specimen using wire electrode discharge machining, with the dimensions of the notch specified in Figure 5.1(b). The notch was machined to localize the deformation at the center of the gauge section. These specimens were then dipped in liquid nitrogen

for $\approx$ 15 minutes, to ensure the specimen is fully martensitic, after which the experiment was performed at room temperature (A_s = (31^0C)). In the later sections, with the zero load X-ray diffraction patterns confirm martensitic NiTi as the predominant phase (Figure 5.1(c)).

5.2.2. High Energy X-ray Diffraction Microscopy (HEDM) and Loading Set-up

The in situ HEDM was performed at Beamline F2 at the Cornell High Energy Synchrotron Source (CHESS). A box beam of width 1.5mm and height 120 µm, with a monochromatic energy of 55.618 keV was focused on the specimen gauge. Five diffraction layers of thickness 120 µm, numbered Ⓐ - Ⓔ, with a center to center spacing of 100 µm were scanned around the notched center of the specimen, as shown using the shaded boxes in Figure 5.1(b). The spacing between layers is chosen such that there is an overlap of 10 µm between every layer and its immediate neighbor. The detector was located at a distance of 1046.929mm from the center of the specimen gauge. Calibration of the specimen to detector distance and detector tilt was performed using a stainless steel specimen, as described in [**96, 97**]. The complete list of calibrated parameters is included in the Supplementary Data in Tables .1 and .2 in Section 1.1. Uniaxial tensile loading was then performed on the specimens at room temperature under load control, using the RAMS2 load frame [**114**]. The specimen surface relief was used to take images of the central notched region during loading and unloading. Digital Image Correlation (DIC) was then used to obtain surface strain maps from these images around the notch. Loading was paused at constant load at various points during loading and unloading to conduct HEDM scans, as indicated by the red colored dots on the nominal load-strain curve in Figure 5.1(d).

At each of these points, the top diffraction layer Ⓐ (indicated by red in Figure 5.1((b) was scanned by rotating the load frame 360^0 about the loading axis. At every 0.1^0, a diffraction snapshot was collected, with an exposure of 0.1 seconds. Thus, for every diffraction layer, 3600 diffraction patterns were collected, corresponding to the microstructure at every 0.1^0 of rotation. Then the base stage of the load frame was moved vertically upwards, in the loading direction, to scan the next layer similarly, till the bottom (violet) layer Ⓔ was scanned. After each loading/unloading increment, the specimen was centered using X-ray tomography such that the notch center was centered with respect to the X-ray beam, before taking the HEDM scan. This ensures that roughly the same volume of material is being investigated over all diffraction scans. The scans were taken at loads of ① : 0N, ② : 100N, ③ : 200N and ④ : 350N during loading and ⑤ : 150N, ⑥ : 0N during unloading. After complete unload, the specimen was again loaded, with a scan taken at ⑦ : 150N, and then further loaded till brittle fracture at $\approx$ **420N**.

5.2.3. Postmortem analyses

After fracture of the specimen, two broken halves were generated. Martensitic twins in NiTi have crystallographic elements at the nanoscale, several orders of magnitude below the length scale of HEDM analysis. Therefore, to complement the in situ HEDM data at the mesoscale, transmission electron microscopy(TEM) was used to obtain the postmortem deformation picture, at the nanoscale. Focused Ion Beam (FIB) milling was done parallel to the loading direction to generate lift-outs from the fracture surface and grip section of one broken half of the specimen, using a FEI Helios Nanolab Dual Beam SEM/FIB with an Omniprobe manipulator. TEM was then performed on the liftouts at three different regions, as outlined in Figure 5.7(b). The regions for performing the lift-out were selected

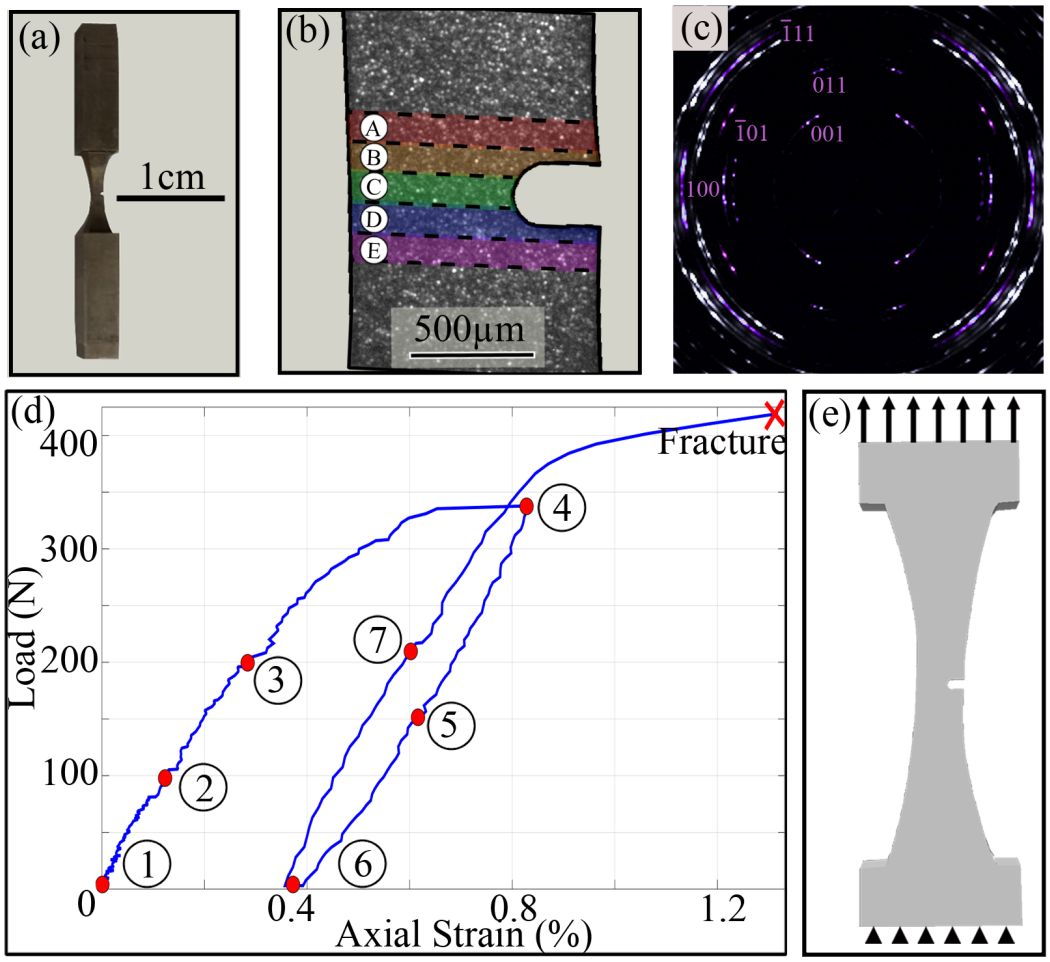

Figure 5.1. (a) shows the dimensions of the planar dogbone used in the tensile experiments. (b) shows a schematic SEM image of the notch tip at the center of the specimen in (a). The diffracted volume at the center of the specimen is indicated by the shaded box, with each of the five diffracting layers indicated by different colors, numbered Ⓐ - Ⓔ. (c) shows a sample diffraction scan taken at zero load of a 120 μm high volume of material. The five monoclinic rings selected for diffraction analysis ([0 0 1], [0 1 1], [$\bar{1}$ 0 1], [1 0 0] and [$\bar{1}$ 1 1]) are indicated by a pink hue. (d) shows the nominal stress strain curve for static loading of the specimen. The numbered red dots ① - ⑦ indicate the points at which loading was paused to take diffraction scans while the red cross at the end indicates the point of brittle fracture. (e) shows a schematic of the specimen used for the simulations, with the boundary conditions imposed for uniaxial tensile loading.

such that they lie in areas of different deformation from different areas of the specimen. TEM microscopy and diffraction was then performed using a Telos TEM (FEG, 200 kV), on a cross-sectional area perpendicular to the fracture surface (along the loading direction).

5.2.4. Analysis of Martensite Microstructure Evolution using HEDM Data

Before being mounted onto the RAMS2 load frame, a single HEDM scan was done at the center of the gauge section of the specimen. In HEDM, the Bragg spots lie along concentric Debye-Scherrer rings on the detector, with each ring corresponding to a different crystallographic plane (Figure 5.1(c), Figure 5.2). Since martensite is a low symmetry phase (monoclinic crystal symmetry), the rings are very close to each other and spots from consecutive rings start to overlap, especially at larger radii of the rings. Some rings from the martensite phase also lie very close to the location of rings from other phases (such as cubic or R-phase NiTi), which potentially reduces the confidence in uniquely assigning diffraction spots to one phase. Therefore, five rings of martensitic NiTi ([0 0 1], [0 1 1], [1 0 0], [$\bar{1}$ 0 1] and [$\bar{1}$ 1 1]) are chosen for the HEDM analysis, such that they are distinctly separated from each other as well as rings from other phases. These selected rings are labeled and highlighted in Figure 5.1(c) with a pink hue.

The lattice parameters for the monoclinic phase of NiTi are then found at this load free scan, using the MIDAS software suite [**115, 116**]. Using the calibrated experimental parameter suite and an initial set of lattice parameters for monoclinic NiTi from a previous study [**96**], the best match between simulated and experimental spots is found iteratively to convergence, varying just the lattice parameters. This process converges after 9 iterations, giving the stress-free lattice parameters as: $a = 2.89\,\text{Å},\ b = 4.11\,\text{Å},\ c = 4.65\,\text{Å},\ \beta = 96.95^0$

and $\alpha, \gamma = 90.00^0$. Subsequent analysis of the diffraction data was done using the heXRD software suite [**9**].

Next, using the calibrated experimental and material parameters, all orientations of crystallites present in the specimen are determined. A trial orientation set is defined, consisting of all orientations in the monoclinic space. Using forward projection given material and experimental parameters, simulated diffraction spots from each orientation in the trial orientation set are found and compared to the actual diffraction spots obtained experimentally. A *completeness parameter* is then defined, as the percentage of all predicted Bragg spots on the detector that are found experimentally for every orientation. A *completeness threshold* is then defined and used to filter out the all orientations whose completeness is below this threshold, from the complete monoclinic orientation space. The set of orientations remaining, after filtering out all orientations from the trial set based on the *completeness threshold* is referred to as the *observed monoclinic orientations*.

A major challenge of HEDM analysis of the low crystal symmetry martensitic NiTi arises due to it's inherent microstructure, with crystallite sizes spanning several orders of magnitude, a wide orientation spread across these crystallites at the length scale of HEDM and the multitude of deformation mechanisms available. Therefore, to correctly identify orientations given the streakiness of the spots, a multi step process was employed, to obtain orientations from deformation of the low crystal symmetry martensite phase in NiTi.

(1) First, the parameter that sets the *angular tolerance* for matching of the calculated diffraction spot to an experimental spot is set to a high value, such that multiple orientations can identified within every streak. This gives rise to a large number of identified orientations along every ring, for every layer and at every load step.

(2) Second, the *completeness threshold* is set to a high value of 80%, so as to only retain orientations that have an extremely high completeness, with all orientations below that threshold being discarded. Since the actual spots are large and streaky and are being compared against small and precise predicted spots, a very high completeness threshold helps in reducing the number of false matches. Even so, due to the low crystal symmetry, many orientations have their predicted spots lying very close to each other and within the defined *angular tolerance* along the rings. Therefore a large number of orientations are identified with a high completeness. At zero load, the average number of orientations identified per diffraction layer (1mm x 1mm x 120 µm) is more than 300. Further analysis of the experimentally obtained streaks reveal that the same 'spots' i.e. smaller portions of a streak corresponding to local intensity peaks, are assigned to multiple predicted orientations, due to the proximity of predicted spot locations of these orientations.

(3) Therefore, to circumvent this issue of the same spots being counted multiple times for multiple orientations, every orientation is assigned an intensity value, which is the sum of intensities of all experimental spots identified for that orientation. The orientations are then sorted in decreasing order of intensity, from most to least intense.

(4) From the sorted orientations, a list of *master orientations* is created, starting from the most intense orientation.

(5) For every successive orientation, if it is more than 10 degrees misoriented from all orientations already in the master list, the predicted spots from this orientation are expected to be adequately distinct from the master orientations. This orientation is therefore then appended to the end of the master orientation list.

(6) However, if there is at least one orientation already in the master orientation list which is less than 10 degrees misoriented from the current orientation, the predicted spots from these two orientations are considered not distinct enough to be separated from each other. It's closest neighbor inthe master orientation list is then identified and the intensities from all spots in the current orientation not already used in the master list are assigned to the nearest neighbor in the master list. This orientation, now left with no spots and zero intensity, is discarded. At the end of this step, every diffraction layer now has an average of $\approx$ 25-40 distinct orientations. As before, for every orientation in the completed master list, the intensity of that orientation is the sum of intensities of all spots belonging to that orientation.

(7) These orientations are then populated into a texture function, with each orientation weighted by it's intensity. This weighted texture function represents the distribution orientations of crystallites present in a diffracting volume and is visualized using pole figures along the loading direction, using the MTex package on MATLAB [**88**]. Therefore, the output thus far is a master list of monoclinic orientations, henceforth referred to as *observed monoclinic orientations*, and a texture function.

5.2.5. High Temperature HEDM to obtain parent cubic orientations

Post fracture and subsequent TEM analysis, the two halves of the specimen were individually put into the HEDM set-up again, at a temperature of 350^0C and at zero load, the set up of which is explained elsewhere [**91**]. Since this temperature is well above the A_f temperature of the material, the material exists purely in the parent cubic austenite phase. Diffraction scans with the same layer thickness are taken in the fractured gauge section of the specimen, to obtain the cubic orientations in roughly the same section of the material as the in

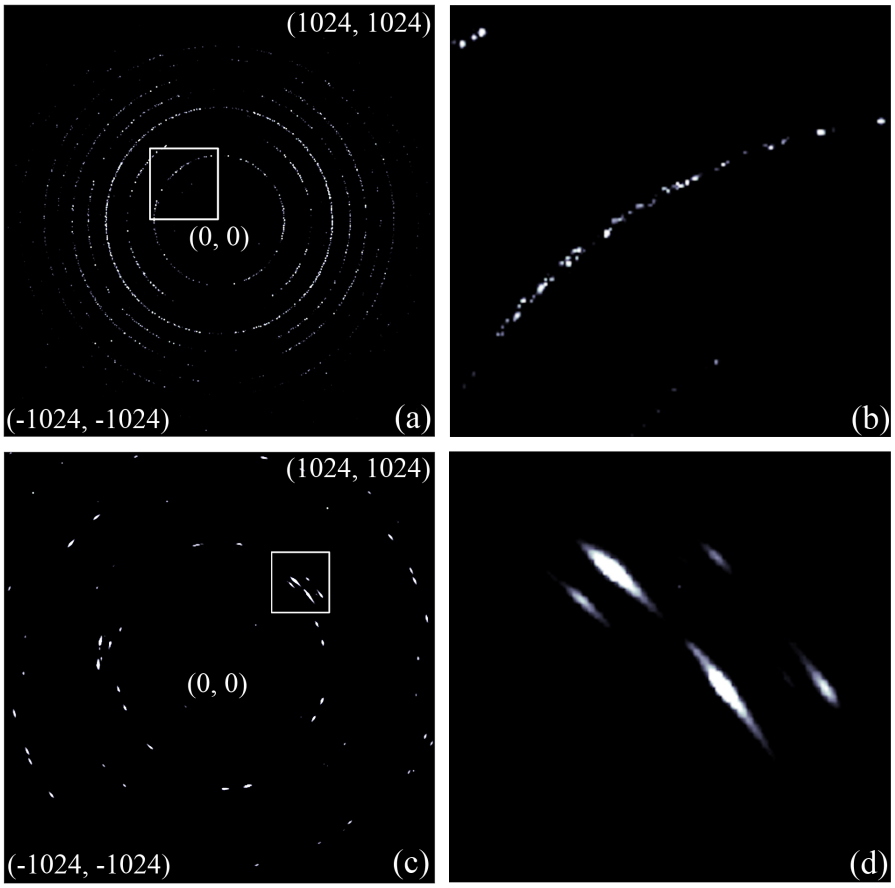

Figure 5.2. Comparison of HEDM far-field scans in (a) high crystal symmetry materials, viz. cubic NiTi phase and (b) low crystal symmetry symmetry materials, viz. monoclinic phase in NiTi. The diffraction patterns are shown over the entire detector, with 2048 x 2048 pixels, while the insets show the portions highlighted by the boxes. The cubic phase shows distinct spots while the pattern on the monoclinic phase is smeared over a wide angular range.

situ room temperature HEDM scan, which yielded the martensite orientations with loading. The complete list of calibrated parameters is included in the Supplementary Data in Table .2 in Section 1.1. A high completeness cut-off of 80% is used to only retain high fidelity cubic orientations from this high temperature scan. Using the Crystallographic Theory of Martenistic Transformation, as outlined by Hane and Shield [**47**], all 336 possible orientations (variants) of martensite, that can form from every cubic orientation obtained from

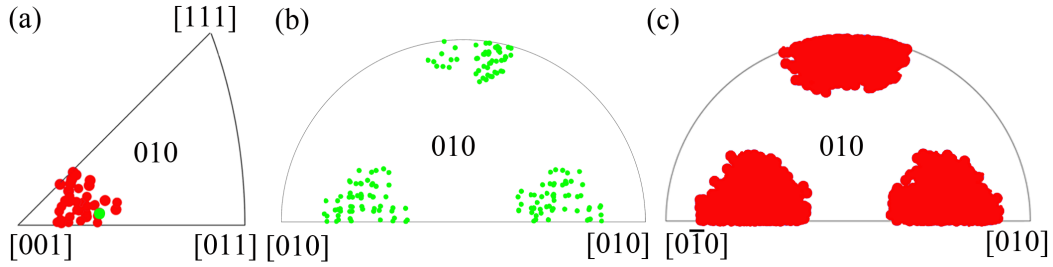

Figure 5.3. Variant Analysis. (a) shows the *parent cubic orientations* obtained from high temperature HEDM on an IPF along the loading axis. Using CTM [**46**], (b) shows all 336 possible monoclinic orientations from one representative cubic orientation highlighted in green in (a), plotted on a monoclinic IPF along the loading direction. (c) shows all possible *calculated monoclinic variants* from all the *parent cubic orientations* in (a), plotted on the same monoclinic IPF.

the high temperature HEDM are calculated. This set of martensitic orientations is henceforth referred to as the *calculated monoclinic variants*. Now, for every orientation in the *observed monoclinic orientations* calculated in the previous section, it's nearest neighbor in the *calculated monoclinic variants* set is found. If the misorientation between the observed orientation and it's nearest neighbor in the calculated variant set is less than 10 degrees, the *observed orientation* is assigned that particular *calculated monoclinic variant*. Thus, the number of unique *calculated monoclinic variants* and their corresponding intensities (directly proportional to volume) at every diffraction layer is then tracked, at every step during loading and unloading of the specimen where the HEDM was conducted. This complete process, from obtaining *parent cubic orientations* to using the CTM to obtain *calculated monoclinic variants* ins elucidated in Figure 5.3.

5.2.6. Linear Elastic Simulations

To compliment the experimental studies described above, linear elastic simulations are carried out at the specimen scale, to study the response of the specimen during tensile loading.

The exact geometry of the specimen was obtained from photography and optical microscopy and used to construct a surface mesh, which was then extruded into a volumetric mesh according to the depth dimension of the specimen. The model was loaded in uniaxial tension to mimic the in situ diffraction experiments, in order to capture the effect of the specimen shape and any asymmetries thereof, due to machining, on the deformation response. For simplicity, the material is assumed to be isotropic and linear elastic, to isolate the effect of asymmetry of the specimen geometry. Figure 5.1(e) shows a face of the specimen with the notch on the left side and the loading boundary conditions imposed. The simulations are run on ABAQUS, using ten-node tetrahedral elements (C3D10 in abaqus notation).

5.3. Results

5.3.1. Deformation at the macroscale

At the specimen scale, DIC is used to track the surface strain on the specimen around the notch, as indicated by the dotted box in Figure 5.1(b). Figure 5.4(a, b) shows the experimental strain contours at peak load, prior to fracture, as obtained by DIC. (a) shows the axial component of the strain along the loading direction while (b) shows the Mises strain calculated from the 2D surface strain tensor. The axial strain peaks at $\approx 3\%$ while the Mises strain, which accounts for the transverse and shear strains peaks at $\approx 5\%$. Both the strain maps show an asymmetry about the notch center line, towards the left side. To complement the DIC strain map of deformation around the notch, the simulated axial and Mises components of the 3D strain tensor at peak load are shown in Figure 5.4(b, d). The simulated maps shows a similar asymmetry about the notch central line. Since this is a linear elastic simulation, the asymmetry arises from the specimen geometry, imperfections and the notch. Therefore, a misalignment between the specimen center, loading line and

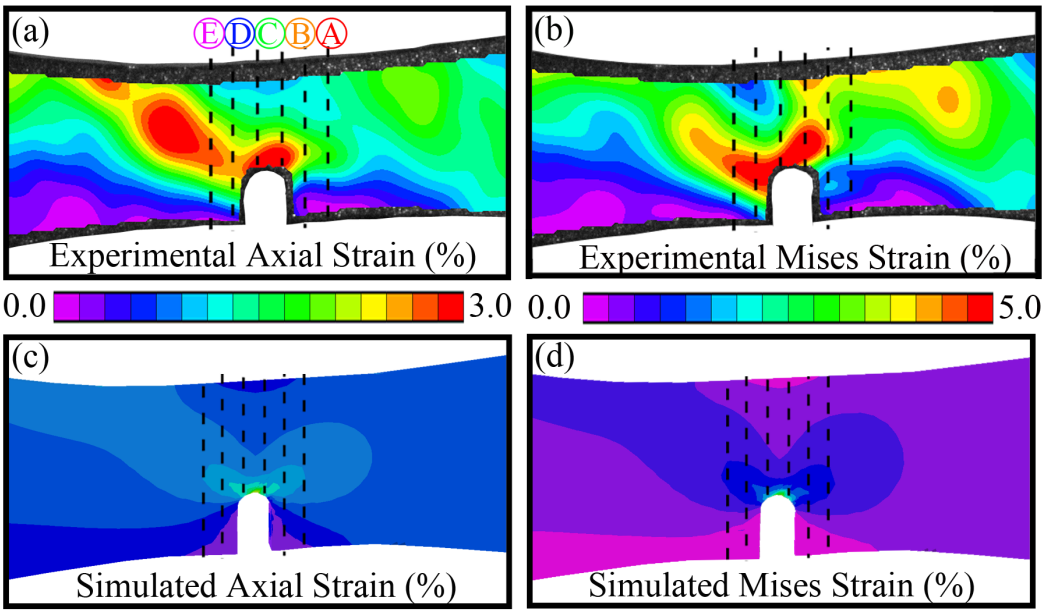

Figure 5.4. Deformation at the specimen scale. Comparison of surface strain maps around the notch in the specimen obtained from (a,b) experiments using Digital Image Correlation and (c,d) simulations. (a, c) show the axial surface strain around the notch, showing an asymmetric band of high strain towards the top left of the notch. The axial strain contour shows a peak strain of $\approx$ 3%. (b, d) show the Mises strain from experiments and simulations. The Mises strain is calculated using the 2D surface strain tensor in (b) and using the 3D volumetric strain tensor in (d). The Mises contour shows a peak strain of $\approx$ 5%, emphasizing the non uniaxial strain field around the notch. The dotted lines are numbered in (a) and represent the diffraction layers Ⓐ - Ⓔ.

notch center can be explained as the most plausible source of deformation asymmetry at the specimen scale.

5.3.2. Deformation at the intermediate microscale

The heterogeneous deformation state experienced by the diffraction layers, both along the loading direction and overall strain state, represented by the Mises strain can be seen in Figure 5.4. At the microscopic length scale, HEDM is used to investigate the micro to mesoscale deformation. The raw diffraction images are used to provide a qualitative picture

of deformation in each of the five diffraction layers, at every loading step ① - ⑥ in the first cycle, as outlined in Figure 5.1(d). Figure 5.5(a) shows individual rings from 2 regions of the overall diffraction pattern for every layer at every loading step. This image is obtained by taking the maximum intensity at every pixel for all 3600 diffraction images taken for a diffraction layer at that load step, through the 360^0 rotation. For simplicity, rings from the same family are considered in both regions.

In general, the horizontal spread in spots is indicative of the orientation spread in the diffracting crystallites whereas the vertical spread comes from the spread in elastic strain. The intensity of spots indicates the volume of diffracting crystallites. The vertical arrows indicate increasing loading steps, from ① to ⑥. The spots inside the orange box correspond to the loading direction and [1 1 1] ring is considered (Figure 5.5(b)). Layers Ⓐ and Ⓑ to the right of the notch show a reduction in horizontal spread of the central peak, with the peaks disappearing at peak load, *indicating a reorientation of grains with their* [1 1 1] *axis parallel to the loading axis.* On the other hand, Layers Ⓒ and Ⓓ show the split central peak coalescing into one central peak, *pointing towards deformation by orientation coalescence.*

The green box lies perpendicular to the loading direction and the $[\bar{1}\,1\,1]$ is considered (Figure 5.5(c)). In Layers Ⓐ and Ⓑ, the peaks move away from each other with increased loading and continue through unloading, *indicating an increasing misalignment of the* $[\bar{1}\,1\,1]$ *axis perpendicular to the loading axis.* Layers Ⓒ and Ⓓ shows an increased coalescing of spots with loading into larger and more intense clusters on loading (from Step ① to ④). *The coalescence of spots points towards orientation coalescence into larger domains, as indicated by the increasing intensity of spots. The increasing size of spots also points towards these coalescing volumes carrying larger elastic (vertical) and inelastic (horizontal) strains*

with loading. In both of these regions, Layer Ⓔ does not show a significant change in the diffraction pattern in {1 1 1} type rings, along and perpendicular to the loading axis.

This qualitative analysis shows a change in the spot pattern in representative rings belonging to the same family, revealing a microstructure that is continuously evolving, both along and perpendicular to the loading direction. Through these two regions, while some layers (Layer Ⓔ) show little to no change, rings in other layers show changes in the spot pattern including (i) coalescing of spots (ii) divergence of spots (iii) narrowing of spots and (iv) disappearance of spots. Such changes are associated with changes in the microstructure, arising from the deformation and the mechanisms (twin nucleation, detwinnning, twin reorientation) associated thereof. This analysis is then expanded, to encompass entire diffraction rings instead of just two directions and to quantify the changes seen through the raw diffraction pattern, to provide a complimentary picture of the deformation.

The *observed monoclinic orientations* obtained from the complete rings during in situ loading are matched with *calculated monoclinic variants* obtained from the high temperature HEDM, as outlined in Section 5.2.5. For every *calculated monoclinic variant* in each layer and at each step, a volume is calculated, based on the intensity of all *observed monoclinic orientations* that are matched with it. The volume percent of every *calculated monoclinic variant* is then defined as the intensity of a variant in a layer at a load step normalized by the sum of intensities of all variants in that layer at that load step. Figure 5.6 shows the evolution of the orientation in each layer in the specimen, plotted on Euler angle figures at every loading and unloading step in the first cycle (① - ⑥). For reference, the orientations in the top row are plotted on an inverse pole figure along the loading axis, for the initial loading step ①). The rows indicate the loads steps at which the diffraction scan is taken

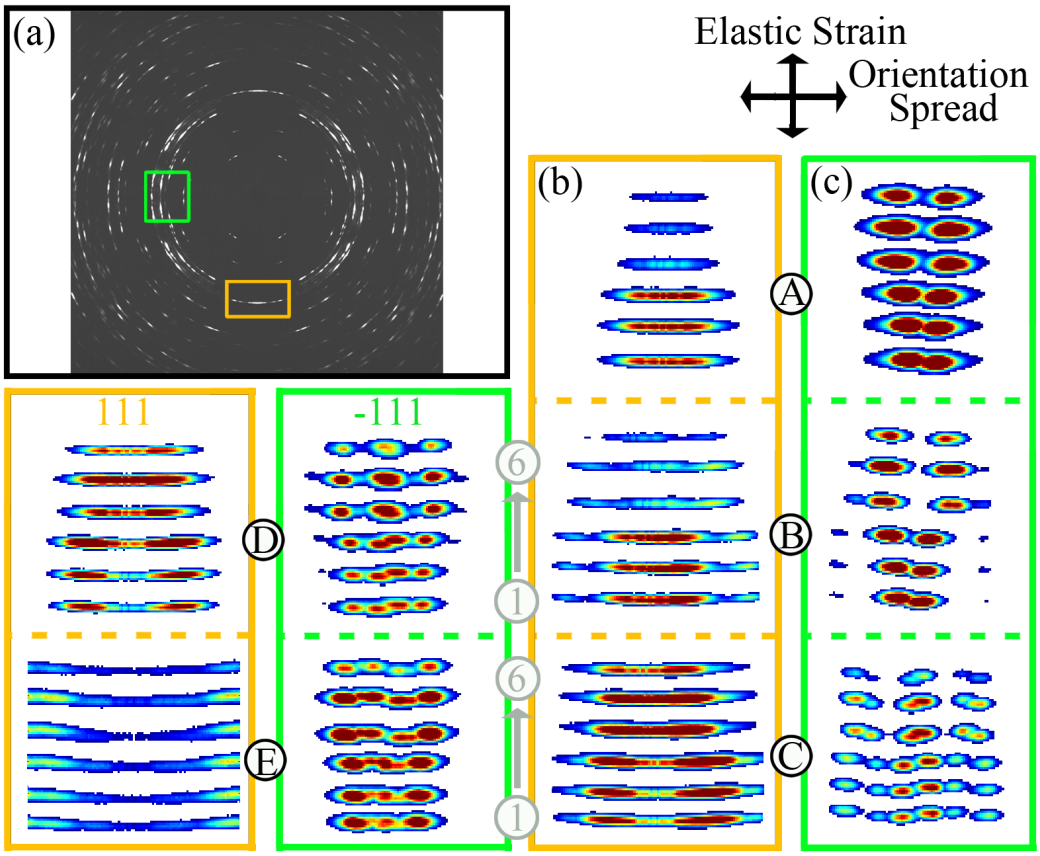

Figure 5.5. Micro-mesoscale deformation in the specimen. (a) shows two sets of diffraction patterns for the load steps 1-7 for all layers, indicated by the colored boxes superimposed on the diffraction pattern. The orange box lies along the loading axis and the orange arrows show the rings considered ([0 0 1], [0 1 1] and [1 1 1]). The green box lies on the axis perpendicular to the loading direction and the arrows indicate the [1 0 0] and [$\bar{1}$ 1 1] rings. Through the layers and across loading and unloading, deformation can be seen in the form of (i) coalescing of spots (ii) splitting of spots and (iii) creation of spots. The diffraction layers are numbered ① - ⑤ while the vertical arrows for each step indicate increasing loading steps in the first cycle, from Ⓐ - Ⓕ, as indicated in Figure 5.1(d).

and the columns represent the layer scanned at that load. The orientations of every variant are colored by the volume percent associated with that variant.

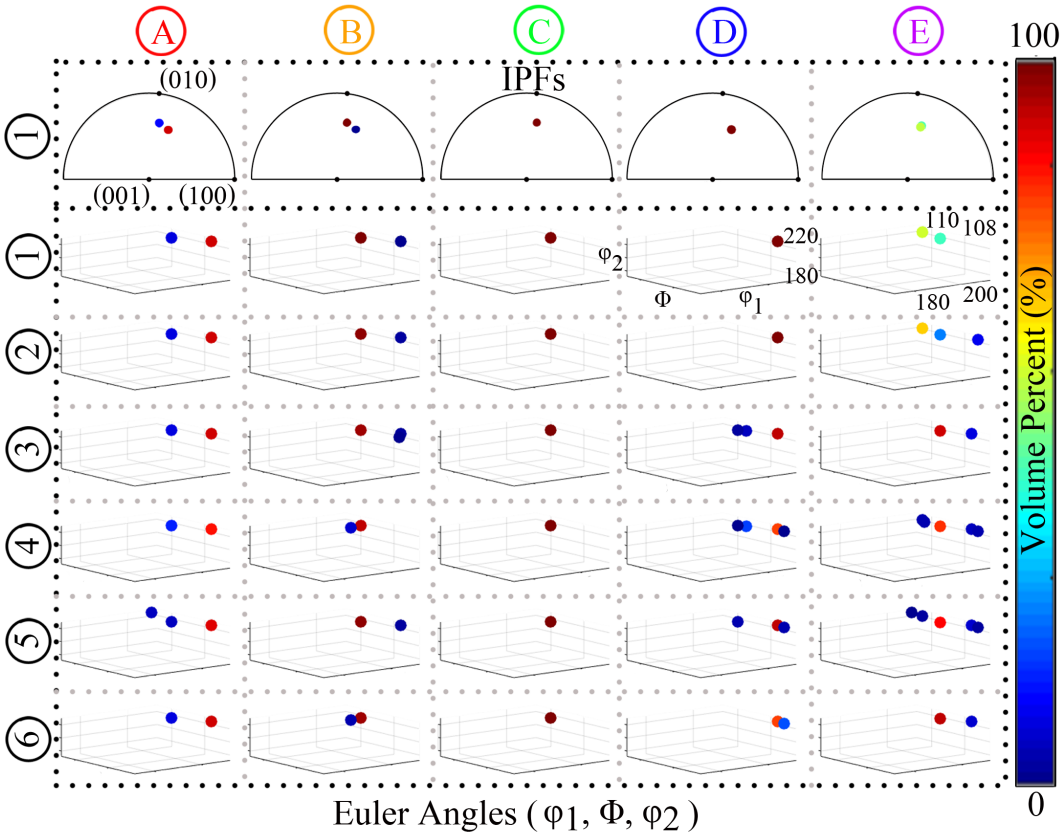

Figure 5.6. Orientations are created for the diffraction layers, based on the *calculated monoclinic variants* and colored according to the volume percent of each variant, as indicated by the colormap on the right. The rows indicate the loads at which the loading was stopped to take diffraction scans during the first cycle ① - ⑥, plotted using the Euler angles of each orientation. As a reference, the orientations in the top row are plotted on an inverse pole figure along the loading axis, for the initial loading step ①. The columns reveal the orientation plots for the five diffraction layers Ⓐ - Ⓔ. The orientations show a continuously evolving microstructure, in terms of number of variants as well as the volume % of every variant. However, these changes are seen to occur within a small sphere of misorientation for every layer.

This analysis reveals that while Layer Ⓒ remains relatively unchanged through loading and unloading, the rest of the layers point towards a continuously evolving microstructure. Layer Ⓐ shows almost no change through loading. There is nucleation of new variant during unloading but it resolves to an orientation map similar to the initial step. Layer Ⓐ also

corresponds to the least deformation, as seen in the DIC strain contour in Figure 5.4(a, b). Layer Ⓑ shows a coalescence of orientations at peak load. In Layers Ⓓ and Ⓔ, the number of variants and volume percent of variants changes during loading and unloading, primarily the nucleation of more variants on loading (from Step ① - ④) and decrease of variants on unloading (Step ⑤ - ⑥). For Layers Ⓑ, Ⓓ and Ⓔ, that show a high strain band in Figure 5.4, the initial and final orientations at Steps ① and ⑥ are different, pointing towards a remnant deformation (strain) upon unloading, as confirmed in the nominal stress-strain curve in Figure 5.1(d). The volume % of each variant at every step for each layer is numerically expanded in Table .1 in Section 5.4.1.1.

Therefore, a quantitative orientation analysis, along with the qualitative analysis of spots on specific portions of rings, provide a picture of a continuously evolving microstructure at the microscale. The raw spots on specific rings show significant changes through loading and unloading for most layers. The orientation analysis of the *calculated monoclinic variants* however reveals very subtle changes in the orientation of the microstructure in each layer, especially in Layer Ⓒ, where the raw spots show a significant change. These findings are reconciled in Section 5.4.

5.3.3. Deformation at the nanoscale

After completion of the first cycle, the specimen experienced brittle fracture during reloading, at a nominal load of $\approx$ 420N. The fracture surface and the equivalent surface Mises strain just before fracture as obtained from DIC are indicated in Figure 5.7(a). The contour indicates that the fracture occurred along a region of high Mises strain. One broken half of the specimen was taken and three sections were lifted from different parts of it, as indicated in Figure 5.7(a, b). These cross sectional areas, perpendicular to the fracture surface are roughly

10 µm x 5 µm and thinned down to electron transparency (<100nm) using FIB milling. The bright field (BF) TEM image in Figure 5.7(c) is from the grip section of the specimen, which does not deform. The selected area diffraction pattern (SADP) of (c) confirms the phase as martensitic NiTi, as shown in the inset. The diffraction pattern is taken along the $[0\,\bar{1}\,2]$ B19 $'$ axis. The structure of martensite is shown in the bright field image in Figure 5.7(d), showing the presence of martensitic laths of about 300 nm thickness and internal nanotwins, with an average width of ≈ 15 nm. Figure 5.7(e,f) correspond to two regions from the fracture surface, as shown in (b), indicated by their respective colored outlines. Both of these areas lie in the central diffraction Layer ©, where the HEDM orientation analysis did not reveal significant changes. (e) is from a region far away from the notch root and shows ≈ 300 nm wide martensitic laths, which are roughly the same dimension as (c). However, the clear and distinct nanotwins seen in (c) are absent and the inset SADP confirms that the martensite phase is still crystalline. (f), which lies at the notch root shows a nanocrystalline/amorphous phase, with the inset SADP pattern confirming it to be martensitic NiTi. There is an absence of a clear lath structure seen in (d) or (e).

5.4. Discussion

5.4.1. Multiscale analyses show a continuously evolving and heterogeneous martensitic microstructure

In the specimen and deformation scheme considered, there are multiple sources of stress concentration, potentially leading to heterogeneity on the deformation field. These include the single edge notch (Figure 1(b)), martensite-martensite interfaces (Figure 6(c)) and brittle inclusions and localized cracking induced thereof (Figure 5.9(b). At the specimen scale, the deformation is dictated by the specimen geometry and boundary conditions during loading,

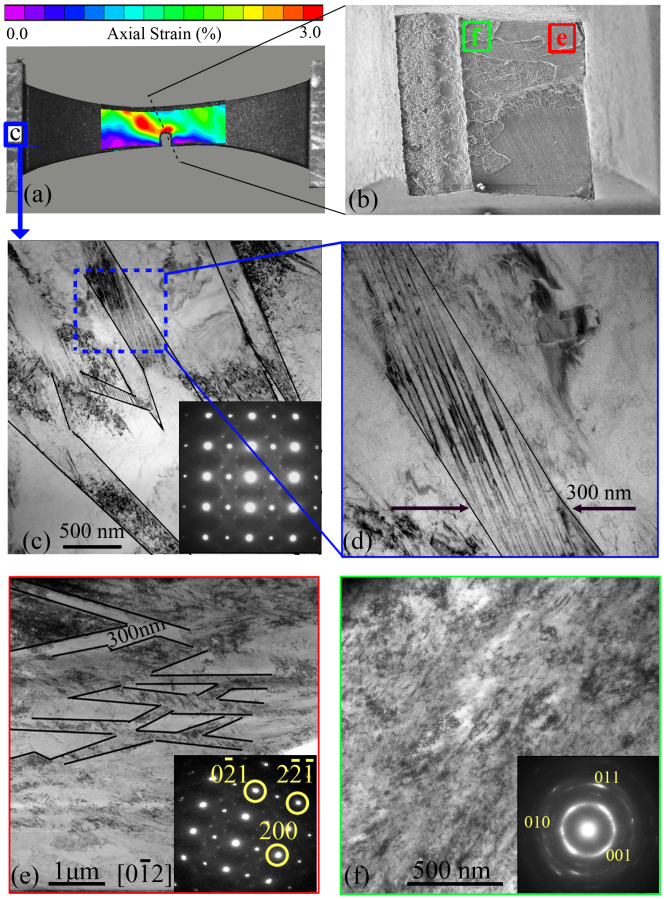

Figure 5.7. TEM on the specimen reveals heterogeneity of deformation at the nanoscale. (a) shows a map of DIC axial strain taken just before fracture, with the dotted line indicating the fracture surface. (b) shows an SEM image of the fracture surface of one half of the specimen. The vertical line towards the left indicates the notch. For (c-e), all TEM foils are perpendicular to the surface in (b). (c) shows a region towards the grip section of the specimen, which undergoes no deformation. (d) shows the dotted blue box in (c), showing martensite laths (inset in (c) shows the SADP pattern) with internal nanotwins. (e) indicates a region far away from the notch root, as indicated by the red box in (b). The TEM micrograph reveals martensite laths and the SADP confirms the retention of crystalline structure of martensite. (f) reveals the region at the notch root with nanocrystalline/amorphous martensite phase (inset shows SADP pattern). In (c-e), loading is in the vertical direction and black lines are used on the raw TEM micrographs to highlight the martensite laths.

confirmed by the match between linear elastic simulations and DIC strain maps in Figure 5.4. At the meso and nanoscale, HEDM and TEM reveal further insights into the heterogeneities and evolution of the martensitic microstructure.

5.4.1.1. HEDM reveals spatial heterogeneity and evolution of martensite microstructure with loading

. Section 5.3.2 reveals the key result from the HEDM analysis, as shown in Figures 5.5 and 5.6, which is a continuously evolving microstructure for every layer at every step. Figure 5.7 (e,f) then confirm that the deformation on the fracture surface, which lies in Layer © is spatially heterogeneous and occurs at a sub-micron length scale, which is lower than the length scale of HEDM. Therefore, the overall orientation picture in Figure 5.6 does not show significant change with loading and unloading, while a qualitative analysis into the rings confirms that the spot pattern changes, indicating an evolving microstructure with loading. For all the other layers, Figure 5.6 shows that there are new variants created or disappearing at various steps during loading and unloading. However, these all occur within a small misorientation degree, therefore pointing towards texture in the material which is largely unchanged. This result is in direct contrast to earlier works on texture evolution with loading in martensitic NiTi. Daymond et. al. [**33**] quantified the increasing texture with increased load in martensitic NiTi, directly underneath a crack under Type I tensile loading while Stebner et. al. [**120**] quantified the texture increase in monoclinic NiTi specimens in uniaxial tension, in the absence of any stress concentrator. The intensification of texture is consistent with the expected high degree of anisotropy in low crystal symmetry phases and also consistent with progression of deformation according to the minimization of energy argument employed in the Crystallographic Theory of Martensite (CTM) [**11**].

In the traditional picture of martenstic NiTi, the changing energy landscape with increased loading results in nucleation of new twins or the less energetically favorable variants that exist in the material 'reorientating' into more favorable variants. As loading increases, all orientations reorient into a single energetically favorable orientation [**53, 81, 119**]. However, the results above show multiple variants present in the specimen even at high loads and strains and a continuously evolving microstructure.

Table 5.1 elucidates this point in a numerical manner. Based on matching *observed monoclinic orientations* to *calculated monoclinic variants* 5.3(c), 1-5 *calculated martensite variants* can be matched to *observed martensite orientations* at every load step. The loading steps from ① to ⑥ are considered, to encompass the complete loading and unloading in the first cycle. With increased loading, there is some local reshuffling of the number and volume percent of these *calculated variants*, within the same layer. For example, Layer Ⓔ begins with two variants at Step Ⓐ of comparable volume. With increased loading, we see a general increase in the number of variants till Step ④, where there are five variants, with one dominant variant. On complete unloading, at Step ⑥, it again ends with two variants, as in the beginning, but with one variant having occupying a significantly larger volume as compared to the second. In contrast, Layer Ⓒ shows the same one variant, throughout the loading and unloading steps. On the other hand, Layer Ⓐ shows little change during the complete loading, from Step ① to ④, but shows a third variant nucleating during unloading at Step ⑤ but again goes back to two variants, at full unload at Step ⑥.

However, there is no overall trend observed, such as predicted by deformation through detwinning/reorientation, where increasingly larger loads lead to fewer variants and finally one dominant variant in terms of volume percent. An important reason for this difference in observed behavior lies in the spatial resolution of characterization techniques used in earlier

works and the scale of crystallites observed. With HEDM able to probe the material in situ at a significantly better spatial resolution as compared to powder X-ray or neutron diffraction, a more refined deformation picture emerges, which was not possible with coarse techniques that average the local deformation picture over large volumes. Another reason has to do with the heterogeneity in deformation, due to presence of multiple sources of stress concentration. In this case, every constraint, in addition to introducing a stress field heterogeneity in its neighborhood, also introduces additional crystallographic constraints on deformation, which are not captured under traditional CTM calculations. Since the stress field and crystallographic constraints are so heterogeneous, the favorable and permissible microstructure is also very heterogeneous and locally determined. Therefore, no one/few orientations are energetically stable at the length scale of the crystallites or even HEDM, as would be expected from a classical picture of defroamtion by martensitic reorientation.

Table 5.1. The number and volume percent of *calculated monoclinic variants*

Load Step	Layer Ⓐ	Layer Ⓑ	Layer Ⓒ	Layer Ⓓ	Layer Ⓔ
Step: ①	1 : 91	1 : 99	1 : 100	1 : 100	1 : 56
0N	2 : 09	2 : 01			2 : 43
Step: ②	1 : 91	1 : 98	1 : 100	1 : 100	1 : 67
100N	2 : 09	2 : 02			2 : 24
					3 : 09
Step: ③	1 : 92	1 : 97	1 : 100	1 : 93	1 : 92
200N	2 : 08	2 : 02		2 : 05	2 : 08
		3 : 01		3 : 02	
Step: ④	1 : 86	1 : 93	1 : 100	1 : 80	1 : 82
350N	2 : 14	2 : 07		2 : 18	2 : 06
				3 : 01	3 : 05
				4 : 01	4 : 04
					5 : 03
Step: ⑤	1 : 90	1 : 98	1 : 100	1 : 94	1 : 86
150N	2 : 05	2 : 02		2 : 03	2 : 08
	3 : 05			3 : 03	3 : 03
					4,5 : 2,1
Step: ⑥	1 : 91	1 : 96	1 : 100	1 : 93	1 : 73
0N	2 : 09	2 : 04		2 : 07	2 : 27

Figure 5.6 reveals changes in the number of variants and variant volume % for all layers at all loading steps in the first cycle (① - ⑥). However, as discussed in Section 5.4, all these changes seem to occur within a small misorientation, such that the impact on the overall texture for every layer is small. Figure 5.8 takes the orientations in Figure 5.6 and plots them into a texture contour, using the mtex library on MATLAB to emphasize this point. As in Figure 5.6, columns represent the diffraction layers while rows represent the loading steps in the first load-unload cycle. For each diffraction layer, the texture maps show little to no change with the load state.

There is no overall trend observed, such as predicted by deformation through detwinning/reorientation, where increasingly larger loads lead to fewer variants and one dominant variant in terms of volume percent. An important reason for this difference in observed behavior lies in the spatial resolution of characterization techniques used in earlier works and the scale of crystallites observed. With HEDM able to probe the material in situ at a significantly better spatial resolution as compared to powder X-ray or neutron diffraction, a more refined deformation picture emerges, which will not be possible with coarse techniques that average over large volumes. This reveals a picture of the microstructure that continuously and heterogeneously evolves with the applied load.

5.4.1.2. TEM reveals spatial heterogeneity in martensitic microstructure linked to different inealstic mechanisms

. Figure 5.7(e) and (f) revealed two starkly different microstructures, pointing towards the modes of deformation being very different at the locations on the fracture surface. The section shown in Figure 5.7(e) is shown to deform primarily via internal detwinning, as evidenced by the retention of the large martensite laths seen in the undeformed material, without the internal nanotwins. In past studies on crack growth in martensite, detwinning is

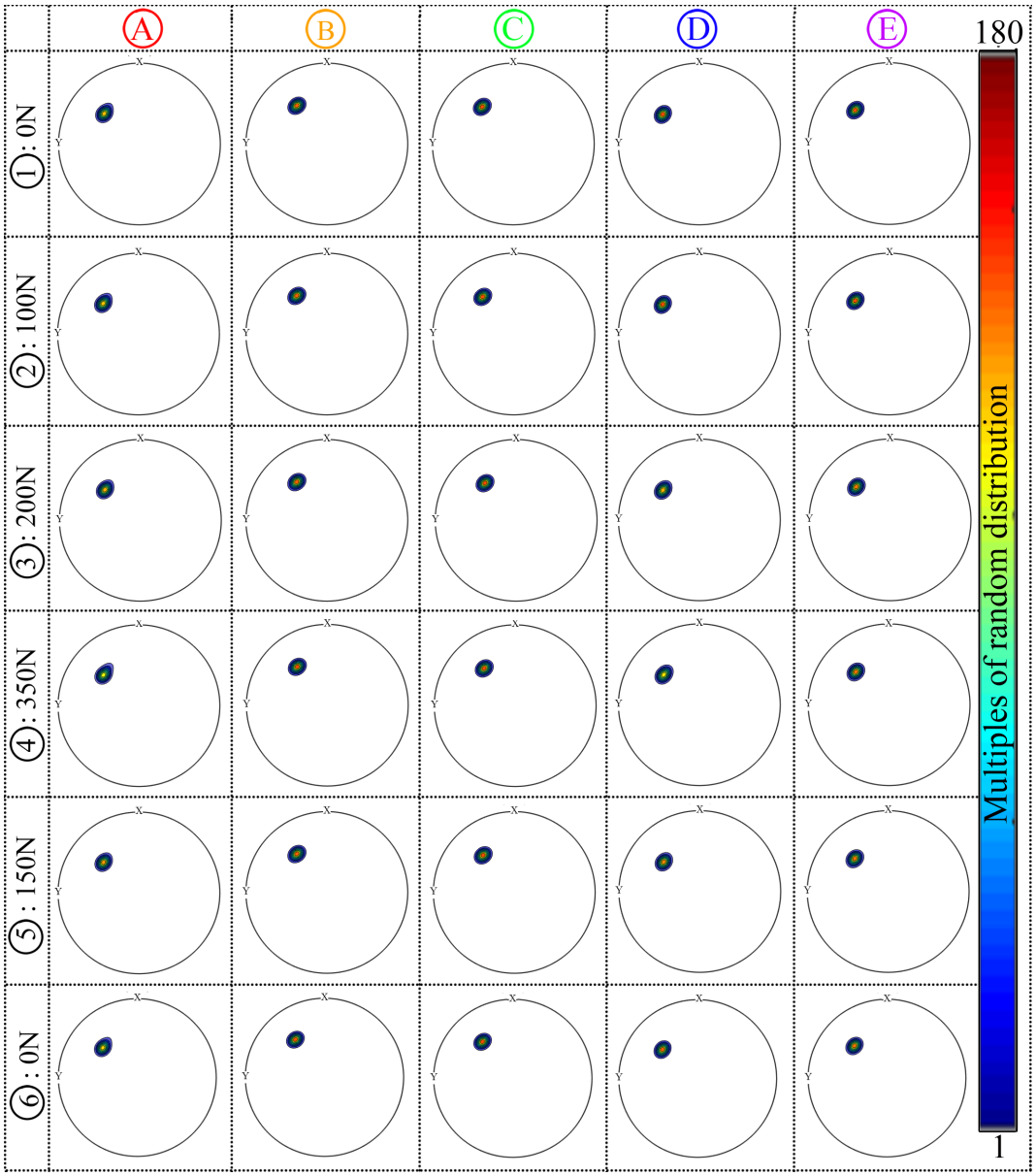

Figure 5.8. Texture maps are created for the diffraction layers around the notch, based on orientations obtained from HEDM, as outlined in Section 5.2.4. The columns reveal the pole figures along the loading direction for the five diffraction layers Ⓐ - Ⓔ whereas the rows indicate loads at which the loading was stopped to take diffraction scans during the first cycle ① - ⑥. The contour coloring is according to multiples of random distribution, as used in standard texture maps. The texture maps reveal very subtle to almost no changes with loading, complementing the subtle changes seen in Figure 5.6.

assumed to be the primary mechanism of deformation in the vicinity of the crack [**33**]. Based on the recovery of strains upon heating after a load-unload cycle, the primary mechanism of deformation near a crack tip is proposed to be detwinning. A crack is reasoned to be growing into a zone of detwinned martensite, analogous to a plastic zone in conventional elastic-plastic metals [**44**]. However, (e) shows the retention of martensite laths on the fracture surface, even after significant loading. This provides an insight into spatially heterogeneous deformation at high loads in martensite, in the presence of multiple stress concentrators. The HEDM analysis in Figure 5.6 and Table 5.1 show that up to very high loads, multiple variants exist under a multi axial stress state, around the notch. The TEM image in Figure 5.7 confirms this through the presence of martensite laths in (e), which would be otherwise absent in a fully detwinned region.

On the other hand, Figure 5.7(f) shows a nanocrystalline/amorphous phase, with diffuse rings superimposed on some diffraction spots, corresponding to martensitic NiTi. Such nanocrystalline and amorphous regions have been observed in martensitic NiTi during deformation by high pressure torsion and in the immediate vicinity of cracks during tensile loading. Waitz et. al. [**136**] showed that a large local shear stress field can induce deformation via amorphization and nanocrystallization in martensitic NiTi. Near the notch, the local stress fields are no longer uniaxial tensile fields. Due to stress concentration around the notch, shear stresses are induced on the fracture surface, at the notch root on the fracture surface, both due to the notch and due to the presence of inclusions. Okamoto et. al.[**90**] observed a transition from a completely amorphous martensitic NiTi phase at the crack tip to a completely crystalline phase far away from the crack tip, through an intermediate nanocrystalline phase. The elevated strain field near the crack was claimed to be the driving force for amorphization. Post mortem SEM imaging shows significant localized cracking to

be present near the notch root, as compared to the region away from it (Figure 5.9). Therefore, a combination of a localized shear shear field and localized cracking at the region near the notch root is likely to induce the deformation via amorphization/nanocrystallization.

In the specimen, postmortem SEM analysis shows the presence of a large number of Ti inclusions near the notch root, which are brittle in nature and pre-cracked (from cooling down of the material to room temperature during material preparation). The SEM images also show the presence of various local cracks in the vicinity of the notch root (Figure 5.9(b), indicated by yellow arrows). In earlier works, post mortem SEM imaging around the inclusions has shown these pre-cracks from the inclusions grow into the matrix, acting as the initiation point of specimen fracture [**106**]. Therefore, in the region of concentrated deformation at the notch root with inclusions, significant cracking is likely to have nucleated before suddenly propagating through the fracture surface resulting in brittle fracture. Therefore, a combination of the presence of significant cracking in the presence of deformation concentration, along with an induced shear stress field in the vicinity of the area on the left, by the notch root, is likely to have induced the nanocrystallization/amorphization of that region. In the absence of a large shear field or significant tensile cracking at the area on the right, away from the notch root, the crystalline phase of martensite is retained, with internal detwinning acting as the primary inelastic deformation mechanism.

Therefore, compared to the traditional picture of detwinning into a single variant as the primary deformation mechanism at high loads in martensite and of cracks primarily growing into a zone of fully detwinned martensite, this mesoscale and nanoscale analysis reveals a rich diversity, in terms of both spatial and load heterogeneity in the deformation of martensite, in the presence of multiple sources if stress concentration.

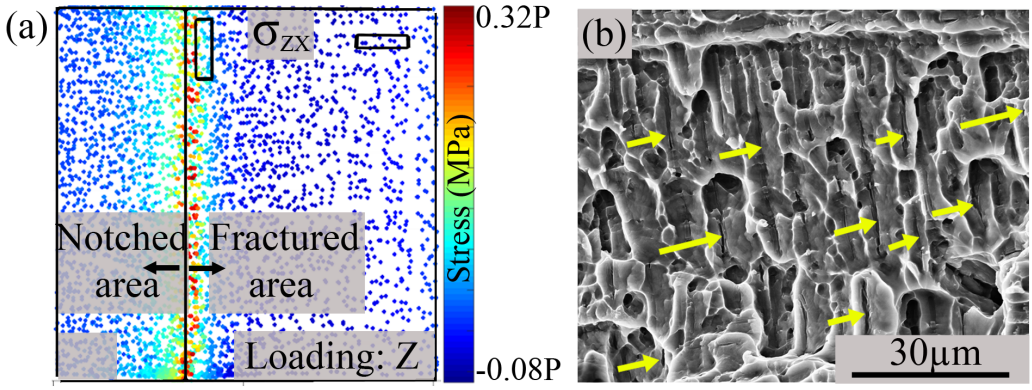

Figure 5.9. Heterogeneity of microstructure and stress state trigger heterogeneous deformation mechanisms on the fracture surface. (a) show a simulation of the shear stress (σ_{ZX}) of the specimen, on the fracture surface indicated in Figure 5.7(a, b). Loading is in the Z direction and the peak axial load is indicated as **P**. The two boxes in (a) indicate the two squares indicated in Figure 5.7(b), from where the TEM sections are examined. The horizontal section on the right corresponds to Figure 5.7(e) while the vertical box on the left corresponds to Figure 5.7(f). (a) shows that a higher shear field develops at the notch root, compared to the box in the region away from the notch. (b) shows an SEM image from the fracture surface, showing a significant extent of localized cracking, another potential source for localized amorphization. Loading is in the X direction.

5.4.2. Low Cyclic Loading also reveals close to homogeneous deformation using HEDM

Similar to the static load case, another specimen with the same dimensions and made from the same material, is taken through a load load-low cycle tensile test and analyzed for evolution of texture through HEDM. *Specimen 2* was taken to a peak load of 200N and complete unloading to 0N. The loading was paused for taking diffraction scans at 0 load, at the end of cycles **1, 2, 3, 8** and **18**. (Figure 5.10(a)) shows the load-strain curve for *Specimen 2*, with the red dots indicating the loads at which diffraction scans are taken. The peak load for cycling is $\approx$ 275N, which is $\approx$ 70% of the fracture load in the specimen. However,

in this case, only one central layer is tracked through HEDM and the texture function is obtained for that layer, which is centered on the single edge notch, with a volume of 1mm x 1mm x 120 µm, as shown in Figure 5.10(b). Loading is done in the vertical direction,in uniaxial tension, like for the specimen. Figures 5.10 (c-g) show the evolution of texture of the diffraction layer with increased cycling, at the end of Cycles 1, 2, 3, 8 and 18 cycles, as shown through pole figures along the loading direction. The lack of a noticeable change in texture points towards the lack of a significant accumulation of deformation with cycling. Since this specimen is comprised of the same material as the specimen, similar sources of constraint are expected to dictate the specimen behavior. Therefore, this lack of significant change in texture of the low crystal symmetry material under multiple and multiscale constraints is displayed again, under cyclic loading conditions.

5.4.3. Implications of varying isotropy across length scales

5.4.4. Implications of varying isotropy across length scales

In the previous sections (5.3.1 - 5.4.1.1), the deformation is seen to be heterogeneous both spatially and with respect to the load state, having an important ramification. In terms of material modeling at the micromechanical scale, the main challenge in NiTi has been effectively capturing the effects of large anisotropy and the plethora of available deformation mechanisms due to the low crystal symmetry. The assumption in martensitic NiTi, of complete reorientation into a single orientation and propagation of cracks in a fully detwinned zone contribute to the extremely high anisotropy of deformation. While phase field models account for inelastic mechanisms such as reorientation and detwinning, they can only be applied to single or oligocrystal materials[**95**]. Conversely, crystal plasticity based models can

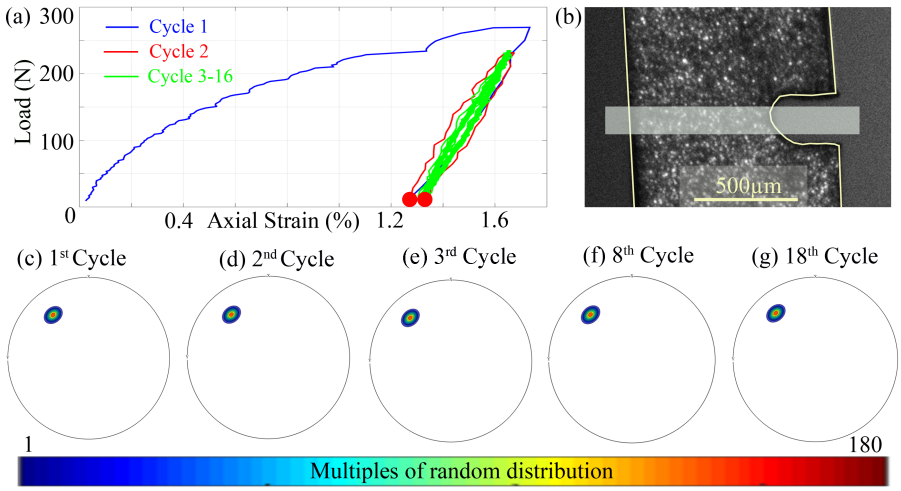

Figure 5.10. Deformation at an intermediate length scale, during low cycle loading of *Specimen 2*. (a) shows the load-strain curve, as obtained from DIC strain maps. The central gauge section (1mm x 1mm) is shown in (b), with a single diffraction layer centered around the notch. Texture maps are created and shown through pole figures along the loading direction, by using the same procedure as in Figure 5.6. The coloring is according to multiples of random distribution, as used in standard texture maps. The texture maps are shown for the central layer about the notch at the end of cycle numbers (c) 1, (d) 2, (e) 3, (f) 8 and (g) 18. The texture shows no significant development over low load cycling.

be used to effectively model polycrystals, but do not account for reorientation mechanisms [**76**]. However, the results from this study show that even at high loads, under a spatially heterogeneous loading scheme and techniques allowing for spatially resolved characterization, the martensite retains its lath structure and exists in multiple variants. Therefore, such materials can now also now be modelled using coarse grain models, where the concerns about the high anisotropy arising from reorientation of martensite are not as critical.

5.5. Conclusions

Two low crystal symmetry (martensitic NiTi) specimens, which have a hierarchical microstructure are studied through tensile deformation, with multiple stress concentrators.

Using traditional techniques, the macroscale and nanoscale deformation picture is studied. An additional intermediate in situ microscale characterization allows to connect between the macro and the nanoscale, whilst providing a unique insight into the progression of martensitic deformation. At various length scales, the deformation picture is seen to be quite distinct.

Macroscale:: At the specimen scale, the asymmetry of the geometry of the specimen is seen to result in deformation hetrogeneity. This results in a non symmetric band of high strain around a single edge notch.

Microscale:: At the microscale, subtle changes in the microstructure are seen with change in the loading. However, the martensitic microstructure at high loads differs from prior suggestions of reorientation into a single variant.

Nanoscale: At the nanoscale, the deformation is again seen to be highly anisotropic, proceeding through different mechanisms. Close to the notch root, amorphization/ nanocrystallization is seen as a dominant mechanism on the fracture surface. Away from the notch root, we see a retention of the martensitic lath structure, which validates the presence of multiple variants at high loads on the fracture surface.

Thus, the hierarchical microstructure of martensite is seen to be spatially heterogeneous and constantly evolving with the load state. This conclusion has important ramifications in terms of using coarse-grain models for microscale simulations, without accounting for the additional complexity due to high anistropy of martensite.

CHAPTER 6

Interactions between Structure and Microstructure Determine Inelastic Mechanisms of Deformation in Low Symmetry Phases

6.1. Introduction

Nickel Titanium (NiTi) is the most common Shape Memory Alloy (SMA), used for a variety of applications, primarily in the aerospace[**132**] and biomedical[**5**] fields. NiTi primarily exists in two phases, a low crystal symmetry (monoclinic) martensite phase and a high crystal symmetry (cubic) phase. The reversible transformation between these two phases gives rise to remarkable properties such as *superelasticity and shape memory effect* in NiTi, contributing to it's widespread use. In terms of characterization of deformation behavior, the cubic phase has received ample attention, owing to relative ease of characterization. The cubic phase transforms through the mechanisms of (i) linear elasticity, (ii) stress induced phase transformation to martensite and (iii) plastic slip, often concurrently. Various experimental and modeling endeavors have attempted to characterize these mechanisms individually as well as interactions between them when they act simultaneously [**95, 94, 108, 71**].

In the low symmetry martensite phase, the deformation behavior during isothermal loading is known to proceed primarily through the mechanisms of (i) linear elasticity, (ii) twin nucleation (iii) detwinning/reorientation [**84**]. Instances of other mechanisms such as amorphization and nanocrystallization have also been studied under certain conditions [**126, 63**]. However, as compared to the body of characterization in the cubic phase, the small size of martensitic crystallites (nm), combined with their high degree of anistoropy due to low crystal

symmetry and simultaneous inelastic deformation mechanisms renders their characterization challenging. Various techniques have been used so far, to circumvent these challenges and tie observed deformation in the martensite phase to the deformation mechanisms listed above. At the nanoscale, TEM has been used as an effective tool to study the crystallography of the martensite phase, in particular evolution of the twinned microstructure of martensite with loading [**134**] and the nanocrystallization and amorphization of certain regions of martensite on loading [**90**]. However, while obtaining the crystallography of deformation on individual crystallites, the big picture of the deformation on the entire material is often lost. Additionally, such techniques are destructive, involve cumbersome sample preparation and often ex situ.

Towards the other end of the spectrum, are bulk techniques. In these, the overall sample deformation is studied in bulk, with lower spatial resolution. The observed deformation is then tied to the inelastic mechanisms. For example, the remnant strain on unloading a martensite phase, is the detwinning strain which can be recovered via heating, through a process known as the *shape memory effect*. So the measurement of a remnant strain on unloading of martensite and subsequent recovery of the strain on heating of the deformed martensite is used to concur the deformation via reorientation [**33**]. Averaging over volumes encompassing several thousands of crystallites, texture maps are also created for the martensite phase. The evolution of the texture function, an statistical aggregate of individual crystallite orientations over a large volume, with loading is then used to tie back to the dominant deformation mechanism. However, such bulk averaging techniques smooth over the many local fluctuations, thus losing information on the spatial heterogeneities of deformation and associated mechanisms. Therefore, there is a paucity in micro to mesoscale

characteriation of martensitic deformation, in terms of connecting between the macro and the nanoscale.

For such length scales, synchrotron X-ray techniques have been successfully combined with modeling and other experimental techniques such as Digital Image Correlation (DIC), for the high symmetry phase and stress induced phase transformation [**109, 97**]. In particular, the effect of a heterogeneous phase (inclusions in the form of carbides and oxides of Ti in a NiTi matrix) was seen to influence the heterogeneity and level of constraint at the microscale and the overall extent of deformation (transformation strain) during stress induced phase transformation of cubic NiTi [**96**]. In recent times, X-ray diffraction is being used to study a deformation picture of the martensite phase which has a good spatial resolution whilst retaining the larger picture of deformation [**21, 20**]. In particular, microLaue diffraction has been used in recent times as a non-destructive technique for characterizing deformation at the sub-micron scale, using synchrotron X-rays [**68, 25**]. This work aims to exploit the superior spatial resolution and in situ capabilities of microLaue diffraction, to provide direct experimental evidence of inelastic mechanisms in the low symmetry martensite phase, without bulk averaging, whilst keeping track of the larger deformation picture of the specimen.

Section 6.2 introduces the material and specimen used in the work, followed by an introduction to the experimental set-up for in situ microLaue diffraction. Section 6.3 then presents the results on two specimens of martensitic NiTi. One experimentally quantifies the effect of Ti inclusions on local deformation heterogeneity while the second specimen focuses on spatial heterogeneity of deformation mechanisms, around a notch. Using diffraction analysis, different inelastic mechanisms are shown to be active explicitly in different areas of the specimen surface, providing a picture of a spatially heterogeneous and continuously

evolving microstructure. Section 6.4 lists the major conclusions as well as significance and broader impact of this work.

6.2. Materials and Methods

6.2.1. Material Preparation

The material used is a NiTi alloy Ni-49.8 at.%-Ti, determined using energy dispersive spectroscopy. The transformation temperatures of the material, using Differential Scanning Calorimetry were found to be $M_f = \approx$ -3^{0}C, $A_s = \approx 31^0$C and $A_f = \approx 45^0$C, meaning the material is completely martensitic below $\approx$ -3^{0}C and completely austenitic above $\approx 45^0$C. It is grown as a single crystal in the cubic austenitic phase at $\approx$ 400C and cooled down to room temperature under stress free conditions, using the modified Brigdman method, as described in [**20**]. During cooling down of the material to room temperature, brittle carbides and oxides of Ti, viz. TiC and TiO_2, henceforth referred to as inclusions, form throughout the material. These have been seen in NiTi SMAs, usually present in networks that span lengths from 1 µm to 100 µm [**106, 100**].

6.2.2. Specimen Preparation

Two dogbone samples were machined from different ingots of this material, with the dimensions indicated in Figure 6.1 (a). These specimens are labelled **Specimen 1** and **Specimen 2**, with a thickness of 0.5mm and 1.43mm respectively. A single edge notch is machined at the center of the gauge section of each specimen using wire electrode discharge machining, with the dimensions of the notch specified in Figure 6.1(b). The surface was then ground and polished up to 1 µm using a diamond-based solution, followed by vibratory polishing with

0.06 µm colloidal silica. Pre-deformation imaging was done on the polished specimen surfaces using an FEI Quanta 600F scanning electron microscope (SEM), to obtain exact notch dimensions and location of inclusions on the surface. The specimens were then dipped in liquid nitrogen for $\approx$ 15 minutes, to get the material below the M_f temperature and completely in the martensite phase. Since the transformation of martensite into austenite on heating starts at the A_s temperature(35^0C), which is above the room temperature, the material is predominantly in martensite phase during room temperature loading experiments.

6.2.3. In situ x-ray Microdiffraction

The in situ fluorescence and microdiffraction scans were done at Beamline 12.3.2 at the Advanced Light Source at the Lawrence Berkeley National Laboratory. A white x-ray beam (6keV-24keV) was focused using Kirkpatrick-Baez (KB) mirrors to a 2 µm x 2 µm beam. A simplified schematic of slits and focusing optics is shown in Figure 6.1(c). The detailed version can be found elsewhere [**123**]. The load frame with the specimen was placed at 45^0 to the forward beam direction. A DECTRIS Pilatus 1M x-ray diffraction area detector was placed at a vertical distance of 150.34mm from the specimen center. The calibration of specimen to detector distance and detector tilts was done using a Si standard. An exposure of 5 seconds was used to record diffraction patterns from a predetermined area (Figure 6.4(b)) on the specimen surface, in a raster mode with a step size of 10 µm x 10 µm. The microdiffraction data was analyzed using the XMAS software suite [**122**].

The uniaxial tensile loading was done at room temperature, using a Deben dual leadscrew load frame under displacement control conditions at 0.2 mm/min. In **Specimen 1**, the scans were taken at a load of 35N. In **Specimen 2**, the loading was stopped at Ⓐ - 15N, Ⓑ - 55N, Ⓒ - 200N and Ⓓ - 250N for diffraction and fluorescence scans, as indicated by the

numbered blue dots in Figure 6.4(a). Due to the presence of inclusions throughout the material, the tensile failure of trial specimens from this material is seen to be sudden and brittle. Therefore, in **Specimen 2**, the loading was done in 5N increments, followed by complete unloading. At the numbered points, The loading was stopped and held at constant displacement for fluorescence and microdiffraction scans. The stress free lattice parameters used for the monoclinic phase of NiTi are $a = 2.89$ Å, $b = 4.11$ Å, $c = 4.65$ Å, $\beta = 96.95^0$ and $\alpha, \gamma = 90.00^0$. The detailed procedure on obtaining these lattice parameters are contained in Chapter 6.2.

Table 6.1. Summary of dimensions and deformation phenomena studied in the two specimens

Specimen Name	Thickness (mm)	μLaue Scans at Load (N)	Deformation Heterogeneity around
Specimen 1	0.50	35	Inclusions
Specimen 2	1.43	15, 55, 200, 250	Notch

6.3. Results and Discussion

6.3.1. Microstructural constraint results in heterogeneity of deformation at the crystallite scale

In **Specimen 1**, an area with a network of Ti inclusions is identified on the SEM, as shown in Figure 6.3(a). The specimen is loaded in the load frame to a load of 35N, where the load first begins to plateau. This region is far away from the notch, so that the stress concentration due to the notch is not felt and the local stress state is similar to the applied stress. The uniaxial loading is in the horizontal direction, as indicated in (a). The area imaged in (a)

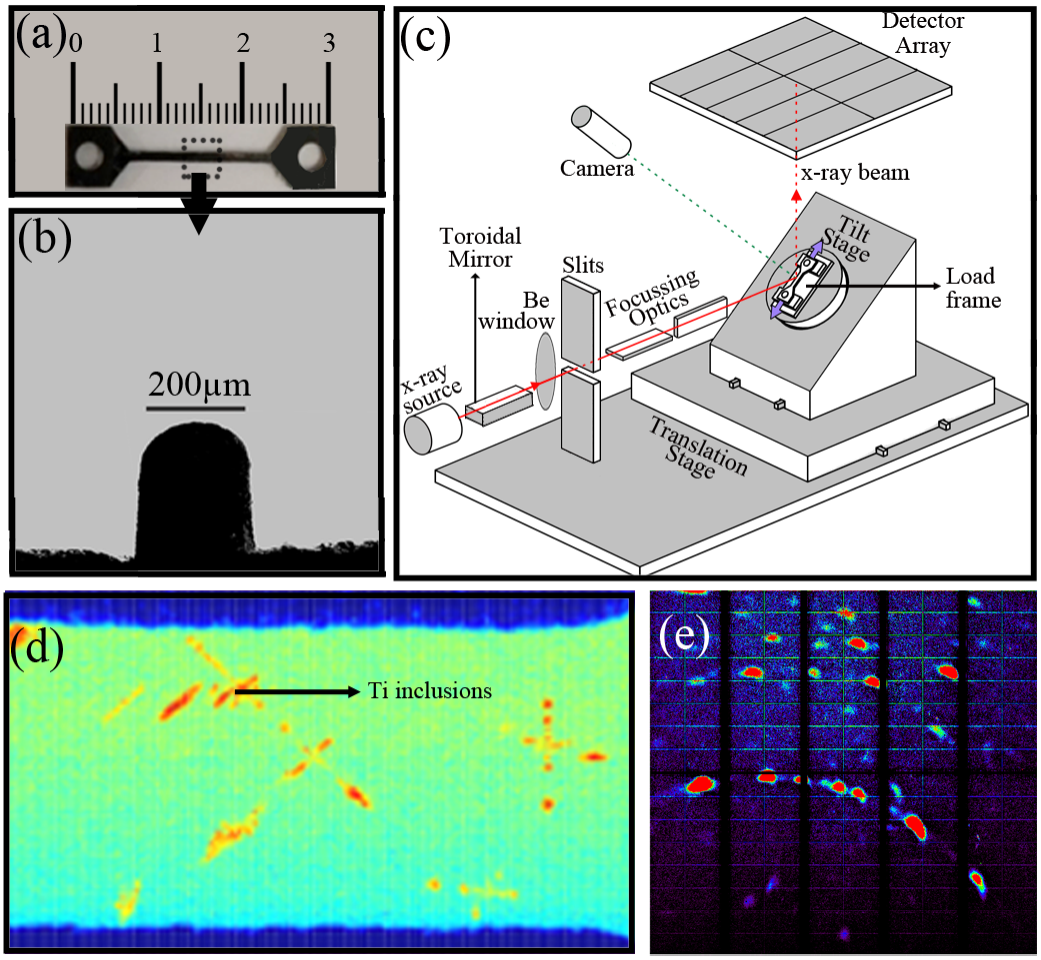

Figure 6.1. (a) shows the dimensions of the planar dogbone used in the tensile experiments. (b) shows a schematic SEM image of the notch tip at the center of the specimen in (a) indicated by the dotted box. (c) shows a schematic of the set-up of the load frame in the microLaue x-ray beam. (d) shows a sample x-ray fluorescence scan taken on Specimen 1. The intensity map shows the counts of Ti, with the red regions indicating Ti rich inclusions (TiC/TiO_2) that are in a matrix of martensitic NiTi. (e) shows a sample diffraction scan taken on a 2 µm x 2 µm area on Specimen 1, with peaks corresponding to the martensite phase of NiTi.

using SEM is located using x-ray fluorescence, as shown in Figure 6.3(b). The colormap indicates number of Ti counts, with the regions in red indicating Ti rich regions (inclusions) on the specimen. Microdiffraction scans are taken on the area indicated in 6.3(b). Three

representative scans corresponding to four distinct regions with respect to the inclusions are considered, marked by boxes (c-e), for which the corresponding microdiffraction patterns are shown in 6.3(c-e). The regions are chosen such that they lie on the same horizontal line. (c) is located far from any inclusion, (d) is located in a region in between two large inclusions while (e) is located close to the inclusion.

In an earlier instance, the effect of deformation heterogeneity around inclusions during stress induced martensitic transformation in NiTi was studied through a combination of 3D X-ray diffraction and modeling [**96**], as shown in Figure 6.2. An idealized simulation of the deformation showed two key results: (a) the region in between two inclusions being shielded from the external stress and (b) the stress concentration at the interface of the inclusions with the matrix, combined with additional crystallographic constraints thereof possibly resulting in the nucleation variants of martensite which are energetically inefficient according to the Crystallographic Theory of Martensite [**11**] and spreading through the specimen. However, the limited spatial resolution of 3DXRD restricted the experimental validation of the conclusions from simulations.

Analysis of the diffraction patterns in (c-e) shed more light on the nature of heterogeneous deformation around the inclusions.

Region (c): shows diffuse and distinct peaks, corresponding to a single orientation of martensitic NiTi. Since it lies in a region far from the inclusions, the local stress state felt by this region is likely to be the same as the external uniaxial stress.

Region (d): shows almost no distinct diffraction peaks. Lying in a region which is shielded in the horizontal direction from the external stress, it is expected that this region experiences no stress and therefore shows very little deformation, resulting in the absence of any clear peaks.

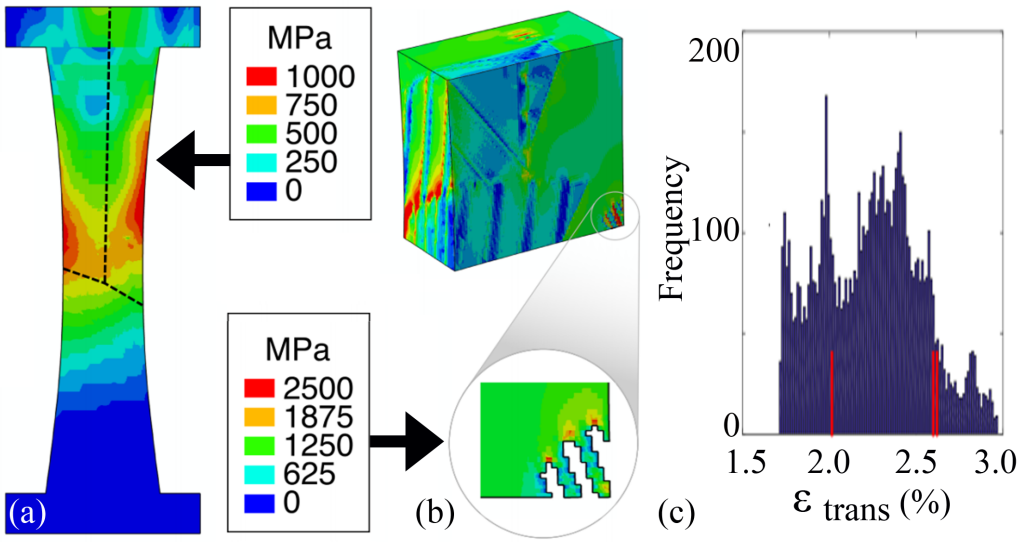

Figure 6.2. (a) Influence of Ti inclusions on deformation of superelastic NiTi, adapted from [**96**]. (a) shows a phase field simulation of the axial stress of the specimen under uniaxial tension. (b) shows a portion from the center of the specimen, where idealized inclusions are modeled (shown in grey in the inset at the bottom). This shows the stress concentration at the tip of the inclusion, which acts as a potential nucleation site for phase transformation. (c) shows the variants of martensite activated in red, as a distribution of all the variants and the transformation strains they produce, as per the Crystallographic Theory of Martensite [**11**]. The efficient variants (that produce the maximum transformation strain) are not activated, possibly due to the additional crystallographic constraints at the interface of the inclusions and the matrix which prevent the nucleation of the most efficient variants.

Region (e): is situated close to an inclusion and shows distinct and intense peaks of martensitic NiTi, with the different colors indicating different orientations of martensite. This lies in a region of stress concentration around the notch, which results in less diffuse and more distinct peaks as compared to (c). The neighboring inclusions also introduce additional crystallographic constraints on the deformation in their vicinity, therefore more number of orientations are identified. Thus the diffraction signature shows a larger extent of deformation, which is also more constrained crystallographically.

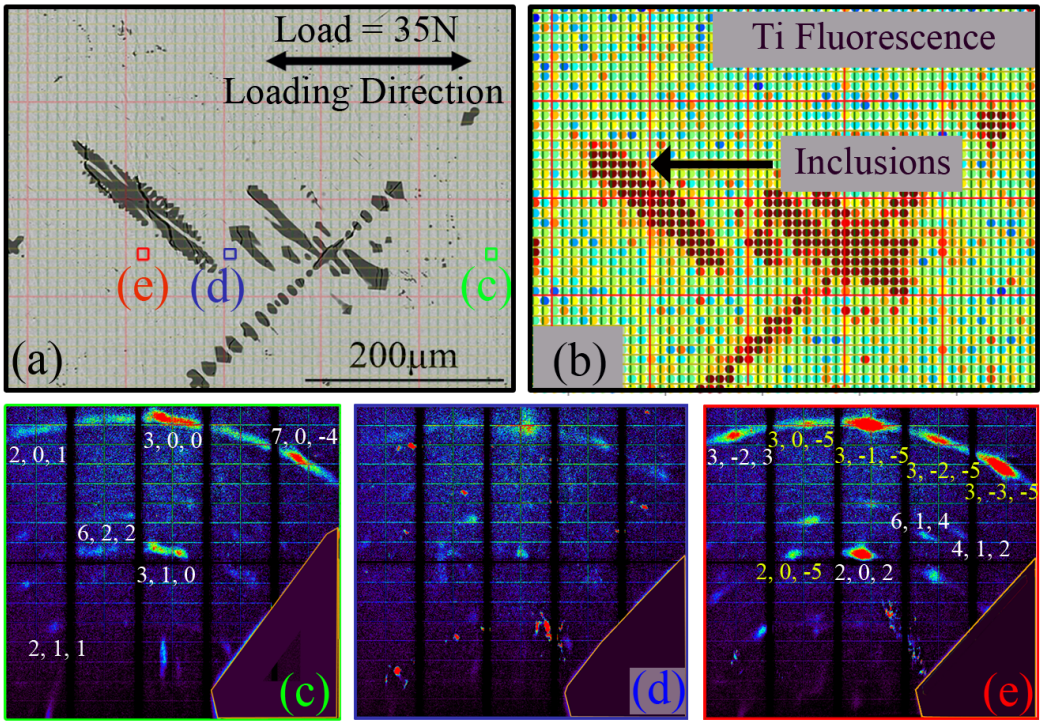

Figure 6.3. (a) shows the preload SEM scan of a region of **Specimen 1** with inclusions (dark regions) in a NiTi martensitic matrix. (b) shows the same area under x-ray fluorescence, similar to Figure 1(d). A grid of the same size as the step size used for the fluorescence is superimposed on (a) and (b). (c-e) represent various microdiffraction scans around the inclusions. (c) represents a region far from any inclusions, showing distinct but weak peaks of martensite, corresponding to one orientation. (d) indicates a region lying directly in between two inclusions in the loading direction, showing no diffraction peaks. (e) shows a region close to the inclusions, where the diffraction pattern shows distinct and intense peaks of martensitic NiTi, with the two colors representing two distinct martensite orientations.

6.3.2. Structural constraint results in heterogeneity of deformation at the specimen scale

In **Specimen 2**, the spatial heterogeneity in tensile deformation around to the notch is analyzed in Figure 6.4, with (a) showing the nominal load-displacement curve. The Ti fluorescence map in Figure 6.4(b) is largely homogeneous, indicating the absence of large

inclusions, which can act as potential sources of deformation heterogeneity in the diffraction area. Panel (c) in Figure 6.4 shows the average intensity from the diffraction pattern for the region indicated by the dotted box in (b) at four load steps: Ⓐ:15N, Ⓑ:55N, Ⓒ:200N and Ⓓ:250N, in the areas shown by the dotted box in (b). The map is colored according to the average intensity of the entire diffraction pattern at every location. The intensity map indicates two regions: a region to the top right of the notch, which corresponds to the region of high intensity, which increases with loading and the rest of the area around the notch. As seen in Figure 6.4(a), scan Ⓑ is taken at a low load, in a region where deformation is primarily elastic. Therefore, to study the inelastic deformation, three of the four loads steps, viz. Ⓐ, Ⓒ and Ⓓ are analyzed in further detail, using two methods which involve analysis of the orientations obtained from the diffraction scans and the raw diffraction patterns. For these analyses, four representative areas are picked (two from each region, as shown by ellipses in Figure 6.4(c)), to illustrate the general trend of deformation while allowing for an in depth analysis.

In the region to the top right of the notch, the two ellipses numbered ① and ② indicate two areas at the edge and center of this high intensity region. The orientation map, created from the most dominant orientation (sizes are proportional to volume percent of the dominant orientation from that area at that load step) shows that the two regions start with their orientations and volumes distinct from each other. Between Ⓐ and Ⓒ, the initial orientations are eliminated while new orientations nucleate. This is accompanied by an increase in the number of monoclinic variants increasing from **two** in Area ① and **one** in Area ② at Step Ⓐ to **three** in both areas at Step Ⓒ. The smaller circles at Step Ⓒ in the figure indicate a lower volume percent of the dominant orientation, showing nucleation and growth of multiple orientations with loading, along with elimination of the initial orientations. After Ⓒ, the

orientation continues to evolve subtly through the load plateau to the load step Ⓓ. The orientations from both the regions switch to the same new orientation, with an increased volume percent compared to Ⓒ. *This evolution of dominant orientation and the increase in volume of the orientations during later stages of loading suggests that reorientation of twins occurred early in loading followed by coarsening of twins.*

On the other hand, the area outside the high intensity region, represented by circles at ③ and ④ in Figure 6.4(c) shows an increasing intensity from Ⓐ - Ⓒ and a decreased intensity post the load plateau beyond Ⓒ. Orientation maps like those for Areas ① and ②, show the dominant orientation to be constantly evolving with load without converging to the same orientation. So, the raw diffraction spots are qualitatively analyzed in Areas ③ and ④.

In Area ③, from Step Ⓐ - Ⓒ, new spots appear along with intensification of existing spots, indicated by the green box. Correspondingly, the number of monoclinic orientations identified increases from **two** to **three**, *which suggests nucleation of new martensite variants as the dominant mechanism.* Further loading beyond Ⓒ plateaus the load and by Step Ⓓ, a number of spots disappear, causing a decrease in intensity (shown by red boxes). *This suggests deformation by detwinning at higher loads.* In Area ④, loading from Step Ⓐ - Ⓒ is accompanied by intensification of existing spots. *The evolution of intensity suggests that whilst no new variants nucleate, a single orientation increases in volume, indicating coalescence of martensite twins by reorientation.* However, further loading from Ⓒ - Ⓓ through the load plateau shows spots that are significantly less diffuse. In microdiffraction, the spread of a spot is tied to the spread of orientation of the diffracting crystallite indicating a decrease in orientation spread from Step Ⓒ - Ⓓ which, along with disappearance of spots, *points towards detwinning and reorientation occurring in these areas at higher loads.*

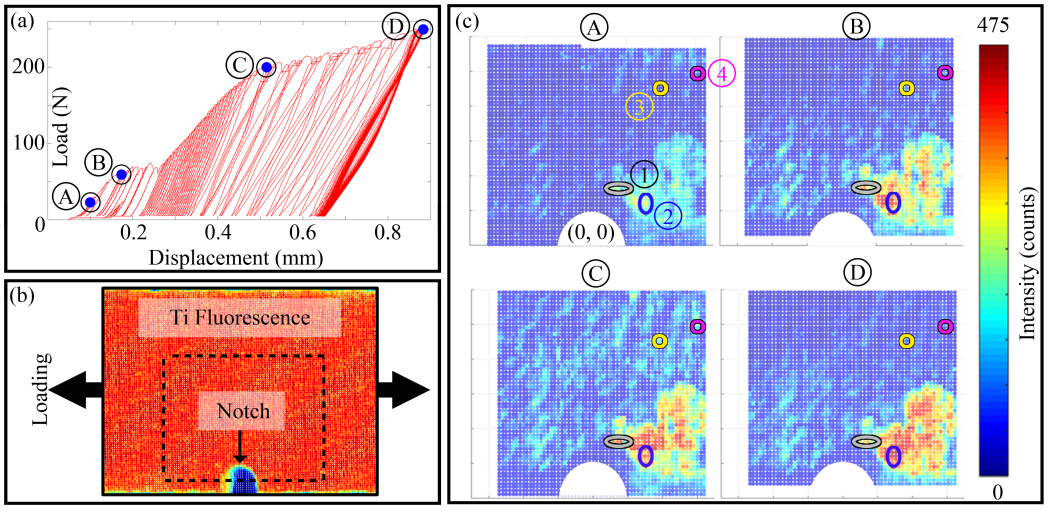

Figure 6.4. (a) shows the load displacement curve for *Specimen 2*. Loading was stopped at Ⓐ:15N, Ⓑ:55N, Ⓒ:200N and Ⓓ:250N. (b) shows the fluorescence scan around the notch (bottom center) and the horizontal arrows indicate the loading direction. (c) shows the spatial distribution of the average diffraction intensity in the area indicated by the dotted box in (b) at four load steps. The intensity map indicates two major regions: a region on the top right of the notch, that intensifies with increasing load and the rest of the map, where the intensity increases from 15N to 200N but decreases at 250N. The four numbered areas, marked by blue, grey, pink and yellow ellipses are analyzed in further detail in Figure 6.5.

A highly heterogeneous progression of deformation is shown around the notch. Regions on one side of the notch show deformation primarily via reorientation and coarsening of twins, with an increasingly larger area coalescing towards the same orientation. Away from the notch, deformation occurs simultaneously via twin nucleation, intensification and de-twinning, seen through the evolution of raw diffraction peaks. Even though the nominal load-displacement shows distinct plateaus, the local deformation picture is heterogeneous and constantly evolving with increased loading, with multiple active inelastic mechanisms.

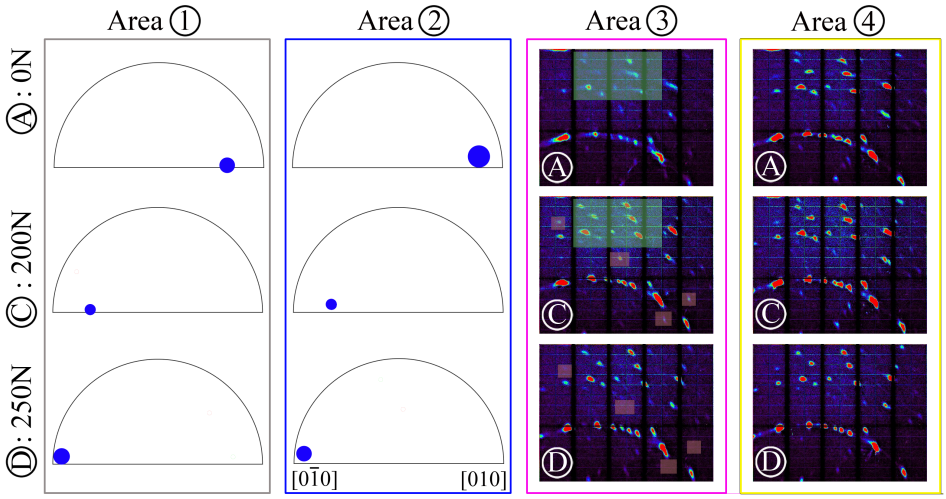

Figure 6.5. Dominant monoclinic orientation for the regions numbered ① and ② near the notch in Figure 6.4(c), at loading steps Ⓐ, Ⓒ and Ⓓ. The sizes are according to the volume percent of all orientations at that region, at that load step. All orientations are plotted on an inverse pole figure along the loading direction. After initial deformation, the orientations converge towards the same value. Areas ③ and ④ are located far from the notch. The panels show the raw diffraction patterns at load steps Ⓐ, Ⓒ and Ⓓ. The boxes in Area ③ are used to highlight changes (appearance and disappearance) of spots with loading.

6.3.3. Framework for analysis of low symmetry phases

Characterization of low crystal symmetry phases, such as martensite in SMAs at the sub-micron to micron scale has been every challenging, using traditional techniques such as EBSD. X-ray microLaue diffraction allows for an in situ analysis at this scale, using both qualitative and quantitative methods. Due to the small scale of crystallites and a large orientation spread, the number of clean and distinct peaks are low, as compared to high symmetry phases. So a strain analysis using shapes of Laue peaks to elucidate deformation mechanisms is not feasible [**50**]. However, a qualitative analysis of the peak patterns, combined with a tracking of the nominal load-displacement state, allows to link local changes in the microstructure to the known inelastic deformation mechanisms such as twin nucleation

and reorientation. *Through this, spatially resolved martensitic reorientation is seen for the first time at the mesoscale and tied to the nominal loading curve.* This work validates a heterogeneous and continuously evolving picture of martensitic microstructure under a heterogeneous local stress state, such as near a notch, as seen in [**102**], where multiple inelastic mechanisms act simultaneously, even at very high loads, resulting in a microstructure that is constantly evolving with the load. Therefore, this characterization technique provides a unique non-destructive and in situ way of connecting the macroscale to the nanoscale.

6.4. Conclusions

Using non-destructive, in situ X-ray micorLaue diffraction, the inelastic deformation of a low symmetry phase under struatural and microstructural constraint was examined at the micro to mesoscale revealing:

(1) **Deformation under microstructural constraint**: Deformation analysis in the vicinity of a heterogeneous phase (inclusions of Ti) reveals:
   (a) The stress concentration at the interface of the inclusions with the matrix results in deformation nucleating in this region
   (b) Additional crystallographic constraints at the interface results in a higher degree of constraint on the deformation, seen in the form of multiple variants of martensite that exist near the interface.

(2) **Deformation under structural constraint**: Deformation around a notch reveals a spatially heterogeneous microstructure, that evolves continuously with loading.
   (a) In a region of high deformation on one side of the notch, reorientation and coalescence of martensite twins is seen as the primary deformation mechanism.

(b) In regions outside the reorientation region, there is twin nucleation and detwinning, up to peak load, even while the reorientation zone continues to grow.

(c) The nominal load-displacement curve shows distinct plateaus but the spatially resolved deformation picture is heterogeneous and constantly evolving with loading, occurring through multiple inleastic mechanisms.

This work provides the first mesoscale in situ, experimental evidence of reorientation and coalescing of variants in martensite. Finally, this work also provides an example of analysis of phases where the standard methods used for strain analysis are not effective and raw experimental data can be connected directly to inelastic mechanisms.

CHAPTER 7

Conclusions and Future Work

In the preceding chapters, a detailed methodology towards a more complete picture of characterization in multiphase and multiscale materials was presented. Through different chapters, the research questions addressed in the beginning in Section 1.3 were addressed, namely:

(1) What is an effective methodology for characterizing materials where the deformation mechanisms and the deformation heterogeneities induced thereof act at different length scales.
(2) If multiple sources of constraint act simultaneously, how can the effect of each be individually understood in the overall deformation picture.
(3) If different deformation mechanisms act at different length scales, how can they be effectively characterized and understood.

. The common thread running through the thesis was the presence of multiscale constraints and the interactions in between constraints, in particular those arising from structural considerations and those from microstructural considerations.

(1) Chapter 2 showed the effect of relative size between structure and microstructure determining the phase transformation response of cubic NiTi. Through DIC, EBSD, TEM and phenomenological modeling, the effect of competition between nanoprecipitates and microholes on dominating the deformation response was elucidated.

(2) Capter 3 expanded on Chapter 2 and showed the interaction between microholes and grain crystallography influencing fracture propagation. Through SEM, EBSD and micromechanical modeling, certain guidelines for local orientation engineering were outlined, for potential improvement of fatigue response of SMA components, made feasible by advances in additive manufacturing.

(3) Chapter 4 examines the role of structure and microstructure in determining the extent of inelastic deformation suppression at the mesocale to the nanoscale. Through micromechanical modeling, the size of grains relative to the size of the specimen is systematically varied, elucidating the factors suppressing transformation when grain size approaches the specimen size.

(4) Chapter 5 studied the simultaneous effect of multiple constraints across multiple length scales on deformation reponse of the low symmetry martensite phase. Through a combination of DIC, HEDM, TEM and macroscale modeling, a spatially heterogeneous and constantly evolving picture of the martensitic microstructure was revealed.

(5) Chapter 6 built on the findings of Chapter 5 and showed the spatial heterogeneity of deformation in martensitic NiTi as arising from differing dominant inelastic modes of deformation. Using microLaue diffraction, experimental evidence is shown for the mechanism of reorientation and the deformation heterogeneity around a heterogeneous phase.

The understanding of complex interactions between structure and microstructure also help in advancing the flexibility of parts and components, specifically those made by additive manufacturing. The presence of complex microstructural and structural features in metal additive components is well documented, as a result of rapid cooling and heating rates.

The next push in additive manufacturing being towards the design of tailor-made materials to desired properties. Towards this, the detailed characterization of structure-microstructure interactions such as grain morphologies with the pore structure and understanding of associated deformation mechanisms, that give rise to large residual strains which hugely affect properties and performance assumes paramount importance.

Finally, Chapters 5 and 6 also provide a framework on the analysis of low crystal symmetry phases and unclean materials, using non destructive techniques at the mesoscale, to bridge the macro and the nanoscale. Through this methodology, raw experimental data can be linked directly to known deformation mechanisms, in a way that maintains a good spatial resolution without compromising on the overall deformation picture at the specimen scale. In the future, these techniques can be further exploited to unlock more science on such low symmetry phases that have seemed challenging up to now. While the growth rate and crystallography of cracks in high symmetry phases is well understood, a similar work on low symmetry phases does not exist. Using sophisticated in situ techniques such as HRTEM and microLaue diffraction, combined with modeling down to the atomistic scale can help uncover these mechanisms.

References

[1] Ahadi, A., and Sun, Q. Grain size dependence of fracture toughness and crack-growth resistance of superelastic NiTi. *Scripta Materialia 113* (Mar. 2016), 171–175.

[2] Ahluwalia, R., Quek, S. S., and Wu, D. T. Simulation of grain size effects in nanocrystalline shape memory alloys. *Journal of Applied Physics 117*, 24 (June 2015), 244305.

[3] ASTM. ASTM E8 / E8m-15a, Standard Test Methods for Tension Testing of Metallic Materials, 2015.

[4] Baer, E., Hiltner, A., and Keith, H. Hierarchical structure in polymeric materials. *Science 235*, 4792 (1987), 1015–1022.

[5] Bansiddhi, A., Sargeant, T., Stupp, S., and Dunand, D. Porous niti for bone implants: A review. *Acta Biomaterialia 4*, 4 (2008), 773 – 782.

[6] Bartel, T., and Hackl, K. A micromechanical model for martensitic phase-transformations in shape-memory alloys based on energy-relaxation. *Zamm-Zeitschrift Fur Angewandte Mathematik Und Mechanik 89* (Oct. 2009), 792–809. 10 bibtex: Bartel2009.

[7] Baxevanis, T., and Lagoudas, D. C. Fracture mechanics of shape memory alloys: review and perspectives. *International Journal of Fracture 191*, 1-2 (Feb. 2015), 191–213.

[8] Bekker, A., and Brinson, L. C. Temperature-induced phase transformation in a shape memory alloy : Phase diagram based kinetics approach. *Journal of the Mechanics and Physics of Solids 45* (1997), 949–988.

[9] Bernier, J. V., Barton, N. R., Lienert, U., and Miller, M. P. Far-field high-energy diffraction microscopy: a tool for intergranular orientation and strain analysis. *The Journal of Strain Analysis for Engineering Design* (July 2011), 0309324711405761.

[10] Bewerse, C., Gall, K. R., McFarland, G. J., Zhu, P., and Brinson, L. C. Local and global strains and strain ratios in shape memory alloys using digital image correlation. *Materials Science and Engineering: A 568* (Apr. 2013), 134–142.

[11] Bhattacharya, K. *Microstructure of Martensite: Why it forms and how it gives rise to the shape-memory effect*. Oxford University Press, 2003.

[12] Bhattacharya, K., and Kohn, R. V. Symmetry, texture and the recoverable strain of shape-memory polycrystals. *Acta Materialia 44* (Feb. 1996), 529–542. 2 bibtex: Bhattacharya1996.

[13] BIEWENER, A. A. Bone and its functions. *Science 227*, 4687 (1985), 629–630.

[14] Bourke, M. A. M., and Dunand, D. C. Phase fraction, texture and strain evolution in superelastic NiTi and NiTi-TiC composites investigated by neutron diffraction. *Acta Materialia 47* (1999), 3353–3366.

[15] Bourke, M. A. M., Vaidyanathan, R., and Dunand, D. C. Neutron diffraction measurement of stress-induced transformation in superelastic NiTi. *Applied Physics Letters 69* (Oct. 1996), 2477–2479.

[16] Boyd, J. G., and Lagoudas, D. C. Constitutive model for simultaneous transformation and reorientation in shape memory materials. *American Society of Mechanical Engineers, Applied Mechanics Division, AMD 189* (1994), 159–172.

[17] Bram, M., Köhl, M., Buchkremer, H. P., and Stöver, D. Mechanical properties of highly porous niti alloys. *Journal of Materials Engineering and Performance 20*, 4 (Jul 2011), 522–528.

[18] Brinson, L. C. One-dimensional constitutive behavior of shape memory alloys: Thermomechanical derivation with non-constant material functions and redefined martensite internal variable. *Journal of Intelligent Material Systems and Structures 4* (1993), 229–242.

[19] Brinson, L. C., Schmidt, I., and Lammering, R. Stress-induced transformation behavior of a polycrystalline NiTi shape memory alloy: micro and macromechanical investigations via in situ optical microscopy. *Journal of the Mechanics and Physics of Solids 52* (July 2004), 1549–1571. 7 bibtex: Brinson2004.

[20] Bucsek, A. N., Dale, D., Ko, J. Y. P., Chumlyakov, Y. I., and Stebner, A. P. Measuring stress-induced martensite microstructures using far-field high-energy diffraction microscopy. *Acta Crystallographica: Section A* (In Review).

[21] Bucsek, A. N., Pagan, D., Casalena, L., Chumlyakov, Y. I., Mills, M. J., and Stebner, A. P. Ferroelastic twin rearrangement in shape memory alloys elucidated with 3d x-ray microscopy. *Journal of the Mechanics and Physics of Solids* (In Review).

[22] Cai, S., Schaffer, J. E., Yu, C., Daymond, M. R., and Ren, Y. Evolution of intergranular stresses in a martensitic and an austenitic niti wire during loading–unloading tensile deformation. *Metallurgical and Materials Transactions A 46*, 6 (2015), 2476–2490.

[23] Carroll, J. D., Abuzaid, W. Z., Lambros, J., and Sehitoglu, H. On the interactions between strain accumulation, microstructure, and fatigue crack behavior. *International Journal of Fracture 180*, 2 (Apr 2013), 223–241.

[24] Chemisky, Y., Duval, A., Patoor, E., and Ben Zineb, T. Constitutive model for shape memory alloys including phase transformation, martensitic reorientation and twins accommodation. *Mechanics of Materials 43*, 7 (July 2011), 361–376. WOS:000292677500002 bibtex: Chemisky2011.

[25] Chen, X., Tamura, N., MacDowell, A., and James, R. D. In-situ characterization of highly reversible phase transformation by synchrotron X-ray Laue microdiffraction. *Applied Physics Letters 108*, 21 (May 2016), 211902.

[26] Cisse, C., Zaki, W., and Ben Zineb, T. A review of constitutive models and modeling techniques for shape memory alloys. *International Journal of Plasticity 76* (Jan. 2016), 244–284.

[27] Collins, P., Brice, D., Samimi, P., Ghamarian, I., and Fraser, H. Microstructural control of additively manufactured metallic materials. *Annual Review of Materials Research 46*, 1 (2016), 63–91.

[28] Creuziger, A., Bartol, L. J., Gall, K., and Crone, W. C. Fracture in single crystal NiTi. *Journal of the Mechanics and Physics of Solids 56*, 9 (Sept. 2008), 2896–2905.

[29] Dadbakhsh, S., Speirs, M., Van Humbeeck, J., and Kruth, J.-P. Laser additive manufacturing of bulk and porous shape-memory niti alloys: From processes to potential biomedical applications. *MRS Bulletin 41*, 10 (2016), 765774.

[30] Daly, S., Miller, A., Ravichandran, G., and Bhattacharya, K. An experimental investigation of crack initiation in thin sheets of nitinol. *Acta Materialia 55*, 18 (Oct. 2007), 6322–6330.

[31] Daly, S., Ravichandran, G., and Bhattacharya, K. Stress-induced martensitic phase transformation in thin sheets of Nitinol. *Acta Materialia 55* (June 2007), 3593–3600.

[32] Daly, S., Rittel, D., Bhattacharya, K., and Ravichandran, G. Large deformation of nitinol under shear dominant loading. *Experimental Mechanics 49*, 2 (Apr 2009), 225–233.

[33] Daymond, M. R., Young, M. L., Almer, J. D., and Dunand, D. C. Strain and texture evolution during mechanical loading of a crack tip in martensitic shape-memory NiTi. *Acta Materialia 55*, 11 (June 2007), 3929–3942.

[34] Dehoff, R. R., Kirka, M. M., Sames, W. J., Bilheux, H., Tremsin, A. S., Lowe, L. E., and Babu, S. S. Site specific control of crystallographic grain orientation through electron beam additive manufacturing. *Materials Science and Technology 31*, 8 (2015), 931–938.

[35] Eggeler, G., Hornbogen, E., Yawny, A., Heckmann, A., and Wagner, M. Structural and functional fatigue of NiTi shape memory alloys. *Materials Science and Engineering: A 378*, 12 (July 2004), 24–33. bibtex: Eggeler2004.

[36] Elahinia, M., Moghaddam, N. S., Andani, M. T., Amerinatanzi, A., Bimber, B. A., and Hamilton, R. F. Fabrication of niti through additive manufacturing: A review. *Progress in Materials Science 83*, Supplement C (2016), 630 – 663.

[37] Entemeyer, D., Patoor, E., Eberhardt, A., and Berveiller, M. Micromechanical modelling of the superthermoelastic behavior of materials undergoing thermoelastic phase transition. *Journal de Physique IV 5* (1995), 233–238.

[38] Frick, C., Orso, S., and Arzt, E. Loss of pseudoelasticity in nickeltitanium submicron compression pillars. *Acta Materialia 55*, 11 (2007), 3845 – 3855.

[39] Frotscher, M., Neuking, K., Bckmann, R., Wolff, K. D., and Eggeler, G. In situ scanning electron microscopic study of structural fatigue of struts, the characteristic elementary building units of medical stents. *Materials Science and Engineering: A 481482* (May 2008), 160–165.

[40] Gall, K., and Sehitoglu, H. The role of texture in tensioncompression asymmetry in polycrystalline NiTi. *International Journal of Plasticity 15*, 1 (Mar. 1999), 69–92.

[41] Gall, K., Yang, N., Sehitoglu, H., and Chumlyakov, Y. I. Fracture of precipitated NiTi shape memory alloys. *International Journal of Fracture 109*, 2 (May 2001), 189–207.

[42] Gao, W., Yi, X., Sun, B., Meng, X., Cai, W., and Zhao, L. Microstructural evolution of martensite during deformation in zr50cu50 shape memory alloy. *Acta Materialia 132* (2017), 405 – 415.

[43] Gao, X., Stebner, A., Brown, D. W., and Brinson, L. C. Neutron diffraction studies and multivariant simulations of shape memory alloys: Concurrent verification of texture development and mechanical response predictions. *Acta Materialia 59* (Sept. 2011), 5924–5937. 15 bibtex: Gao2011.

[44] Gollerthan, S., Young, M. L., Baruj, A., Frenzel, J., Schmahl, W. W., and Eggeler, G. Fracture mechanics and microstructure in NiTi shape memory alloys. *Acta Materialia 57*, 4 (Feb. 2009), 1015–1025.

[45] Gürsoy, D., De Carlo, F., Xiao, X., and Jacobsen, C. TomoPy: a framework for the analysis of synchrotron tomographic data. *Journal of Synchrotron Radiation 21*, 5 (Sep 2014), 1188–1193.

[46] Hane, K. F., and Shield, T. W. Symmetry and microstructure in martensites. *Philosophical Magazine A 78*, 6 (Dec. 1998), 1215–1252. bibtex: Hane1998.

[47] Hane, K. F., and Shield, T. W. Microstructure in the cubic to monoclinic transition in titaniumnickel shape memory alloys. *Acta materialia 47*, 9 (1999), 2603–2617. bibtex: Hane1999.

[48] Huang, W. On the selection of shape memory alloys for actuators. *Materials and Design 23*, 1 (2002), 11 – 19.

[49] Ice, G. E., Larson, B. C., Yang, W., Budai, J. D., Tischler, J. Z., Pang, J. W. L., Barabash, R. I., and Liu, W. Polychromatic X-ray microdiffraction studies of mesoscale structure and dynamics. *Journal of Synchrotron Radiation 12*, 2 (Feb. 2005), 155–162. bibtex: Ice2005.

[50] Ice, G. E., and Pang, J. W. Tutorial on x-ray microlaue diffraction. *Materials Characterization 60*, 11 (2009), 1191 – 1201.

[51] Jape, S., Baxevanis, T., and Lagoudas, D. C. On the fracture toughness and stable crack growth in shape memory alloy actuators in the presence of transformation-induced plasticity. *International Journal of Fracture* (Sep 2017).

[52] Javid, F., Liu, J., Rafsanjani, A., Schaenzer, M., Pham, M. Q., Backman, D., Yandt, S., Innes, M. C., Booth-Morrison, C., Gerendas, M., Scarinci, T., Shanian, A., and Bertoldi, K. On the design of porous structures with enhanced fatigue life. *Extreme Mechanics Letters 16*, Supplement C (2017), 13 – 17.

[53] Jones, N. G., and Dye, D. Martensite evolution in a NiTi shape memory alloy when thermal cycling under an applied load. *Intermetallics 19* (Oct. 2011), 1348–1358. 10 bibtex: Jones2011.

[54] Kabirifar, P., Chu, K., Ren, F., and Sun, Q. Effects of grain size on compressive behavior of niti polycrystalline superelastic macro- and micropillars. *Materials Letters 214* (2018), 53 – 55.

[55] Kammers, A. D., and Daly, S. Digital image correlation under scanning electron microscopy: Methodology and validation. *Experimental Mechanics 53*, 9 (Nov 2013), 1743–1761.

[56] Kelly, A., Stebner, A. P., and Bhattacharya, K. A micromechanics-inspired constitutive model for shape-memory alloys that accounts for initiation and saturation of phase transformation. *Journal of the Mechanics and Physics of Solids* (2016).

[57] Khalil-Allafi, J., Dlouhy, A., and Eggeler, G. Ni4ti3-precipitation during aging of NiTi shape memory alloys and its influence on martensitic phase transformations. *Acta Materialia 50*, 17 (Oct. 2002), 4255–4274.

[58] Kim, K., and Daly, S. Martensite Strain Memory in the Shape Memory Alloy Nickel-Titanium Under Mechanical Cycling. *Experimental Mechanics 51* (Apr. 2011), 641–652.

[59] Kimiecik, M., Jones, J. W., and Daly, S. The effect of microstructure on stress-induced martensitic transformation under cyclic loading in the SMA Nickel-Titanium. *Journal of the Mechanics and Physics of Solids 89* (Apr. 2016), 16–30.

[60] Kimiecik, M., Wayne Jones, J., and Daly, S. Grain orientation dependence of phase transformation in the shape memory alloy NickelTitanium. *Acta Materialia 94* (Aug. 2015), 214–223.

[61] Kobryn, P. A., and Semiatin, S. L. The laser additive manufacture of ti-6al-4v. *JOM 53*, 9 (Sep 2001), 40–42.

[62] Kohl, M., Bram, M., Moser, A., Buchkremer, H., Beck, T., and Stver, D. Characterization of porous, net-shaped niti alloy regarding its damping and energy-absorbing capacity. *Materials Science and Engineering: A 528*, 6 (2011), 2454 – 2462.

[63] Koike, J., Parkin, D. M., and Nastasi, M. Crystal-to-amorphous transformation of niti induced by cold rolling. *Journal of Materials Research 5*, 7 (1990), 14141418.

[64] Kundin, J., Raabe, D., and Emmerich, H. A phase-field model for incoherent martensitic transformations including plastic accommodation processes in the austenite. *Journal of the Mechanics and Physics of Solids 59*, 10 (Oct. 2011), 2082–2102. bibtex: Kundin2011.

[65] Lackmann, J., Niendorf, T., Maxisch, M., Grundmeier, G., and Maier, H. J. High-resolution in-situ characterization of the surface evolution of a polycrystalline NiTi SMA-alloy under pseudoelastic deformation. *Materials Characterization 62* (Mar. 2011), 298–303. 3 bibtex: Lackmann2011.

[66] Lakes, R. Materials with structural hierarchy. *Nature 361*, 511 (February 1993), 1786–1802.

[67] Laplanche, G., Birk, T., Schneider, S., Frenzel, J., and Eggeler, G. Effect of temperature and texture on the reorientation of martensite variants in niti shape memory alloys. *Acta Materialia 127* (2017), 143 – 152.

[68] Larson, B. C., Yang, W., Ice, G. E., Budai, J. D., and Tischler, J. Z. Three-dimensional X-ray structural microscopy with submicrometre resolution. *Nature 415* (Feb. 2002), 887–890. 6874 bibtex: Larson2002.

[69] LePage, W. S., Ahadi, A., Lenthe, W. C., Sun, Q.-P., Pollock, T. M., Shaw, J. A., and Daly, S. H. Grain size effects on niti shape memory alloy fatigue crack growth. *Journal of Materials Research* (2017), 117.

[70] Levitas, V., Roy, A., and Preston, D. Multiple twinning and variant-variant transformations in martensite: Phase-field approach. *Physical Review B 88*, 5 (2013), 054113 – 054120. bibtex: Levitas2013.

[71] Levitas, V. I., and Javanbakht, M. Interaction between phase transformations and dislocations at the nanoscale. Part 1. General phase field approach. *Journal of the Mechanics and Physics of Solids 82* (Sept. 2015), 287–319.

[72] Liu, Y. The superelastic anisotropy in a NiTi shape memory alloy thin sheet. *Acta Materialia* (2015).

[73] Liu, Y., Xie, Z., Van Humbeeck, J., and Delaey, L. Asymmetry of stress-strain curves under tension and compression for NiTi shape memory alloys. *Acta Materialia 46* (July 1998), 4325–4338. 12 bibtex: Liu1998.

[74] Liu, Y., Xie, Z. L., Van Humbeeck, J., and Delaey, L. Effect of texture orientation on the martensite deformation of NiTi shape memory alloy sheet. *Acta Materialia 47* (Jan. 1999), 645–660. 2 bibtex: Liu1999a.

[75] Malik, A., Amberg, G., Borgenstam, A., and gren, J. Phase-field modelling of martensitic transformation: the effects of grain and twin boundaries. *Modelling and Simulation in Materials Science and Engineering 21*, 8 (2013), 085003.

[76] Manchiraju, S., and Anderson, P. M. Coupling between martensitic phase transformations and plasticity: A microstructure-based finite element model. *International Journal of Plasticity 26* (Oct. 2010), 1508–1526.

[77] Mao, S. C., Han, X. D., Tian, Y. B., Luo, J. F., Zhang, Z., Ji, Y., and Wu, M. H. In situ EBSD investigations of the asymmetric stress-induced martensitic transformation in TiNi shape memory alloys under bending. *Materials Science and Engineering a-Structural Materials Properties Microstructure and Processing 498* (Dec. 2008), 278–282. 1-2 bibtex: Mao2008.

[78] Merzouki, T., Collard, C., Bourgeois, N., Ben Zineb, T., and Meraghni, F. Coupling between measured kinematic fields and multicrystal SMA finite element calculations. *Mechanics of Materials 42*, 1 (Jan. 2010), 72–95.

[79] Michutta, J., Somsen, C., Yawny, A., Dlouhy, A., and Eggeler, G. Elementary martensitic transformation processes in ni-rich niti single crystals with ni4ti3 precipitates. *Acta Materialia 54*, 13 (2006), 3525 – 3542. Selected Papers from the Meeting Micromechanics and Microstructure Evolution: Modeling, Simulation and Experiments held in Madrid/Spain, 1116 September 2005.

[80] Mirzaeifar, R., DesRoches, R., Yavari, A., and Gall, K. A micromechanical analysis of the coupled thermomechanical superelastic response of textured and untextured polycrystalline NiTi shape memory alloys. *Acta Materialia 61*, 12 (July 2013), 4542–4558. WOS:000321086100023 bibtex: Mirzaeifar2013.

[81] Miyazaki, S., Otsuka, K., and Wayman, C. The shape memory mechanism associated with the martensitic transformation in tini alloysii. variant coalescence and shape recovery. *Acta Metallurgica 37*, 7 (1989), 1885 – 1890.

[82] Miyazaki, S., Otsuka, K., and Wayman, C. M. The shape memory mechanism associated with the martensitic transformation in Ti- Ni alloysI. Self-accommodation. *Acta Metallurgica 37*, 7 (1989), 1873–1884. bibtex: Miyazaki1989a.

[83] Morin, C., Moumni, Z., and Zaki, W. Thermomechanical coupling in shape memory alloys under cyclic loadings: Experimental analysis and constitutive modeling. *International Journal of Plasticity 27*, 12 (Dec. 2011), 1959–1980. bibtex: Morin2011.

[84] Mullner, P., and King, A. Deformation of hierarchically twinned martensite. *Acta Materialia 58*, 16 (2010), 5242 – 5261.

[85] Naragani, D., Sangid, M. D., Shade, P. A., Schuren, J. C., Sharma, H., Park, J.-S., Kenesei, P., Bernier, J. V., Turner, T. J., and Parr, I. Investigation of fatigue crack initiation from a non-metallic inclusion via high energy x-ray diffraction microscopy. *Acta Materialia 137*, Supplement C (2017), 71 – 84.

[86] Niendorf, T., Kroo, P., Somsen, C., Eggeler, G., Chumlyakov, Y. I., and Maier, H. J. Martensite aging Avenue to new high temperature shape memory alloys. *Acta Materialia 89* (May 2015), 298–304.

[87] Niendorf, T., Lackmann, J., Gorny, B., and Maier, H. In situ characterization of martensite variant formation in nickeltitanium shape memory alloy under biaxial loading. *Scripta Materialia 65*, 10 (Nov. 2011), 915–918. bibtex: Niendorf2011.

[88] Nolze, G., and Hielscher, R. Orientations – perfectly colored. *Journal of Applied Crystallography 49*, 5 (Oct 2016), 1786–1802.

[89] Norfleet, D. M., Sarosi, P. M., Manchiraju, S., Wagner, M. F. X., Uchic, M. D., Anderson, P. M., and Mills, M. J. Transformation-induced plasticity during pseudoelastic deformation in Ni-Ti microcrystals. *Acta Materialia 57* (2009), 3549–3561. 12 bibtex: Norfleet2009.

[90] Okamoto, P. R., Heuer, J. K., Lam, N. Q., Ohnuki, S., Matsukawa, Y., Tozawa, K., and Stubbins, J. F. Stress-induced amorphization at moving crack tips in niti. *Applied Physics Letters 73*, 4 (1998), 473–475.

[91] Pagan, D. C., Bernier, J. V., Dale, D., Ko, J. P., Turner, T. J., Blank, B., and Shade, P. A. Measuring ti-7al slip system strengths at elevated temperature using high-energy x-ray diffraction. *Scripta Materialia 142* (2018), 96–100.

[92] Panico, M., and Brinson, L. C. A three-dimensional phenomenological model for martensite reorientation in shape memory alloys. *Journal of the Mechanics and Physics of Solids 55*, 11 (Nov. 2007), 2491–2511.

[93] Paranjape, H., and Anderson, P. M. Texture and grain neighborhood effects on NiTi shape memory alloy performance. *Modelling and Simulation in Materials Science and Engineering 22*, 7 (Oct. 2014), 075002.

[94] Paranjape, H. M., Bowers, M. L., Mills, M. J., and Anderson, P. M. Mechanisms for phase transformation induced slip in shape memory alloy micro-crystals. *Acta Materialia 132* (2017), 444 – 454.

[95] Paranjape, H. M., Manchiraju, S., and Anderson, P. M. A phase field Finite element approach to model the interaction between phase transformations and

plasticity in shape memory alloys. *International Journal of Plasticity 80* (May 2016), 1–18.

[96] Paranjape, H. M., Paul, P. P., Amin-Ahmadi, B., Sharma, H., Dale, D., Ko, J. P., Chumlyakov, Y. I., Brinson, L. C., and Stebner, A. P. In situ, 3d characterization of the deformation mechanics of a superelastic niti shape memory alloy single crystal under multiscale constraint. *Acta Materialia 144* (2018), 748 – 757.

[97] Paranjape, H. M., Paul, P. P., Sharma, H., Kenesei, P., Park, J.-S., Duerig, T., Brinson, L. C., and Stebner, A. P. Influences of granular constraints and surface effects on the heterogeneity of elastic, superelastic, and plastic responses of polycrystalline shape memory alloys. *Journal of the Mechanics and Physics of Solids 102* (2017), 46 – 66.

[98] Park, J.-S., Zhang, X., Sharma, H., Kenesei, P., Hoelzer, D., Li, M., and Almer, J. High-energy synchrotron x-ray techniques for studying irradiated materials. *Journal of Materials Research 30*, 09 (May 2015), 1380–1391.

[99] Patoor, E., Eberhardt, A., and Berveiller, M. Micromechanical modelling of the shape behavior. *American Society of Mechanical Engineers, Applied Mechanics Division, AMD 189* (1994), 23–37.

[100] Paul, P. P., Fortman, M., Paranjape, H. M., Anderson, P. M., Stebner, A. P., and Brinson, L. C. Influence of structure and microstructure on deformation localization and crack growth in niti shape memory alloys. *Shape Memory and Superelasticity* (Apr 2018).

[101] Paul, P. P., Paranjape, H. M., Amin-Ahmadi, B., Stebner, A. P., Dunand, D. C., and Brinson, L. C. Effect of machined feature size relative to the microstructural size on the superelastic performance in polycrystalline niti shape memory alloys. *Materials Science and Engineering: A 706* (2017), 227–235.

[102] Paul, P. P., Paranjape, H. M., Main-Ahmadi, B., Bucsek, A. N., Pagan, D., Chumlyakov, Y. I., Stebner, A. P., and Brinson, L. C. Effect of multiscale constraints on heterogeneity of deformation across length scales in hierarchical sma material. *Acta Materialia* (In Review).

[103] Peultier, B., Ben Zineb, T., and Patoor, E. A simplified micromechanical constitutive law adapted to the design of shape memory applications by finite element methods. *Materials Science and Engineering: A 481* (2008), 384–388. bibtex: Peultier2008.

[104] Pilkey, W. D., and Pilkey, D. F. *Holes*. John Wiley & Sons, Inc., 2008, pp. 176–400.

[105] Qiu, S., Clausen, B., Padula, S. A., Noebe, R. D., and Vaidyanathan, R. On elastic moduli and elastic anisotropy in polycrystalline martensitic NiTi. *Acta Materialia 59* (Aug. 2011), 5055–5066.

[106] Rahim, M., Frenzel, J., Frotscher, M., Pfetzing-Micklich, J., Steegmüller, R., Wohlschlögel, M., H. Mughrabi, H., and Eggeler, G. Impurity levels and fatigue lives of pseudoelastic niti shape memory alloys. *Acta Materialia 61* (2013), 3667–3686.

[107] Rajagopalan, S., Little, A. L., Bourke, M. a. M., and Vaidyanathan, R. Elastic modulus of shape-memory NiTi from in situ neutron diffraction during macroscopic loading, instrumented indentation, and extensometry. *Applied Physics Letters 86*, 8 (Feb. 2005), 081901.

[108] Richards, A. W., Lebensohn, R. A., and Bhattacharya, K. Interplay of martensitic phase transformation and plastic slip in polycrystals. *Acta Materialia 61*, 12 (July 2013), 4384–4397.

[109] Robertson, S. W., Mehta, A., Pelton, A. R., and Ritchie, R. O. Evolution of crack-tip transformation zones in superelastic Nitinol subjected to in situ fatigue: A fracture mechanics and synchrotron X-ray microdiffraction analysis. *Acta Materialia 55* (Oct. 2007), 6198–6207. 18 bibtex: Robertson2007.

[110] Roters, F., Eisenlohr, P., Hantcherli, L., Tjahjanto, D., Bieler, T., and Raabe, D. Overview of constitutive laws, kinematics, homogenization and multiscale methods in crystal plasticity finite-element modeling: Theory, experiments, applications. *Acta Materialia 58*, 4 (Feb. 2010), 1152–1211. bibtex: Roters2010.

[111] Saedi, S., Turabi, A. S., Andani, M. T., Moghaddam, N. S., Elahinia, M., and Karaca, H. E. Texture, aging, and superelasticity of selective laser melting fabricated ni-rich niti alloys. *Materials Science and Engineering: A 686*, Supplement C (2017), 1 – 10.

[112] San Juan, J., N, M. L., and Schuh, C. A. Thermomechanical behavior at the nanoscale and size effects in shape memory alloys. *Journal of Materials Research 26*, 19 (Oct. 2011), 2461–2469.

[113] Schaffer, J. E. Structure-property relationships in conventional and nanocrystalline niti intermetallic alloy wire. *Journal of Materials Engineering and Performance 18*, 5 (2009), 582–587.

[114] Shade, P. A., Blank, B., Schuren, J. C., Turner, T. J., Kenesei, P., Goetze, K., Suter, R. M., Bernier, J. V., Li, S. F., Lind, J., Lienert,

U., and Almer, J. A rotational and axial motion system load frame insert for in situ high energy x-ray studies. *Review of Scientific Instruments 86*, 9 (2015), 093902.

[115] Sharma, H., Huizenga, R. M., and Offerman, S. E. A fast methodology to determine the characteristics of thousands of grains using three-dimensional X-ray diffraction. I. Overlapping diffraction peaks and parameters of the experimental setup. *Journal of Applied Crystallography 45*, 4 (Aug 2012), 693–704.

[116] Sharma, H., Huizenga, R. M., and Offerman, S. E. A fast methodology to determine the characteristics of thousands of grains using three-dimensional X-ray diffraction. II. Volume, centre-of-mass position, crystallographic orientation and strain state of grains. *Journal of Applied Crystallography 45*, 4 (Aug 2012), 705–718.

[117] Stebner, A. P., and Brinson, L. C. Explicit finite element implementation of an improved three dimensional constitutive model for shape memory alloys. *Computer Methods in Applied Mechanics and Engineering 257* (Apr. 2013), 17–35.

[118] Stebner, A. P., Brown, D. W., and Brinson, L. C. Young's modulus evolution and texture-based elastic-inelastic strain partitioning during large uniaxial deformations of monoclinic nickel-titanium. *Acta Materialia 61*, 6 (Apr. 2013), 1944–1956.

[119] Stebner, A. P., Paranjape, H. M., Clausen, B., Brinson, L. C., and Pelton, A. R. In Situ Neutron Diffraction Studies of Large Monotonic Deformations of Superelastic Nitinol. *Shape Memory and Superelasticity 1*, 2 (May 2015), 252–267.

[120] Stebner, A. P., Vogel, S. C., Noebe, R. D., Sisneros, T. A., Clausen, B., Brown, D. W., Garg, A., and Brinson, L. C. Micromechanical quantification of elastic, twinning, and slip strain partitioning exhibited by polycrystalline, monoclinic nickel-titanium during large uniaxial deformations measured via in-situ neutron diffraction. *Journal of the Mechanics and Physics of Solids 61*, 11 (Nov. 2013), 2302–2330.

[121] Sutou, Y., Omori, T., Yamauchi, K., Ono, N., Kainuma, R., and Ishida, K. Effect of grain size and texture on pseudoelasticity in CuAlMn-based shape memory wire. *Acta Materialia 53*, 15 (Sept. 2005), 4121–4133.

[122] Tamura, N. *XMAS: A Versatile Tool for Analyzing Synchrotron X-ray Microdiffraction Data*. IMPERIAL COLLEGE PRESS, 2014, ch. Chapter 4, pp. 125–155.

[123] Tamura, N., Kunz, M., Chen, K., Celestre, R., MacDowell, A., and Warwick, T. A superbend x-ray microdiffraction beamline at the advanced light source. *Materials Science and Engineering: A 524*, 1-2 (2009), 28–32.

[124] Thamburaja, P., and Anand, L. Polycrystalline shape-memory materials: Effect of crystallographic texture. *Journal of the Mechanics and Physics of Solids 49* (2001), 709–737.

[125] Thamburaja, P., Pan, H., and Chau, F. S. Martensitic reorientation and shape-memory effect in initially textured polycrystalline Ti-Ni sheet. *Acta Materialia 53* (Aug. 2005), 3821–3831. 14 bibtex: Thamburaja2005a.

[126] Thomas, G., Mori, H., Fujita, H., and Sinclair, R. Electron irradiation induced crystalline amorphous transitions in niti alloys. *Scripta Metallurgica 16*, 5 (1982), 589 – 592.

[127] Tirry, W., and Schryvers, D. Linking a completely three-dimensional nanostrain toa structural transformation eigenstrain. *Nature Materials 8*, 9 (Sept. 2009), 752–757.

[128] Ueland, S. M., and Schuh, C. A. Grain boundary and triple junction constraints during martensitic transformation in shape memory alloys. *Journal of Applied Physics 114*, 5 (Aug. 2013), 053503.

[129] Ueland, S. M., and Schuh, C. A. Transition from many domain to single domain martensite morphology in small-scale shape memory alloys. *Acta Materialia 61*, 15 (Sept. 2013), 5618–5625.

[130] Vaidyanathan, R., Bourke, M., and Dunand, D. Phase fraction, texture and strain evolution in superelastic niti and nititic composites investigated by neutron diffraction. *Acta Materialia 47*, 12 (1999), 3353 – 3366.

[131] Vaidyanathan, R., Dunand, D. C., and Ramamurty, U. Fatigue crack-growth in shape-memory NiTi and NiTiTiC composites. *Materials Science and Engineering: A 289*, 12 (Sept. 2000), 208–216.

[132] Van Humbeeck, J. Non-medical applications of shape memory alloys. *Materials Science and Engineering: A 273* (1999), 134–148. bibtex: VanHumbeeck1999.

[133] W., R. S., V., I., H.-R., W., and O., R. R. Crystallographic texture for tube and plate of the superelastic/shape-memory alloy nitinol used for endovascular stents. *Journal of Biomedical Materials Research Part A 72A*, 2 (2004), 190–199.

[134] Waitz, T. The self-accommodated morphology of martensite in nanocrystalline niti shape memory alloys. *Acta Materialia 53*, 8 (2005), 2273 – 2283.

[135] Waitz, T., Antretter, T., Fischer, F. D., and Karnthaler, H. P. Size effects on martensitic phase transformations in nanocrystalline NiTi shape memory alloys. *Materials Science and Technology 24*, 8 (Aug. 2008), 934–940.

[136] Waitz, T., Kazykhanov, V., and Karnthaler, H. Martensitic phase transformations in nanocrystalline niti studied by tem. *Acta Materialia 52*, 1 (2004), 137 – 147.

[137] Wang, G. Effects of notch geometry on stressstrain distribution, martensite transformation and fracture behavior in shape memory alloy niti. *Materials Science and Engineering: A 434*, 1 (2006), 269 – 279.

[138] Wang, X., Speirs, M., Kustov, S., Vrancken, B., Li, X., Kruth, J.-P., and Humbeeck, J. V. Selective laser melting produced layer-structured niti shape memory alloys with high damping properties and elinvar effect. *Scripta Materialia 146* (2018), 246 – 250.

[139] Whittaker, D. R., and Fillinger, M. F. The engineering of endovascular stent technology: A review. *Vascular and Endovascular Surgery 40*, 2 (2006), 85–94.

[140] Wu, Y., Ojha, A., Patriarca, L., and Sehitoglu, H. Fatigue Crack Growth Fundamentals in Shape Memory Alloys. *Shape Memory and Superelasticity 1*, 1 (Mar. 2015), 18–40.

[141] Xie, C. Y., Zhao, L. C., and Lei, T. C. Effect of Ti3ni4 precipitates on the phase transitions in an aged Ti-51.8at% Ni shape memory alloy. *Scripta Metallurgica et Materialia 24*, 9 (Sept. 1990), 1753–1758.

[142] Ye, J., Mishra, R. K., Pelton, A. R., and Minor, A. M. Direct observation of the NiTi martensitic phase transformation in nanoscale volumes. *Acta Materialia 58*, 2 (Jan. 2010), 490–498.

[143] Yin, H., He, Y., Moumni, Z., and Sun, Q. Effects of grain size on tensile fatigue life of nanostructured niti shape memory alloy. *International Journal of Fatigue 88* (2016), 166 – 177.

[144] Yuan, W. Q., and Yi, S. Pseudo-elastic strain estimation of textured TiNi shape memory alloys. *Materials Science and Engineering a-Structural Materials Properties Microstructure and Processing 271* (Nov. 1999), 439–448. 1-2 bibtex: Yuan1999.

[145] Zhao, P., Song En Low, T., Wang, Y., and Niezgoda, S. R. An integrated full-field model of concurrent plastic deformation and microstructure evolution: Application to 3d simulation of dynamic recrystallization in polycrystalline copper. *International Journal of Plasticity 80* (May 2016), 38–55.

[146] Zhou, N., Shen, C., Wagner, M. F. X., Eggeler, G., Mills, M. J., and Wang, Y. Effect of Ni(4)Ti(3) precipitation on martensitic transformation in Ti-Ni. *Acta Materialia 58* (Dec. 2010), 6685–6694. 20 bibtex: Zhou2010.

[147] Zhu, P., Stebner, A. P., and Brinson, L. C. Finite Element Study of Pore Interactions in Shape Memory Alloy Plates Using an Elastic-Transformation-Plastic Constitutive Model, ASME Smart materials, Adaptive Structures, and Intelligenet Systems Annual Conference, Snowbird, UT, Sept. 2013.

[148] Zhu, P., Stebner, A. P., and Brinson, L. C. A numerical study of the coupling of elastic and transformation fields in pore arrays in shape memory alloy plates to advance porous structure design and optimization. *Smart Materials and Structures 22*, 9 (Sept. 2013). WOS:000323832000011 bibtex: Zhu2013.

APPENDIX

Appendix A: Supplementary Data for Diffraction Analyses

1. Supplementary data for Chapter 4: Parameters Used in HEDM Analysis

1.1. List of parameters used during room temperature HEDM analysis

Table .1. List of parameters used during room temperature HEDM analysis

Parameter	Value
Sample to detector distance	1 046 929.02 µm
Wavelength of X-ray beam	0.222 921 Å
Beam Center	(1029.203569922250, 1027.473268714830)
Tilts (tx, ty, yz)	(0.136869387, 0.240109719, -0.014083165)
(po, p1, p2)	(-0.000114211, -0.000044213, -0.000487309)
Wedge	0.061993764
Threshold	150
Completeness Cutoff	0.8
Angular Tolerance	0.5
Fiber Step	0.5
Stress free lattice parameters	($a = 2.89$ Å, $b = 4.11$ Å, $c = 4.65$ Å),
for monoclinic NiTi	($\beta = 96.95^0$ and $\alpha, \gamma = 90.00^0$)

1.2. List of parameters used during high temperature HEDM analysis

Table .2. List of parameters used during high temperature HEDM analysis

Parameter	Value
Calibration position	(-0.081878967, 0.0, 0.051679426)
Wavelength of X-ray beam	0.324 104 Å
Beam Center	(1029.203569922250, 1027.473268714830)
Detector 1 Tilts	(0.002759268, -0.012092556, -0.001757652)
Detector 1 t_vec_d	(137.414335, -2.73432133, -734.804950)
Detector 2 Tilts	(0.005295383, 0.011441169, -0.001504351)
Detector 2 t_vec_d	(-147.044903, -2.191167076, -734.878812)
Wedge	-0.002974246
Orientations Threshold	2
Grains Threshold	5
Clustering Radius	1.0
Completeness Cutoff	0.8
Angular Tolerance (η, ω)	(1.0, 2.0)
Fiber Step	0.5
Stress free lattice parameters	$(a,\ b,\ c = 3.01\,\text{Å})$,
for cubic NiTi	$(\alpha, \beta, \gamma = 90.00^0)$

2. Supplementary data for Chapter 5: Parameters Used in MicroLaue Analysis

The calibration parameters, from the standard Si calibration, used for the microLaue analysis are listed below.

Table .3. List of parameters used for microLaue analysis

Parameter	Value
Detector and Beam Settings:	
Sample to detector distance	150.336mm
Energy range of X-ray beam	6 - 24 keV
Detector tilts (^{0})	0: Roll, -0.09698: Pitch, 0.64682: Yaw
Camera Dimensions (px)	1043 x 981
Center Channel Position (px)	(536.063 230.397)
Laue Indexing Parameters:	
Angular Tolerance (^{0})	0.15
Sample ω, χ, ϕ	0, 0, 0
Num. Ref. for Index	800
Starting Set	20
Minimum nb Index	20
Material Settings:	
Stress free lattice parameters	($a = 2.89$ Å, $b = 4.11$ Å, $c = 4.65$ Å),
for monoclinic NiTi	($\beta = 96.95^0$ and $\alpha, \gamma = 90.00^0$)